

**ALUMINUM-SILICON CARBIDE COMPOSITE COATINGS  
BY PLASMA SPRAYING**

by

**KUNAL GHOSH**

**B.Tech., Indian Institute of Technology, 1994**

**A THESIS SUBMITTED IN PARTIAL FULFILLMENT OF THE  
REQUIREMENTS FOR THE DEGREE OF  
MASTER OF APPLIED SCIENCE**

in

**THE FACULTY OF GRADUATE STUDIES  
(Department of Metals and Materials Engineering)  
We accept this report as conforming to the required standard**

**THE UNIVERSITY OF BRITISH COLUMBIA**

**August, 1996**

**© Kunal Ghosh, 1996**

In presenting this thesis in partial fulfilment of the requirements for an advanced degree at the University of British Columbia, I agree that the Library shall make it freely available for reference and study. I further agree that permission for extensive copying of this thesis for scholarly purposes may be granted by the head of my department or by his or her representatives. It is understood that copying or publication of this thesis for financial gain shall not be allowed without my written permission.

Department of Metals & Materials Eng.

The University of British Columbia  
Vancouver, Canada

Date 23<sup>rd</sup> August, 1996

## Abstract

The use of aluminum in the automobile engines and other critical parts require a superior surface property of the same. This has led to the development of plasma sprayable surface coatings for the components. To impart the maximum bonding strength, along with hardness to the coatings an aluminum based composite (Al-SiC) was found to be the most suitable. The presence of a hard ceramic second phase within a soft metallic matrix greatly improves the wear resistance of the composite material. The powders for spraying were prepared by mechanical agglomeration of 6061 Al alloy (particle size between 40 and 60  $\mu\text{m}$ ) with fine SiC particles ( $\approx 8 \mu\text{m}$ ) by using high energy vibratory mills. The concentration of SiC was varied from 20-75 vol%, the balance being the matrix Al alloy. The size of the reinforcement was varied from 8 to 37  $\mu\text{m}$  in the Al-50vol%SiC composite coatings. A Process Control Agent (PCA) was used to modify the morphology of the powders during the process of mechanical alloying. Mechanical alloying produced composite powders in a size range between 40 and 120  $\mu\text{m}$  with the SiC phase uniformly dispersed within the matrix. The powders used for spraying were fractionated between the size range of 44 and 149  $\mu\text{m}$  by sieving.

The powders were sprayed using two types of axial feed plasma torches. Coatings were sprayed on mild steel coupons, rods and thin foils of Al, Ni, plain carbon steel and stainless steel, which were used for conducting tests to assess the physical properties of the coatings. The cross sections of the coatings sprayed on the coupons were observed under an SEM and optical microscope. The hardness, porosity and SiC distribution of the coatings were assessed on these cross sections. The coatings were

tested for different physical and mechanical properties like adhesion and wear strength.

Adhesion was tested on the mild steel rods using the standard ASTM C633 pull tests but the results were mostly inconclusive. Adhesion strength on the foils was also measured by peel tests which is a modification of the ASTM D-3167 tests. The coatings showed high adhesion strength compared to the other commercially available coatings reported in a recent work [40]. Adhesion strength was found to decrease with the increase in the SiC content and decrease in SiC particle sizes.

Erosive wear of the coatings was assessed using a dry erosion test which is a modification of the ASTM G76-83 test. The increase in the SiC content and decrease in the reinforcing particle size improved the wear resistance of the coatings. The abrasive wear resistance was found to improve with the increase in SiC particle size and also with the SiC content in the composite powders (or coatings).

# Table of Contents

<b>Abstract</b>	ii
<b>Table of Contents</b>	iv
<b>List of Figures</b>	vi
<b>List of Tables</b>	ix
<b>Acknowledgments</b>	x
<b>Chapter 1: Introduction</b>	
<b>1.1 The Concepts of Surface Engineering</b> .....	1
<b>1.2 Commonly Used Coating Methods</b> .....	3
1.2.1 Vapor Deposition Techniques .....	3
1.2.2 Thermal Spraying .....	6
<b>Chapter 2: Literature Review</b>	
<b>2.1 Al-SiC Systems</b> .....	15
2.1.1 Background of Al-SiC systems .....	15
2.1.2 Wear Properties of Al-SiC Composites .....	17
<b>2.2 Powder Production for Plasma Spraying</b> .....	18
2.2.1 Powder Characteristics .....	18
2.2.2 Powder Manufacturing Techniques .....	20
<b>2.3 The Process of Mechanical Alloying</b> .....	22
2.3.1 Background .....	22
2.3.2 Mechanism of Mechanical Alloying .....	23
2.3.3 Structural Developments in Mechanical Alloying .....	26
2.3.4 Process Control Agents .....	28
2.3.5 Physics of Mechanical Alloying .....	30
<b>2.4 The Plasma Spraying Process</b> .....	34
<b>2.5 Coating Adhesion Tests</b> .....	37
2.5.1 Tensile Adhesion Test .....	38
2.5.2 Peel Adhesion Tests .....	38
<b>2.6 Wear Tests</b> .....	41
2.6.1 Abrasive Wear .....	41
2.6.2 Erosion Wear .....	43
<b>2.7 Previous Work on Al-SiC Coatings</b> .....	44

<b>Chapter 3: Scope and Objectives</b> .....	46	
 <b>Chapter 4: Experimental</b>		
<b>4.1 Powder Preparation</b> .....	47	
4.1.1 Starting Material .....	47	
4.1.2 Powder Preparation .....	49	
4.1.3 Powder Analysis .....	51	
<b>4.2 Coating Experiments and Analysis</b> .....	51	
4.2.1 Plasma Spray process .....	51	
4.2.2 Hardness Measurements .....	53	
4.2.3 Adhesion Measurements .....	53	
4.2.4 Wear Tests .....	54	
 <b>Chapter 5: Results and Discussion</b>		
<b>5.1 Powder Preparation</b> .....	56	
5.1.1 Powder Morphology .....	56	
5.1.2 Powder Microstructure .....	74	
5.1.3 Powder Composition Analyses .....	78	
5.1.4 X-ray Diffractometry .....	79	
<b>5.2 Coating Deposition</b> .....	83	
<b>5.3 Coating Characteristics</b> .....	84	
5.3.1 Coating Microstructure .....	84	
5.3.2 Coating Hardness .....	92	
5.3.3 Adhesion Strength .....	80	
5.3.4 Wear Resistance .....	88	
 <b>Chapter 6: Interparticle Distance: Model vs. Experiment</b>		
<b>6.1 Background</b> .....	112	
<b>6.2 Geometric Model</b> .....	112	
6.2.1 Assumptions .....	113	
6.2.2 Derivations and Experimental Verifications .....	114	
<b>6.3 Discussion of Model</b> .....	116	
 <b>Chapter 7: Summary and Conclusions</b> .....		118
 <b>Chapter 8: Future Work and Recommendations</b> .....		121
<b>References</b> .....	122	
<b>Appendix (I)</b> .....	126	

## List of Figures

Figure 1	Commonly Used Surface Engineering Techniques .....	2
Figure 2a	Achievable Coating Thickness in Surface Engineering .....	2
Figure 2b	Surface Temperature in Surface Engineering .....	3
Figure 3	Schematic of CVD Process .....	4
Figure 4	Schematic Microstructure of a Thermal Spray Coating .....	7
Figure 5	Schematic Diagram of a Combustion Wire Gun .....	8
Figure 6	Schematic Diagram of a Flame Spray Gun .....	8
Figure 7	Schematic of a Detonation Gun .....	9
Figure 8	Schematic of an Axial Powder Plasma Torch .....	10
Figure 9	Effect of Powder Injection Velocity in Radial Feed Torch .....	11
Figure 10	Schematic of the Szegvari Attritor .....	24
Figure 11	Schematic of a SPEX Shaker Mill .....	25
Figure 12	Schematic Illustration of the MA Process .....	27
Figure 13	Ductile fracture on Aluminum .....	29
Figure 14	Comparison of Upset Forging and MA .....	33
Figure 15	Segregation in Composites during Plasma Spraying .....	37
Figure 16	Schematic of the Tensile Adhesion Test .....	39
Figure 17	Schematic of the Peel Adhesion Test .....	40
Figure 18	Geometries employed in Abrasive Wear Test .....	42
Figure 19	Schematic of a Solid Particle Erosion Test .....	44

Figure 20	Morphology of a Starting Powder .....	48
Figure 21	Powder Morphology after 5 min of milling .....	57
Figure 22	Powder Morphology after 10 min of milling .....	58
Figure 23	Powder Morphology after 20 min of milling .....	59
Figure 24	Powder Morphology after 30 min of milling .....	60
Figure 25	Particle Size Change with Milling time .....	63
Figure 26	Variation in equilibrium particle size with PCA content .....	66
Figure 27	Energy requirements for reducing SiC .....	68
Figure 28	Change in SiC sizes with Milling time .....	69
Figure 29	Change in yield with PCA and SiC content .....	72
Figure 30	Change in yield with MMC/SiC size ratio .....	73
Figure 31	Composite Powder Cross Sections .....	75
Figure 32	Cross Section of Al-75SiC1200 powders .....	77
Figure 33	Cross section of powders without PCA .....	77
Figure 34	X-ray patterns of the starting powders .....	80
Figure 35	X-ray patterns of the powders in various stages of milling .....	81
Figure 36	Cross Section of Plasma Sprayed Coatings .....	85
Figure 37	X-ray patterns of the coating .....	87
Figure 38	Schematic showing Measurement of Interparticle Distance .....	88
Figure 39	Variation of interparticle distance in coatings .....	89
Figure 40	Change in Interparticle Distance with SiC content .....	91
Figure 41	Change in Interparticle Distance with SiC sizes .....	91

Figure 42	Change in Hardness with Coating Thickness .....	94
Figure 43	Peel strength graphs of coatings .....	97
Figure 44	Fusion of Al substrate during spraying of Al-SiC powder .....	102
Figure 45	Change in Peel Strength with SiC content .....	103
Figure 46	Change in Peel Strength with SiC Particle size .....	103
Figure 47	Change in Abrasive Wear with SiC Content .....	104
Figure 48	Change in Abrasive Wear with SiC Particle Size .....	105
Figure 49	Change in Erosive Wear with SiC Content .....	108
Figure 50	Change in Erosive Wear with SiC particle sizes .....	108
Figure 51	Eroded surface of Al-50SiC 800 coatings .....	109
Figure 52	Dependence of erosive wear on SiC particle size .....	110
Figure 53	Commonly found modes of packing .....	113
Figure 54	Calculated change in $\lambda$ with packing and SiC content .....	115
Figure 55	Calculated change in $\lambda$ with packing and SiC sizes .....	116

## List of Tables

Table 1:	Plasma Sprayed Materials and their uses .....	13
Table 2:	Milling Parameters of the machines commonly used .....	33
Table 3:	Elemental Composition of the Al 6061 metal .....	47
Table 4:	Summary of the Processed Composite Powders .....	50
Table 5:	Summary of the Spraying Conditions .....	52
Table 6:	Composition Analysis by the Wet Method .....	79
Table 7:	Summary of the substrates sprayed and their uses .....	84
Table 8:	Hardness of the Powders and Coatings .....	93
Table 9:	Summary of the ASTM C633 Pull Adhesion Tests .....	96
Table 10:	Summary of Peel Test without calibration .....	97
Table 11:	Summary of Peel Test after calibration .....	100

## Acknowledgments

The author would like to express his gratitude and thanks to his supervisors Dr. Tom Troczynski and Prof. A.C.D. Chaklader for their advice, expertise and guidance during the entire course of the project.

The assistance provided by Northwest Mettech. and Metcon Services in spraying the coatings and providing other research facilities are greatly appreciated. The help provided by National Research Council, Vancouver in allowing the use of their equipment is gratefully acknowledged.

A special thanks to Edith Breslauer, Edmond Lin, Mike Sexsmith and the other associates of ceramics lab for the assistance provided in different stages of the experimental work. Thanks to Noah Third and Partha Ganguly for the assistance provided in compilation of the entire work.

Special thanks are extended to the staff, students and faculties of the Department of Metals and Materials Engineering at UBC. The financial assistance from the Science Council of British Columbia and NSERC for the project is gratefully acknowledged.

## **Chapter 1: Introduction**

### ***1.1 The Concepts of Surface Engineering***

The choice of a material for structural engineering applications is often based on the strength of the material. But the material may not possess satisfactory surface properties such as wear and corrosion resistance, thermal insulation, electrical conductivity, etc. To improve the surface condition and impart specific surface properties, a surface treatment or coating might be required. Surface engineering thus can be defined as the design of a composite system (coating and substrate) which shows a performance that cannot be achieved either by the coating or substrate alone [1]. The main criterion of surface engineering is that the coating should not impair the properties of the bulk substrate.

There is a vast range of surface treatment techniques which can be broadly classified into “dry” and “wet” methods. The dry coating techniques have much less environmental impact than the wet processes like electroplating, salt bath nitriding, etc. [1]. The latter processes use high concentration of acids and alkalis which often produce toxic byproducts like cyanides. In contrast to the wet methods, the dry advanced surface treatment techniques operate at a high temperature and have a higher productivity than the wet processes.

The diverse surface treatment methods available are classified in Fig. 1 based on the deposition method [1]. Selection of the appropriate technique for a given application is frequently based on the thickness of the coating required and acceptable surface

temperature of substrate during deposition. Figures 2a and b show the achievable coating thickness and the substrate temperatures attained during the respective surface treatments.

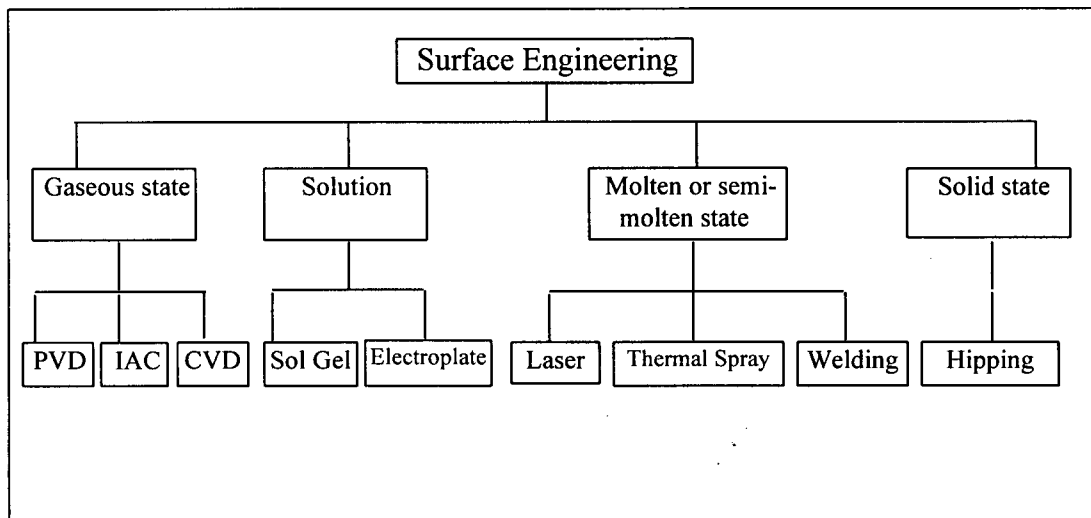


Fig. 1: Commonly used surface engineering techniques [1]. PVD = Physical vapor deposition, IAC = Ion assisted coating, CVD = Chemical vapor deposition.

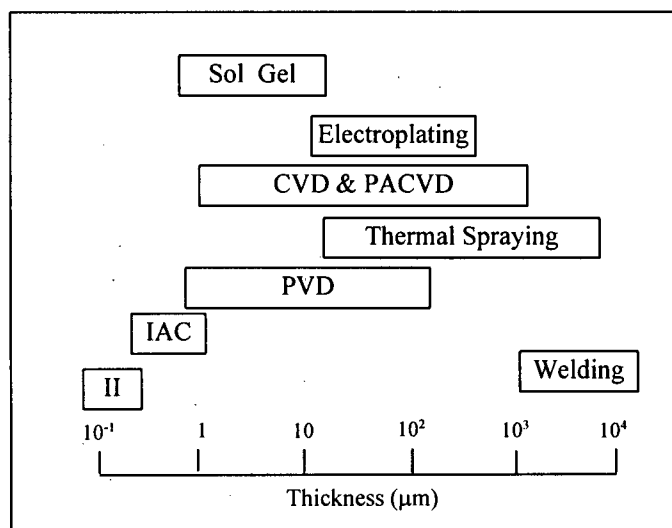


Fig. 2a: Achievable coating thickness using the commonly used surface engineering techniques [1]. PACVD = Plasma assisted chemical vapor deposition.

Most of the dry surface treatment processes like Physical Vapor Deposition (PVD)/Chemical Vapor Deposition(CVD) involve a closed chamber which limits the size and shape of the component that can be coated. The level of vacuum required in the chambers also varies amongst the various processes. In the following section a brief description of the advanced dry coating techniques with their relative merits and demerits are discussed.

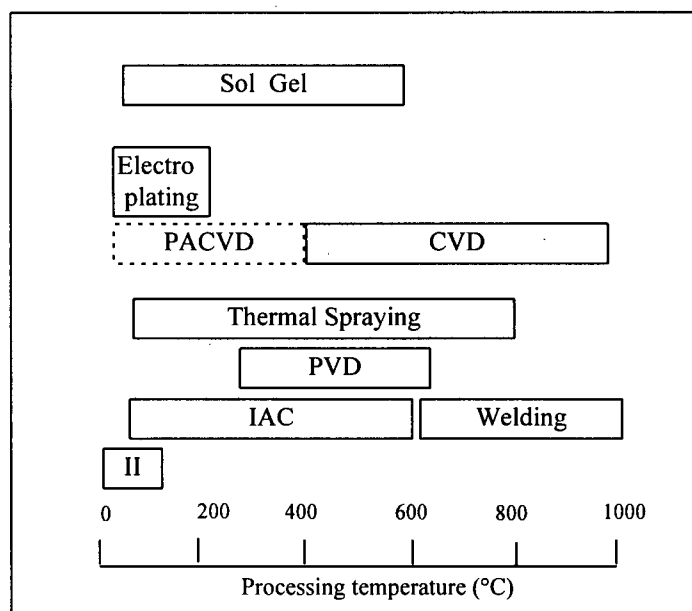


Fig. 2b: Surface temperature attained during the commonly used surface engineering methods [1].

## 1.2 Commonly used Coating Methods

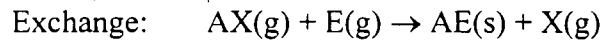
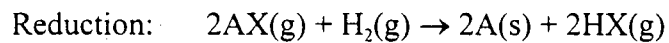
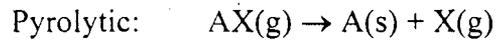
### 1.2.1 Vapor Deposition Techniques

#### a) Chemical Vapor Deposition CVD

Chemical Vapor Deposition coatings are generated by the thermal reaction of gaseous compounds on the surface of the substrate yielding a solid material [1,2]. The principle of CVD coatings is shown schematically in Fig. 3, which illustrates the buildup

of a coating (black spheres) on a substrate (white spheres). In addition to the solid material a volatile gaseous product is also produced which is removed from the reactor.

The major types of reactions achievable using CVD include:



where 'A' represents a metallic atom like Cu, Ag, etc., 'X' represents the by-product gases, and 'E' represents the reactive gases like nitrogen.

In CVD, there is a complex interplay between different reactions taking place in the vapor phase, both at the vapor/solid interface and the substrate/coating interface [1].

CVD coatings are developed atom by atom hence the microstructure of the coatings produced is different from most other processes.

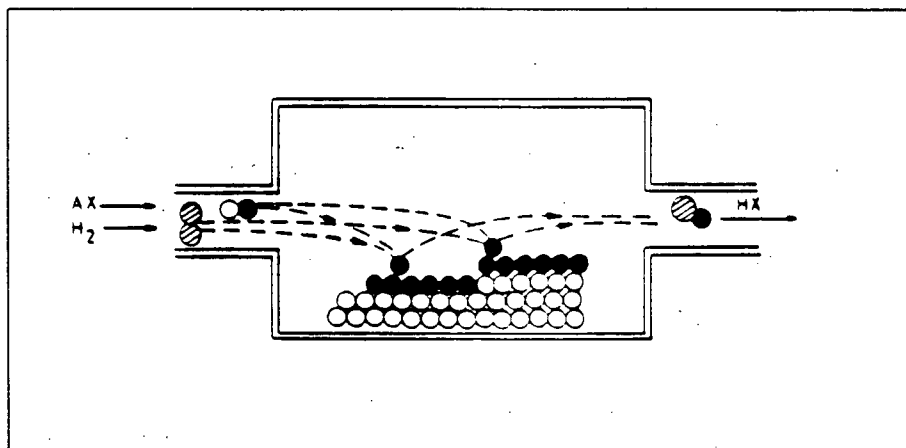


Fig. 3: Schematic of a CVD Process [1].

A major advantage of CVD is that complex shapes can be coated if uniform heating and gas flow can be achieved. However, this is difficult and sometimes elaborate

gas distribution systems are required. Typically, CVD coatings are produced in a batch process with a few hundred of components being loaded at the same time in a furnace.

One of the major limitations of the CVD process is the high temperature (generally in excess of 800°C) of the substrates required to produce the coatings. The high temperature limits the type of substrate that can be coated without thermal distortion of the component or degradation of its mechanical properties and microstructures. The difference in the coefficient of thermal expansion (CTE) between the coating and the substrate may result in excessive residual stresses during cooling after deposition. This is true especially in the case of ceramic coatings on metals. Another major limitation of CVD is the toxicity and corrosivity of the reactants and/or the by-products of the reactions. The cost of a CVD coating depends largely on the material being deposited and has been estimated to be between \$ 0.001 and \$ 0.5/( $\mu\text{m cm}^2$ ) [2].

b) Physical Vapor Deposition (PVD)

The Physical Vapor Deposition coatings are produced by a variety of techniques including thermal, cathodic arc, electron beam evaporation, sputtering, ion beam implantation, ion beam plating and many other techniques [2]. In thermal evaporation the material is simply evaporated or sublimed using electrical (resistive or inductive) heating of the coating material. Electron beam evaporation is a variant of thermal evaporation in which an electron beam is used to heat the material. In reactive evaporation a second element is introduced into the chamber to react with the evaporated material on the substrate surface to form a coating such as  $\text{Ti}_3\text{N}_4$ . In cathodic arc evaporation an electric

arc not only evaporates the cathode material but also ionizes it. By introducing an electrical bias on the substrate, substantial kinetic energy can be imparted to the ions, thus improving the bonding and microstructure. One of the main problems of the cathodic arc process is the tendency to eject macro-particles of material from the target which causes lumps, porosity, and generally deteriorates the microstructure of the coating.

Deposition of the PVD coatings is usually done in batches in vacuum furnaces. PVD coatings require extremely clean surface. Therefore, before the actual deposition is done the substrate is additionally cleaned to remove traces of surface oxides. Unlike most other deposition techniques the highest bond strength is obtained with PVD coatings when the surface of the substrate is smooth. The average cost of PVD is higher than CVD mainly due to the high intensity vacuum required in the chamber and varies between 0.05 and 1.00  $\$/(\mu\text{m cm}^2)$  [2].

### 1.2.2 Thermal Spraying

Thermal spraying is a generic name for a family of coating processes in which a material is heated rapidly in a hot gaseous medium and projected onto a roughened substrate where it builds up the desired coating [1,2]. The material is provided either as powder or droplets from wires or rods, heated to near or above their melting points. The molten material forms into thin lamellar droplets which splat on impact. The coating is composed of many splats overlapping and interlocking as shown in Fig. 4. Usually the molten droplets are between 30 and 60 microns in diameter and the resulting splats are only a few microns thick. Typical coating thickness varies between 50 and 1000  $\mu\text{m}$ .

There are two main advantages of producing coatings by thermal spray technique: a) the substrate temperature remains relatively low during spraying and b) the large variety of materials can be sprayed using this technique. The substrate temperature usually remains below 300°C and so fully heat treated aluminum, titanium or steel alloys can be coated without changing their microstructure or mechanical properties. Virtually

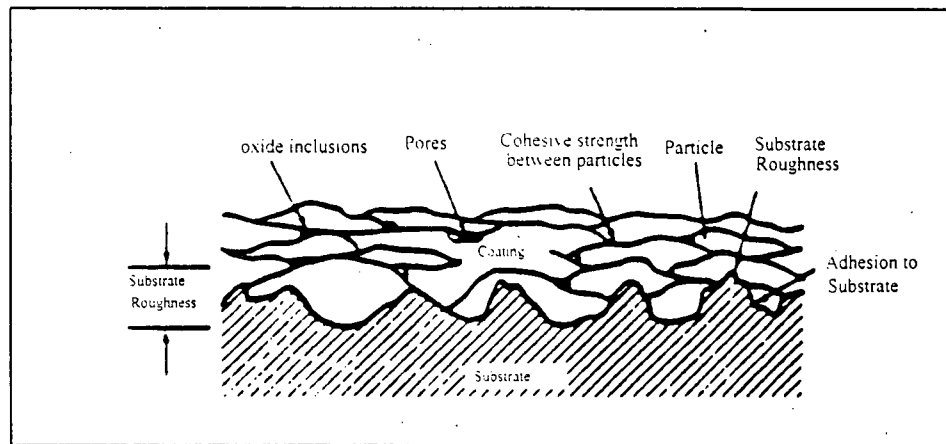


Fig 4: Schematic microstructure of the cross section of a thermal spray coating [8].

any ceramic, cermet or metallic material as well as some polymeric materials that melt without decomposing can be used to make a coating.

In a wire spray gun, Fig. 5, a wire 3 to 5 mm in diameter is fed into a multi-jet combustion flame by using a variable speed motor [1]. The tip of the wire melts and the gas jet strips the molten droplet from the wire and deposits it on the substrate at a speed up to 100 m/s. Wire spraying equipment is portable and the guns can be used manually making them attractive for on-site applications. However, the low temperature of processing and low deposition velocity reduces the bond strength of the thus formed coatings [2].

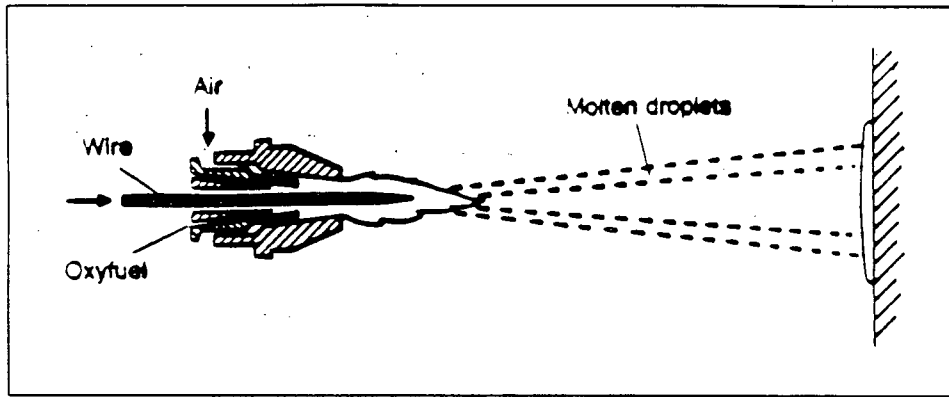


Fig. 5: Schematic diagram of a combustion wire spray gun [1].

In flame spraying, Figure 6, the combustion gases are mixed and burnt in an annular region around a central powder injector. The powder is generally fed by gravity, and depending on their morphology and composition, becomes partially or fully molten and acquire velocities up to 100 m/s. With a temperature of  $\sim 3000$  K, the oxy-fuel flame can melt most materials but the spraying efficiency of this process is low ( $\approx 30-40\%$ ).

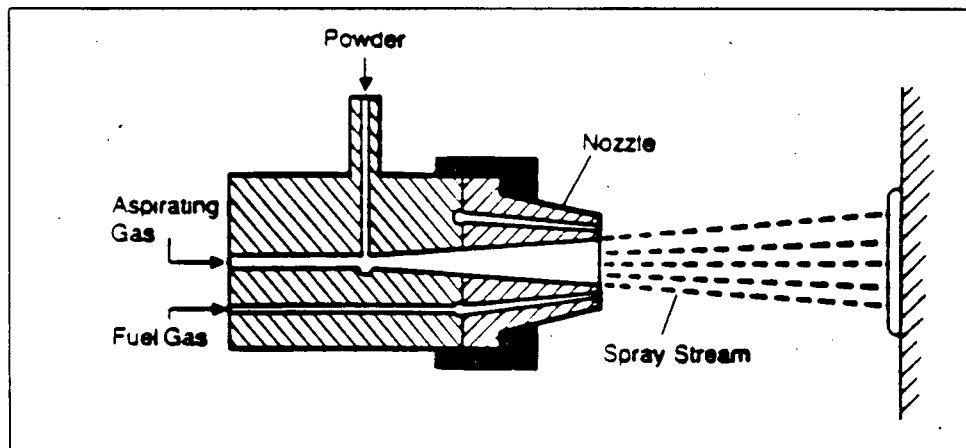


Fig. 6: Schematic diagram of a powder combustion flame spray process [4].

Detonation gun (D-Gun), which is one of the most successful high velocity thermal spray processes, is run by controlled detonation of oxy-acetylene mixtures. The schematic sketch of a D-Gun, as shown in Fig. 7, consists of a barrel 1 to 1.5 m long into

which the gas mixture is injected and ignited by a spark plug. When a critical temperature is reached, a self ignition process produces a detonation wave. The shock wave travels at velocities of  $\sim 3000$  m/s with a temperature of  $\sim 3500$  K. The bond strength achievable at the interface with D-Guns is higher compared to that obtained by other thermal spray units. One of the main limitations of the D-Gun is the higher residual stress it induces into the coating and or substrate interface compared to the other thermal spraying methods. This causes a significant reduction in fatigue strength of certain substrates [1].

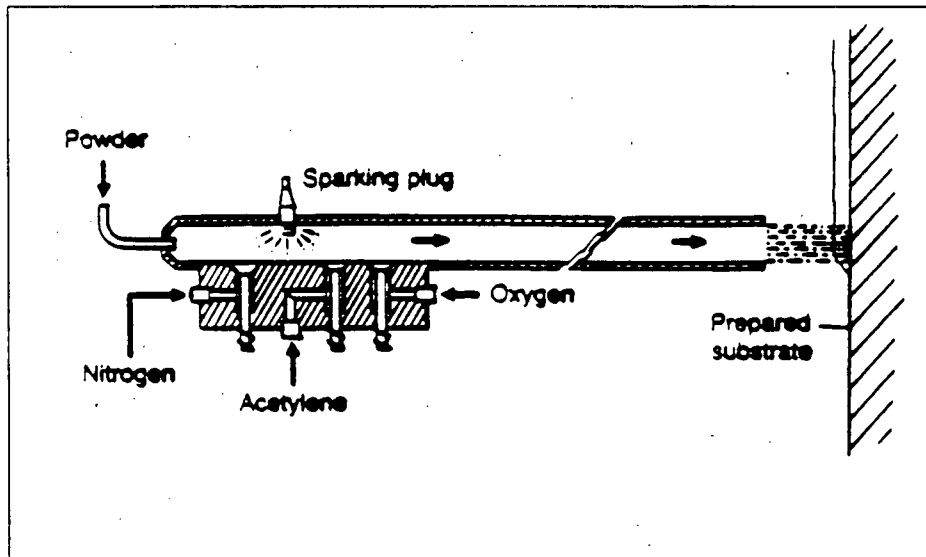


Fig. 7: Schematic of a detonation gun [1].

a) Plasma Spraying

Plasma Spraying is one of the most advanced thermal spraying methods. In the process of plasma spraying, a non-transferred arc is used in the torches where the nozzle of the torch serves as the anode. Figure 8 shows a typical plasma torch with an axial

powder feed. The nozzle has a diameter slightly smaller than the free burning arc. This constricted arc can have high current e.g. 1000 A at 80 V DC, and temperatures up to 15,000K. Gases passing through the arc are heated, dissociated, ionized and emerge from the nozzle as plasma with velocity greater than 300 m/s. Most devices use nitrogen, argon and helium with some addition of hydrogen which increases the plasma enthalpy and temperature. This process with its medium to high velocity of spraying and high temperature of the plasma produces coatings with high bond strength. Further, the high spraying efficiency and deposition rate enable it to be used for coating large components.

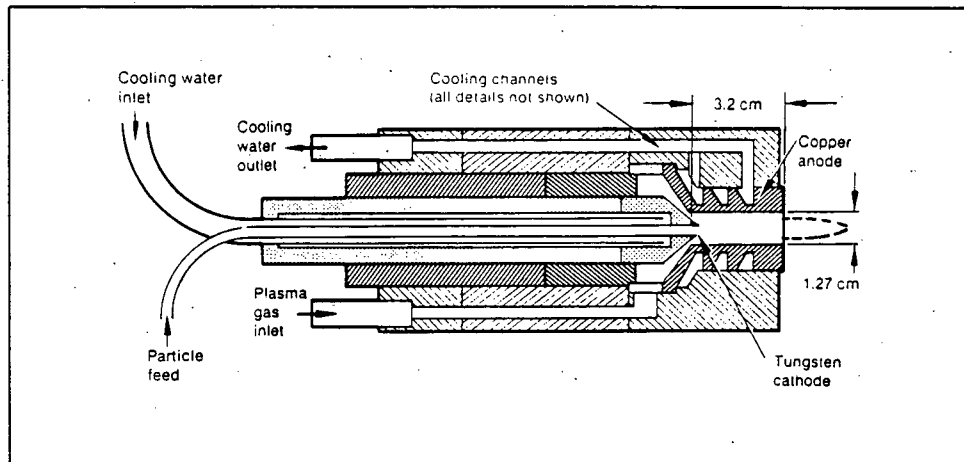


Fig. 8: Schematic of an axial powder feed plasma torch.

Heat transfer from plasma jets to the entrained particles depends on the temperature history of the particles moving along their trajectories, on the heat transfer coefficient from the gas and on the gas enthalpy. The gas enthalpy is related to the atomic structure of the molecule. For example, in the case of diatomic molecules additional energy is obtained from the recombination of the dissociated molecules as well as the ions and electrons,



Under identical operating parameters the efficiency of a torch depends on the way powder is fed into the plasma jet. There are broadly two types of powder feeders available for the commercially used plasma torches. Radial Feeder has the powder fed at an angle (usually ninety degrees) to the direction of the plasma jet as shown in Fig. 9. For this type of torch, a careful adjustment of the carrier gas and plasma jet is required to ensure that the bulk of the injected powder stays within the plasma plume and is ultimately deposited. However, even with the best control, a spraying efficiency higher than 40 wt% of the fed powder is rarely obtained for radial fed torches [12]. In the case

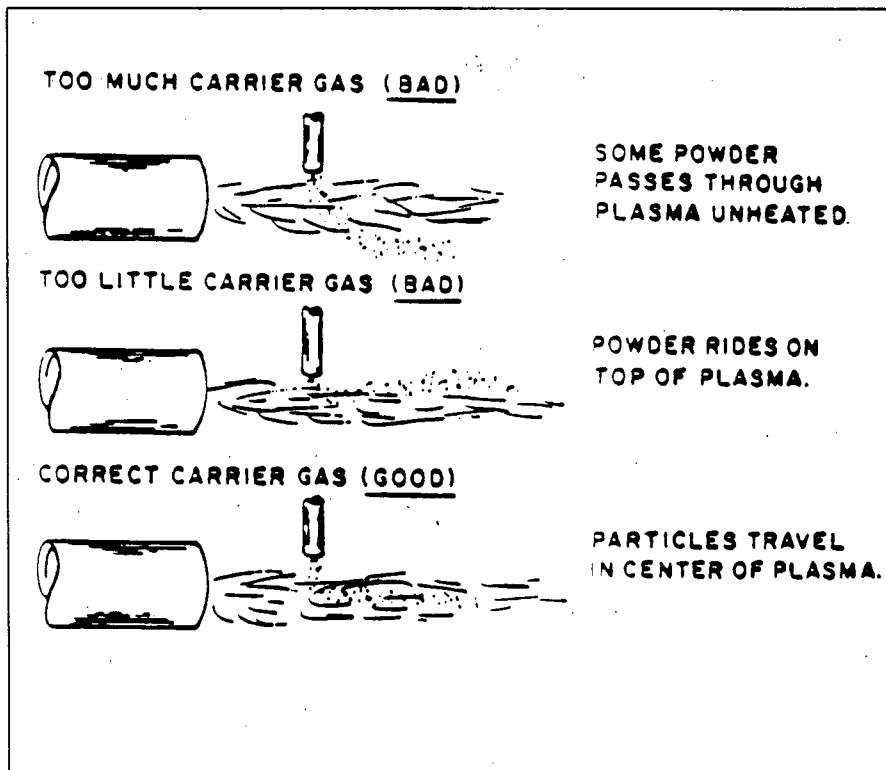


Fig. 9: Effect of powder injection velocity in the plasma jet with radial feed [4].

of an Axial Feeder, powders are injected along the axial direction, i.e. in the direction of travel of the plasma jet. This eliminates the negative effect of radial powder injection on laminar flow of plasma, resulting in lower turbulence in the free expanding plume outside the nozzle. Thus, it allows higher gas and particle velocity. The reduced turbulence allows a higher feed rate and spray rates are 100 to 200% higher than that achievable with radial feeders. The nearly full entrapment of the powders within the plume allows deposition efficiency as high as 95% and coating costs are reduced by 50 to 60% compared to the radial feeders [12].

Plasma spraying is used to produce coatings for a variety of applications. They are mainly used as protective coatings to improve the wear and corrosion resistance of the material and in some cases to improve the optical, electronic/electrical or thermal properties. Wear and antifretting resistance is imparted to a material by applying a harder and more wear resistant material than the substrate. Corrosion resistance, especially in marine or other corrosive atmosphere is imparted by spraying an inert material, usually a ceramic, on the component. Thermal barrier coatings are applied on high temperature components like in aircraft engines, where the metallic superalloy components are coated with a high temperature ceramic. This allows a higher operating temperature. Coatings of electrically conductive (e.g. Cu) or insulative materials usually ceramics, are applied on substrates to impart their respective electrical properties. Plasma sprayed coatings are often used to restore dimensions of worn out components and also in medical devices to make them inert. Thus, the use of plasma spraying can be classified in the following three categories [37]: manufacturing (e.g. automobiles), infrastructure repairs (e.g. paper mills and petrochemical industries) and high technology (e.g. aircraft). Depending on the

use and properties required the type of materials to be sprayed are selected. The commonly sprayed materials and their uses are summarized in Table 1.

**Table 1:** Plasma Sprayed Materials and their Uses [37]

<b>Materials</b>	<b>Uses</b>
<b>Metals</b> Aluminum Stainless Steel Chromium Titanium	Surface Repair Sliding Wear Resistance Corrosion Resistance
<b>Cermets</b> WC-Co Ti-TiN Al-SiC/Al <sub>2</sub> O <sub>3</sub>	Corrosion Resistance Erosion Resistance Sliding Wear Resistance Spray Forming
<b>Ceramics</b> Cr <sub>2</sub> O <sub>3</sub> TiO <sub>2</sub> Al <sub>2</sub> O <sub>3</sub> ZrO <sub>2</sub>	Corrosion & Erosion Resistance Sliding Wear Resistance High Temperature Wear Thermal Barriers

The calculation of the economics of the process of plasma spraying is a complicated procedure and is done by considering the number of years the coating performs, the reduction in maintenance cost it provides, the reduction in scheduled or unscheduled down time, associated loss of production along with the improvement in the quality of the product being processed [2]. Frequently, in the case of thermal spray coatings, the substrate preparation (grit blasting), fixturing and tooling, and/or finishing of a coated component costs more than the actual coating itself. With all the above factors an approximate estimate of the commonly used coatings has been provided by Tucker [2], where the deposition cost of plasma sprayed coatings is found to vary

between 0.002 and 0.05  $\$/(\mu\text{m cm}^2)$ . This value is dependent on the cost of the spraying powder, although, generally it is seen that the powders with higher initial cost has the least total cost when all the other factors are considered.

## Chapter 2: Literature Review

### 2.1 *Al-SiC systems*

#### 2.1.1 Background of Al-SiC system

Light metals like aluminum, titanium, magnesium are gaining use as structural materials in engineering components. Their low density combined with reasonable tensile strength and ductility have led to their extensive use in the field of aviation and automotive industries. Among these metals, the high strength aluminum alloys, namely the 2xxx series (Cu alloyed), 6xxx series (Mg, Si alloyed), and 7xxx series (Zn alloyed) are gaining popularity because of higher tensile strength than pure Al. One of the limitations of the high strength aluminum alloys is their relatively low elastic modulus compared to other structural alloy systems, e.g. steel and titanium alloys [13].

To overcome this problem, the metal matrix composites (MMC) were first used by the aerospace industry to obtain a higher Young's modulus and strength to weight ratio for the airframe structures [7]. The introduction of a ceramic phase as reinforcement in the form of particulate, whisker or fiber not only improves the strength of the material at room and elevated temperatures but also the wear resistance of the material. Among the various types of reinforcements such as oxides and carbides, the monocarbides of groups IV, V and VI metals like SiC and TiC exhibit exceptional properties such as high hardness, wear resistance and melting point [8]. However, amongst these SiC having a density ( $d=3.2 \text{ g/cc}$ ) close to that of Al ( $d=2.7\text{g/cc}$ ) is the most commonly used reinforcement. The insertion of these carbides in the ductile matrix improves the failure

strength by deviating the propagating crack and increasing the crack path [5]. This enhances the elastic modulus and wear resistance of the material. However, the addition of the ceramic phase reduces the ductility of the material depending on the content of the reinforcement. The ceramic does not contribute much to the strength of the MMC in the high temperature range as these particles are usually too coarse ( $>3\mu\text{m}$ ) to dispersion harden the material [20].

The amount of second phase that can be incorporated into the composite through the conventional routes of casting or powder metallurgy (PM) is limited by the wettability between the Al matrix and the second phase particle. The PM technique is also limited by the sinterability of the system [9]. Hence, the commercially available cast or sintered particulate composites usually have the content of the second phase limited to less than 30 vol% [9]. An additional problem is microstructural optimization of the MMC. For example, one of the main difficulties in producing an Al-based MMC through powder metallurgy is the tendency to agglomerate the reinforcement particles [9]. The primary reason for this phenomenon is the difference in size of the powders of the matrix and the second phase particles [6,7]. The variation in interparticle distance between the second phase particles is directly proportional to the ratio of the matrix to reinforcement particle size. Development of static charge on the surface of the nonmetallic reinforcements leads to agglomeration of SiC in the Al matrix [7].

Owing to the above mentioned difficulties in obtaining a homogeneous microstructure of a composite, manufacturing a structural component out of MMC is not always economically viable. Hence, for the components where the tribological (wear

resistant) properties are more critical than the structural strength, thermal sprayed coatings are preferred. The choice of the coating material for monolithic Al component depends on various factors. Ceramics have the best wear resistance but they reduce the ductility of and induce residual stresses within the Al component. Hence, MMC coatings are desired as they retain the ductility while providing a wear resistance. The WC/Co (tungsten carbide-cobalt) system, although most widely used MMC coating with high hardness and acceptable oxidation/corrosion resistance behavior, has drawbacks of its own. The high density of WC/Co ( $d \approx 13.5$  g/cc) does not make them optimal coatings for many of the lightweight aluminum structures ( $d \approx 2.7$  g/cc). Moreover the cost of using WC/Co coatings is relatively high, approximately US \$500/m<sup>2</sup> for a 250  $\mu$ m thick coating with a 65% spraying efficiency [8]. Compared to this, the density of the Al-SiC coating systems have density of 2.7-3.2 g/cc, depending on the SiC content of the Al-SiC coatings and therefore costs 4 to 5 times less for the same volume and spraying efficiency.

### 2.1.2 Wear properties of Al-SiC composites

The classic Archard's law states that the wear rate of a material is generally inversely proportional to the hardness of the material [10-11, 46]. The wear resistance of Al-SiC systems has been found to be superior, for both dry and lubricated sliding wear to that exhibited by Al. At low wear rates the composites are superior by a factor between 2 and 5 [6]. Chung et. al [11] reported that the hard particles enhanced the wear resistance by reducing the plastic flow in Al alloy matrices. The real advantage of the composites

compared to Al is found at higher loads when the wear resistance is better by a factor between 16 and 50 [10]. However, the coefficient of friction ( $\mu$ ) for the composites is always higher than that of Al [9].

Venkatraman et. al [10] found that Archard's law is maintained for the Al-SiC system under dry sliding wear conditions. Hardness and wear resistance increased with increasing SiC content, although the relationship was not linear. At low SiC contents (vol% SiC  $\leq$  10) the wear rate decreases much faster than the corresponding increase in hardness. The reverse trend was reported by the same authors for higher SiC content where the increase of SiC content from 30 to 40 vol% increased the hardness by 20% but the wear rates remained the same. Hwang et. al [11] also further observed that the increase in SiC particle size increased the wear resistance. The SiC particles reinforce the Al matrix and provide an extra wear resistance against rubbing of both contact surfaces and the trapped wear debris. The matrix, being softer than the SiC, wears out faster leaving the SiC particles projected out of the matrix surface. Thus, one of the main criteria for further wear to take place in these composites is the removal of the SiC particles. Hwang et. al suggested three possible mechanisms for the SiC to break loose from the surface: 1) brittle fracture, 2) pull out from the matrix, or 3) burial in the Al alloy matrix and being carried away when the latter detaches [11].

## **2.2 Powder Production for Plasma Spraying**

### **2.2.1 Powder Characteristics**

One of the most important factors in obtaining a good plasma sprayed coating is

quality of the powder which is being used for spraying [12]. Many powders of apparently same composition, but obtained from different sources, vary widely in quality and hence produce different coating qualities. Clogging of the powder in the powder feeder lines, poor deposition rates and cracked (or spalled) deposits are some of the common problems which arise due to poor powder quality.

Boulos et. al [12] suggested a number of properties like chemical composition, morphology and constitution to characterize the powder quality. The powders are characterized chemically, based on the average and local content of the elements, the constituents and impurities, and the homogeneity of the powder. The characterization of the morphology is based on the powder aggregate and individual particle traits which include the powder fineness, shape and microstructure of the particles. The characterization on the constitution is based on the phase structures and chemical composition of the powders. The above few traits of the powder decide on the thermo-physical properties like the heat transfer and the heat conductivity of the powders. This, in turn, controls the spraying quality of the powder.

For a given Al-SiC system the chemical composition of the powder is of profound importance. The composition of the matrix material determines its strength and also the wettability of SiC reinforcements. The homogeneity of SiC in the matrix decides on the ultimate distribution of the reinforcements in the coatings.

The powder morphology is determined by the shape of the particles. The shape and size of the particles decide on the flowability of the powder, which is critical to obtain uniform feed in the plasma plume. Flowability can be defined as the ease with which individual particles can slide across each other in a shear action. Thus, the

resistance of a powder to flow can be thought of as a shear strength and can be used to measure the flowability. The resistance to the shear arises from a variety of factors which include Van Der Waal's forces, electrostatics, chemical bonding, mechanical interlocking, etc. Almost all the factors controlling flowability depend on the total surface area available and hence on the powder sizes. Thus for the same processing conditions of the powder, the finer the particles lower is their flowability. Irregular shaped particles tend to show a low flowability due to easy mechanical interlocking between the particles. Thus, spherical particles with a narrow size range distribution show the best flow characteristics and thus are most suitable for plasma spraying.

### 2.2.2 Powder Manufacturing Techniques

The wear resistance, ductility and fracture toughness of the Al-SiC coatings are critically dependent on the homogeneity of distribution of the SiC in the powders. The main processes which are used for producing the Al-SiC composite powders include: i) mechanical blending ii) fusing and crushing iii) agglomeration and sintering iv) agglomeration and plasma densification and v) mechanical alloying [12-14]. The powders vary from irregular to spherical, porous to dense and from large irregular reinforcements to fine uniformly distributed ones [13]. The process of mechanical blending can be used when only one of the components of the powder cold weld and all the constituents of the powder are of similar density for e.g. Ti ( $d = 4.50 \text{ g/cc}$ ) and TiC ( $d = 4.93 \text{ g/cc}$ ) [8]. Even with very close densities, the powders sprayed by this method produce some segregation. Intermetallics like  $\text{MoSi}_2$ , NiCr, etc. powders are made by the fused crushed technique. The powders are made by Self Propagating High Temperature

Synthesis (SHS) technique and then crushed and sieved for the required particle size fraction. The agglomerated - sintered process is generally used for the ceramic powders where low density ingots are produced and are crushed and sieved for the required particle size fraction. The agglomeration followed by plasma densification process has been used for producing intermetallics NiAl [48], Al-Li based composites [15]. In this process, the premixed powders are fed into a plasma torch and the molten powders are collected in water. The particles are generally of uniform size and spherical in shape. Mechanical alloying is one of the most common method of manufacturing MMC powders and is used for blends which have at least one ductile component as its constituent. All these processes result in a variety of powder morphologies, compositions and structures.

For blends there is no actual bonding between the constituents and leads to carbide segregation and results in poor bonding between the matrix material and the carbides in the coating [8]. To avoid segregation submicron sized SiC ( $\approx 0.8\mu\text{m}$ ) was used by Khor et. al [15] along with specialized blending processes which included a combination of fluidized bed, spray drying and ball milling. However, the number of multiple steps involved in blending along with the fine size of SiC/AlN particles used, made the process more expensive than the alternative methods.

In the case of fused - crushed or sintered - milled powders the particles are dense but angular in shape which reduces the flowability of the powders. The process of sintering results in inhomogeneous distribution of the carbides when the size of the dispersed carbides was small ( $< 5\mu\text{m}$ ) or for compositions greater than 40 vol% SiC. It

has been determined that the movement of grain boundaries during the sintering stage results in segregation of the carbides [16].

Although the process of agglomeration and plasma densification yield better qualities of the powder, there is still the possibility of oxygen pickup by aluminum while plasma forming.

Compared to the processes mentioned above, the process of mechanical alloying has a few distinct advantages in the production of Al-SiC composite powders. The process produces powder with a homogeneous distribution of SiC in Al matrix [17, 20-22]. Mechanical alloying of the composites with suitable Process Control Agents produces powders which are spherical in shape [20]. Besides, the refinement of microstructures that occurs during the process of mechanical alloying allows the formation of supersaturated compositions of the matrix alloy which would not be possible by the conventional melting and casting techniques [17]. Thus, the process of mechanical alloying is one of the most commonly used powder metallurgy technique for producing Al-SiC composite powders.

### ***2.3 The Process of Mechanical Alloying***

#### **2.3.1 Background**

Mechanical alloying (MA) is a high energy, dry milling technique which produces composite metal powders with submicron homogeneity [17]. The driving force behind the development of this process was to combine nickel based superalloys with the high temperature strength of oxide dispersions. However, MA is not limited to producing oxide dispersion strengthened (ODS) alloys. Since the entire processing takes place in

solid state, it can produce alloys that are otherwise impossible to produce by the conventional melting and casting techniques [18]. The alloys are based on nickel, iron and other high temperature metals and contain alloying elements such as chromium, aluminum and titanium for corrosion resistance. In some cases, the latter two elements (Al & Ti) combine to form intermetallics which are responsible for high strength at an intermediate temperature.

MA has been increasingly employed in the development of metal matrix composites because it leads to an uniform distribution of the ceramic reinforcements along with the alloying of the elemental powders [19-21]. In the conventional casting techniques, the problem of wettability of Al with SiC limit the maximum content of SiC particles in the powder. Obtaining the composites through powder metallurgy techniques are limited by the grain boundary movement during the process of sintering [16]. Thus, the only way to obtain reinforcements greater than 30 vol% is with the use of mechanical alloying. Mechanical alloying of MMC has been used to achieve reinforcement contents from 5 to 40 vol% [16-20]. The reinforcements used are of the particulate type or whiskers and their sizes varied from 5 to 100  $\mu\text{m}$  [16-20].

### 2.3.2 Mechanism of Mechanical Alloying

The fundamental mechanism of MA is repeated cold welding, fracturing and rewelding of powders in dry state in a high energy ball mill [18]. The process can achieve completion when the rates of welding and fracture are balanced. Therefore, after a certain time of milling the average particle size remains relatively constant. The

process differs from the low energy conventional ball milling, as the latter gradually reduces the size of the powder particles with fracture being the dominant phenomenon. The competing process of cold welding also takes place in the conventional milling, but is limited by the low energy of the process and the use of milling fluids and surfactants [18].

One of the commonly used mills for the process of mechanical alloying is the high energy Szegvari attritor as shown in Fig. 10. In this mill the ball charge is rotated by impellers protruding from a vertical central shaft. The capacity of the attritors typically range from 1.0 to 100 gallons (3.75 to 375.0 l) and can be rotated to speeds up to 750 rpm [18,19,21]. The run time for a full charge of powders (approximately 500 g for a 6 litre attritor) is 8 to 10 hr. for complete alloying of the powders.

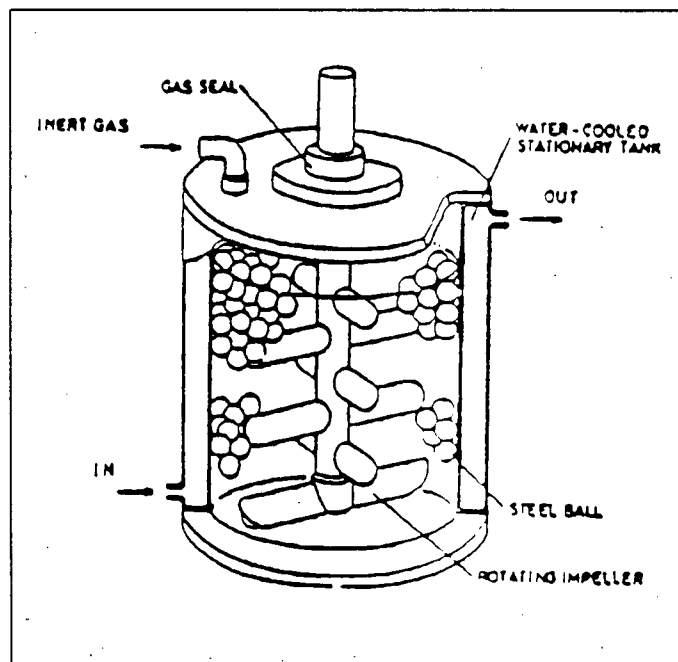


Fig. 10: Schematic of the high energy Szegvari attritor [24]

The “Fritsch Pulverisette” planetary ball mill are also commonly used for MA. These mills have vials set at the outer edge of a large rotating disc (typical diameter of  $\frac{1}{2}$  to 1m). The vials also rotate about their central axes upto speeds of 750 rpm [20,22,23]. The product of the two independent rotations cause high frequency and high energy collisions of the balls in the vials.

The configuration of another high energy mill (Fig. 11) is the vibratory type SPEX (trademark of the Sytech Corporation, Houston, TX) shaker mill. This unit produces small quantities (approximately 15 g) of powder in each cycle and grinding of ceramics like SiC, Al<sub>2</sub>O<sub>3</sub> to sub-micron sizes, typically takes less than an hour. The process involves the movement of the vial and balls at a high speed of approximately 1200 rpm (as quoted by manufacturer) in three mutually orthogonal directions [24].

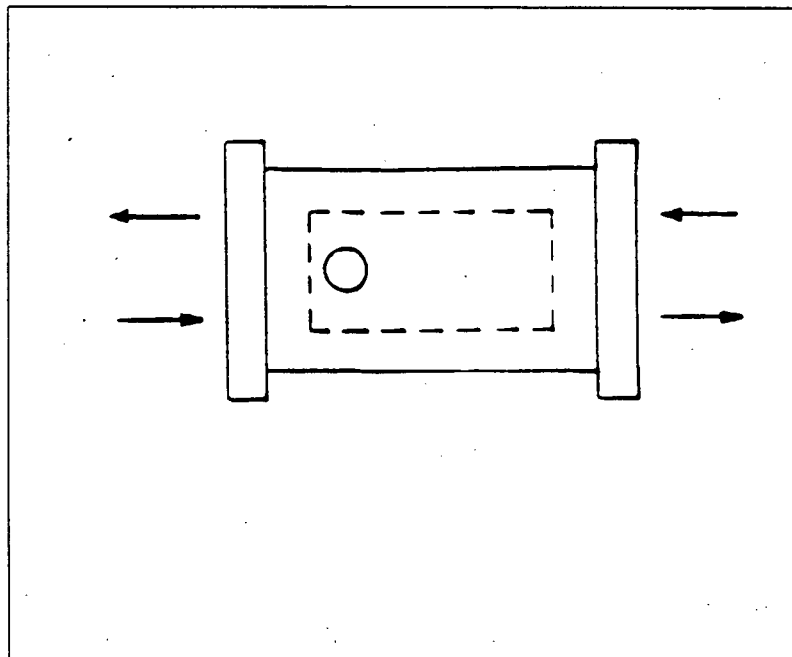


Fig. 11: Schematic of a SPEX shaker mill [24].

Conventional ball mills that rotate around a fixed central horizontal axis can also be used for mechanical alloying. To obtain the high energy of milling it should be of sufficiently large diameter ( $> 1$  m) and the mill should be operated just below the critical speed [17,18, 24]. The ball charge in mechanical alloying usually contains ASI 52100-bearing steel grinding balls with a composition of - 1.04 wt%C, 0.35wt%Mn, 0.25wt%Si, 1.45wt%Cr and rest Fe. The high content of the Cr and C provides high wear resistance and hardness ( $R_c$  60 to 64) to the ball material. The ball charge to powder ratio is varied between 15 and 30.

### 2.3.3 Structural Developments in Mechanical Alloying

The process of mechanical alloying starts from blending individual powder constituents where the diameter of the particles can range from 1 to 500  $\mu\text{m}$  [18]. The powder blend depends on the alloy to be processed and has one or more ductile metal constituents which act as the matrix. During MA, the greatest number of collision events are of the ball-powder-ball type where the powders are deformed between the colliding balls. A single collision between two balls affects the entrapped particles in two ways: either in a coalescence or fracture of the material, as shown in Fig. 12 [18]. High strain rate (dynamic) fracture is favored for normal impact. When the angle of impaction changes, other fracture modes such as forging fracture and shear fracture may occur. Cold welding takes place only when there is normal impact between the two colliding balls, resulting in a direct seizure. As the material is flattened, the surface film present on the particles ruptures. This brings atomically clean surface areas into contact and cold

welding results. Indirect seizure is said to occur when the deformation is preceded by sliding displacement and occurs for low angles of impact (Fig. 12).

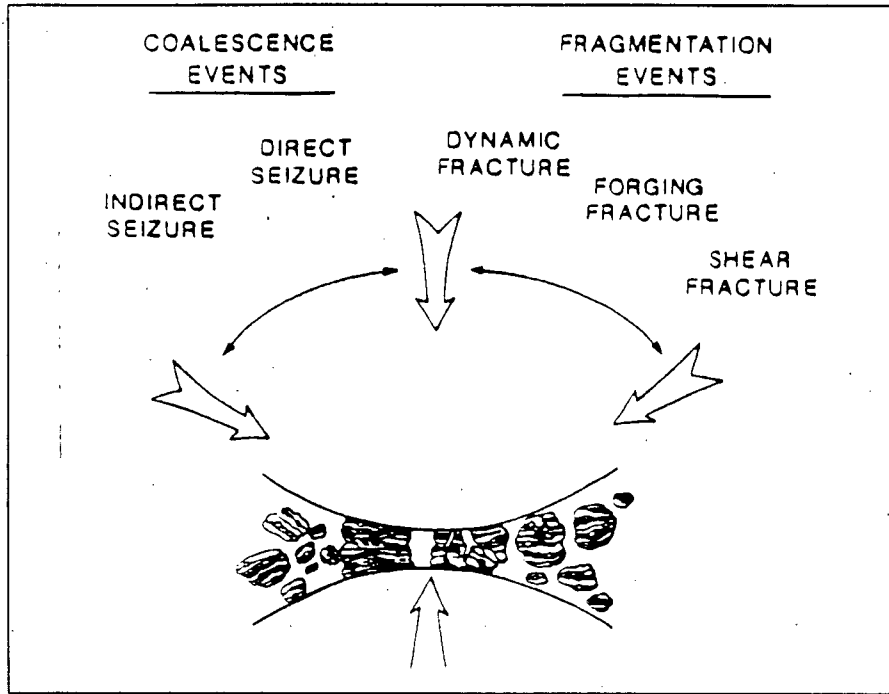


Fig. 12: Schematic illustration of the repeated fragmentation and coalescence processes that characterize MA [24].

For mechanically alloyed ductile Al the repeated flattening of the particles results in strain hardening. In addition to the cumulative strain, the high strain rate of deformation accompanying the collisions results in an accumulation of stress [24]. The stress within the material as a result of the collisions is given by [54]:

$$\sigma = K\varepsilon^n + C(\varepsilon')^m \quad (2)$$

where,  $\sigma$  = Stress within the material,

$\varepsilon$  = Strain in the material,

$\varepsilon'$  = Deformation strain rate.

$n$  = Strain hardening coefficient,

$m$  = Strain rate sensitivity of the material,

$K, C$  are constants depending on the material properties.

It has been shown that the contact surface between the balls and powder has a high coefficient of friction. Ashby and Lim empirically obtained coefficient of friction ( $\mu$ ) values as high as 1.0 during similar conditions in steel [53]. This high friction further increases with time of milling due to the adhesion of Al on the grinding balls which makes the surface progressively rough. Benjamin et. al [18] estimated that for a ductile metal like Al 3-4 wt% of the material is lost due to the adhesion on the surface of the balls. Due to friction between the balls and the material, the powder particles adjacent to the balls do not undergo much deformation as shown in Figure 13. The shaded areas represent the zones which undergo little deformation owing to the friction. The barreling of the cylindrical pellet between the two balls generate a tensile strain perpendicular to the direction of collision.

#### 2.3.4 Process Control Agents

In the case of a ductile metal like Al, the powders cold weld easily and thus it becomes difficult to control the mechanical alloying. Fracture is prevented by the dominant process of cold welding and hence the balance between cold welding and fracture is not obtained. Thus, mechanical alloying of Al powder results only in an agglomeration of the Al particles and the control over the size and microstructure of the particles is lost. To reduce the tendency of cold welding two different techniques are

used. Process control agents (PCA) which are organic surfactants have been commonly used for this purpose [18,20,26,27]. They are generally used in small amounts, e.g. 1-3 wt% of the total powder charge. Nopcovax-22 [29], 1,2 bis-oxycarbonyl dodecyl ethane-1-sulphonate [27] and hexadecyl trimethyl ammonium bromide [27] are some of the reported process control agents. The PCA delays the cold welding and allows the material to work harden enough to fracture. During sintering of these powders, the organic compounds decompose and the carbon is adsorbed to form carbides. Reduction of the processing temperature has also been used to reduce ductility, promote fracture and simultaneously reduce the cold welding during mechanical alloying of extremely ductile elements, like Al. Singer et. al [28] reported an increase in rate of fracture during mechanical alloying of aluminum at  $-40^{\circ}\text{C}$ .

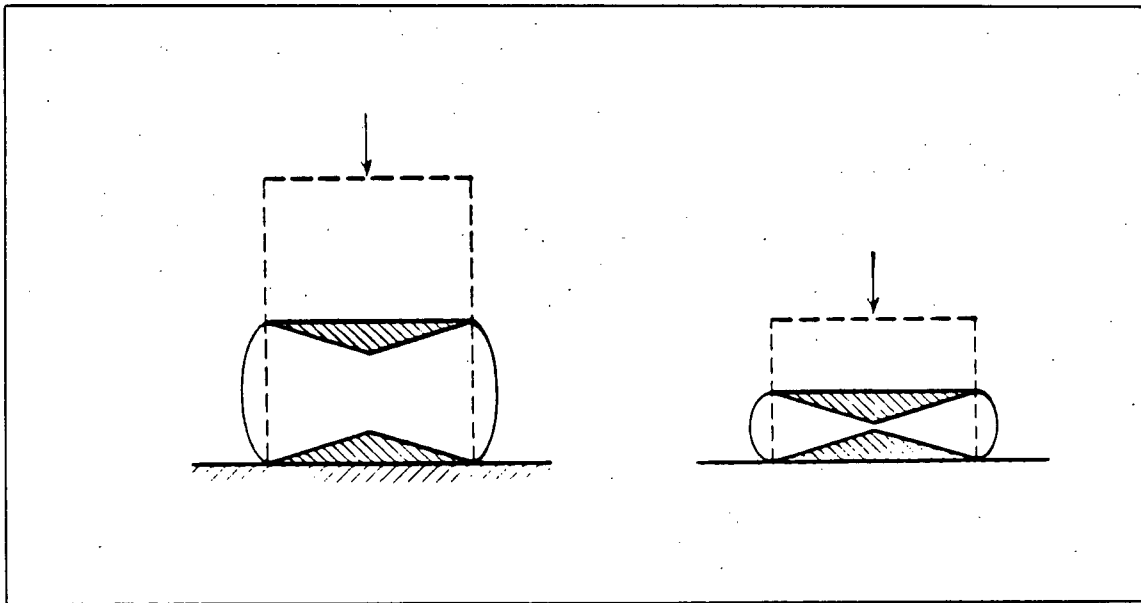


Fig. 13: Undeformed regions (shaded) due to friction during compressive specimen in a ductile material [54].

Lu et. al [20] reported that without the use of PCA the size of Al-SiC particles continuously increased with duration of milling. The composite powder also had a nonuniform distribution of SiC in the Al matrix. The use of PCA helped to homogenize the distribution and reduce the size of the original SiC particles. The reduction in size of the SiC phase was an effect of the reduced cold welding of Al which allows the collision energy to be absorbed by SiC. This results in fracture of SiC particles.

### 2.3.5 Physics of Mechanical Alloying

There are considerable gaps in the fundamental knowledge about the mechanism of MA and hence the theoretical prediction of the process is minimal. To determine the actual physical parameters governing the transition of morphology, the understanding of the physics of the process is essential. Maurice and Courtney [24] made the first attempt in understanding the physics of the process in which they assessed the powder-ball interactions for the common devices used in the process of mechanical alloying. This work helped in assessing the related parameters of the process like the impact velocity, volume of powder material impacted, frequency of collisions, etc. They reported that the velocity of the colliding balls is the most important parameter in determining the mechanics of the process.

Magini [29] used the difference in the potential energies of the colliding balls before and after the collisions to calculate the kinetic shock energy which is released into the powder from the balls. However, the shock frequency was not considered and hence the total amount of energy delivered could not be assessed. In the present investigation,

mechanical alloying was done using the SPEX mill and hence emphasis has been laid on the physics of this type of mill.

The impact velocity between the grinding balls in the SPEX shaker mill was reported by Maurice et. al [27] by using the empirically obtained operating conditions of the mill. The mill vibrates the charged container in three mutually perpendicular directions at approximately 1200 rpm. Since the magnitude of oscillation is much higher in one direction it can be viewed as a linear harmonic device oscillating with an amplitude of 5.7 cm. Through the first half of this distance the vial accelerates. When it starts to decelerate, the balls within the vial continue to travel with the maximum velocity of the vial. The maximum velocity is twice the average velocity and is given by

$$v = \frac{2x}{t} \quad (3)$$

where  $x$  is the distance traversed by the vial and  $t$  is the time of one complete to and fro motion of the vial. Using the specifications of the mill, this velocity was reported to be around 3.9 m/s [24]. In a comparable SPEX mill Davis et. al [30] approximated it to be around 6 m/s. This impact velocity is found to be an order of magnitude higher than that found in an attritor or planetary ball mill and hence the processing time for the powder is less in a SPEX mill (typically less than 1 hr.).

Abdellaoui et. al [22] have emphasized that kinetic shock energy and kinetic shock frequency are the most important parameters governing the process of mechanical alloying. But neither of the above two factors separately taken alone can determine the end-product of the process. Instead, the shock power which is the product of the shock frequency and shock energy governs the process.

The shock frequency is governed by the type of mill that is being used for the process. The shock energy has been calculated by assuming that collisions between the balls are completely elastic and the entire kinetic shock energy is released onto the powder. Maurice et. al [27] assumed the collisions followed Hertz theory of impact which assumes that no energy is dissipated during the collision. In a Hertzian collision, it is assumed that there is a gradual compression of the colliding balls and the energy is completely recovered following the impact i.e. the kinetic energy used in deforming the bodies becomes stored elastic energy as the bodies recover. The Hertzian impact theory is appropriate if the kinetic energy associated with the relative motion of the colliding bodies is much less than the elastic energy content of the bodies. This requirement is satisfied if the relative velocity of the colliding bodies is less than the speed of sound in the material. Since the speed of sound in metals are of the order of kilometers per second and the highest speed of the balls is of the order of 6 m/s, the Hertz theory of collisions are applicable to all the collisions that take place in the typical MA devices. Maurice et. al compared the collision of the two balls with the powder with upset forging between two parallel plates, Figure 14 [27]. The notation  $r_h$  is the Hertz radius of impact, as shown in the collision geometry in Fig. 14a. Since, this value is much less than the radius of the colliding balls, they can essentially be assumed to be between two parallel plates. The cylindrical pellet, of initial height  $h_0$ , comprises of individual particles entrapped between the two colliding surfaces. The Hertzian radii and the pellet height  $h_0$  are typically of the order of  $10^{-4}$  m in a SPEX mill, whereas the applied stress  $p$  is of the order of  $10^9$  N/m<sup>2</sup>. The velocity of the balls, shock frequency, shock energy and shock power are summarized in Table 2 [22].

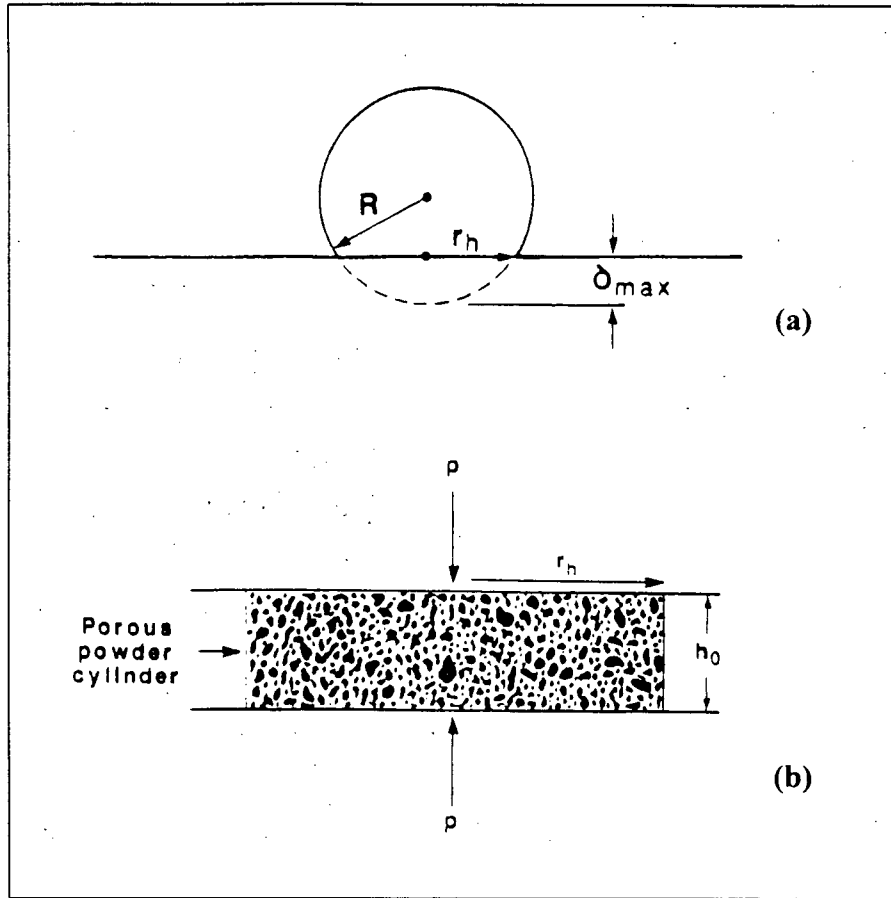


Fig. 14: a) Geometry of the ball at the time of collision. b) Upset forging event which is comparable to the collision between two balls with the powder in-between [27].

**Table (2).** Summary of the milling parameters of the machines commonly used [22].

	Attritor	Planetary ball mill	SPEX
Velocity of balls(m/s)	0-0.8	2.5-4	3.9
Kinetic Energy( $10^{-3}$ J/hit)	10	10-400	120
Shock frequency (Hz)	1000	100	200
Power (W/g. of ball)	0.001	0.01-0.08	0.24

## 2.4 The Plasma Spraying Process

In the case of plasma spraying in air (APS), the turbulent mixing of the plasma jet with the atmospheric gases reduces the plasma velocity and produces steep gradients in temperature profiles. The velocity of the plasma jet along the axis of the torch drops from 900 m/s at the nozzle mouth to 150 m/s at a distance of 100 mm. Similarly, the temperature drops from 12,400 K to 2,800 K for the same traversed distance. As a result of the interaction of the hot plasma with air, oxygen and nitrogen can react chemically with the sprayed particles. The oxides and nitrides thus formed are entrapped in the coating and affect the coating characteristics [8]. Controlled environment spraying such as vacuum plasma spraying (VPS) has been used to circumvent the problem of oxidation of reactive metallic elements like aluminum, copper, etc. [32]. This can also be done by using a shroud of inert gas surrounding the plasma [5].

The interaction of plasma gas with the powder particles depends on the heat and momentum transfer from the plasma to the particles. The total heat transfer from the plasma to the powder is decided by a number of factors, amongst which, the applied power of the torch and residence time of the powder in the flame are most important. The variation in the applied power controls the temperature of the plasma flame which can vary from 2,000 to 12,000°K. The residence time, decided by the carrier and plasma gas velocity, along with the temperature controls the total energy absorption possible by a powder particle in its flight path. The governing equation for the heat exchange of a single particle is given by [12]

$$Q = h.a.(T_{\infty} - T_s) - \sigma.\epsilon.a.(T_s^4 - T_a^4) \quad (4)$$

where,  $Q$  = Power input into the powder particle, [W].  
 $h$  = Heat transfer coefficient, [W/(m<sup>2</sup>°K)].  
 $a$  = Surface area of the particle, [m<sup>2</sup>].  
 $T_{\infty}$  = Temperature of plasma flame, [°K].  
 $T_s$  = Temperature on the surface of the powder particle, [°K].  
 $\sigma$  = Stefan-Boltzman constant,  $5.67 \times 10^{-8}$  W/m<sup>2</sup>.K<sup>4</sup>  
 $\varepsilon$  = Emissivity of the plasma  
 $T_a$  = Ambient temperature, [°K].

The first part of the equation determines the energy input to the particle through convection whereas the second part represents the energy loss through radiation. The input power, eq. (4), multiplied by the residence time of the particle determines the total energy intake of the powder in its path and thus the temperature of the powder. To obtain a homogeneous, dense coating it is important that there are no unmelted particles in the plasma flame. For the powder to completely melt in its flight path the following relation should be fulfilled [12] :

$$\int_0^t Q dt > m_p C_p (T_m - T_o) + m_p H_m \quad (5)$$

where,  $t$  = Residence time of the particle in the flame, [sec].  
 $m_p$  = Mass of powder particle, [kg].  
 $C_p$  = Heat capacity of powder, [J/mol.°K]  
 $T_m$  = Melting point of sprayed material, [°K].  
 $T_o$  = Original temperature of the powder, [°K].

$H_m$  = Enthalpy of melting of the powder particle, [J/kg].

In the above equation, the LHS is the product of the residence time and power input into the particle. Hence, it represents the total input energy into the particle. RHS indicates the heat required for the melting of a particle. The first term in RHS indicates the heat input required to heat the particle to its melting point, whereas the second term indicates the latent heat required for the melting. Thus eq. (5) indicates the condition for complete melting of the particle. As expected, ceramic materials having a higher melting point, require higher amount of energy for their complete melting whereas low melting metals, like Al, melt at low power levels.

Depending on the sprayed powder morphology and composition, the mechanisms of plasma spraying of cermet coatings can be broadly classified into two categories. Spraying can be done with either both the metallic and reinforcing phase in the molten state in the plasma flame or by only the metallic phase being in molten state. Plasma spraying of Al-Al<sub>2</sub>O<sub>3</sub> or Cu-Al<sub>2</sub>O<sub>3</sub> at higher power are examples where both the ceramic and metallic phase melt during spraying [33]. The reinforcing phase is mostly present in the solid state where the ceramic is carbide or nitride e.g. Al-SiC [5], Ti-TiC/TiN [4] or Ni-TiC [34].

Segregation during spraying has been reported for both the cases where the reinforcing phase is either in the molten or solid condition. For the materials where the ceramic phase remains solid during spraying, the main causes of segregation are the difference in density and lack of wettability between the reinforcing phase and the matrix [4, 33]. However, separation of phases was also seen in Cu-TiC system which shows a good wettability with the molten matrix [33]. If the reinforcing phase melts during

spraying segregation is due to the difference in surface tension of the two liquids. Fukumoto et. al. [33] also found a correlation between segregation within the coatings and the spraying distance. This was obtained by varying the spraying distance during the spraying of Cu-Al<sub>2</sub>O<sub>3</sub> MMC powder between 100 and 300 mm while spraying into water. Spraying into water helps minimize segregation due to lower deceleration upon impact compared to that on a rigid substrate. The morphology and SiC distribution in the molten powder is retained by quenching in water. It was found that the plasma gas on emerging from the nozzle creates an acceleration zone, followed by a deceleration zone which is experienced by the powder particles in their flight path, as shown in Fig. 15 [33].

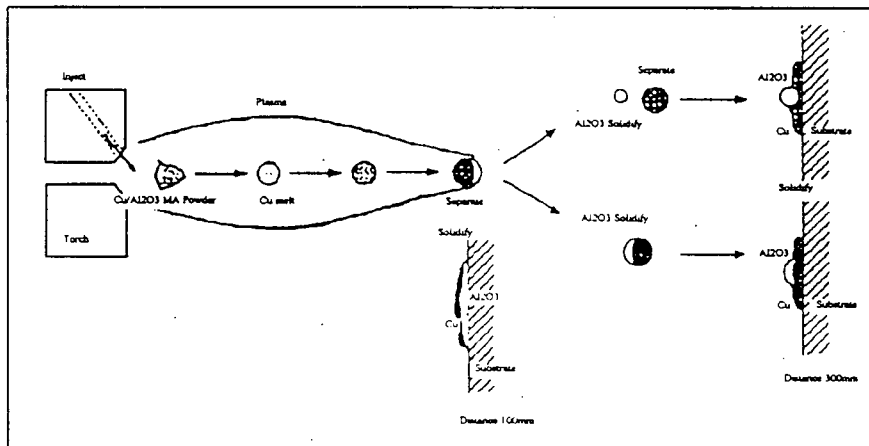


Fig. 15: Schematic mechanism of separation in plasma sprayed MA composite powder [33].

## 2.5 Coating Adhesion Tests

The adhesion strength between the coating and substrate is one of the most important properties of the system, determining its lifetime and overall quality [35, 36]. Adhesion is affected by a host of variables including powder and torch parameters,

surface preparation and substrate heating [37]. Numerous tests are used to evaluate the adhesion strength of thermal sprayed coatings. However, none is universally acceptable [35-37]. The fundamental problem in investigating adhesion is selection of a parameter which characterizes the strength of an interface. The best test method is often the one that simulates stress conditions found in practical applications of the coating. Thus, although there are many accepted tests [36], industry uses few tests amongst which the tensile adhesion test (TAT) also known as the pull test, is the most commonly accepted one.

#### 2.5.1 The Tensile Adhesion Test (TAT)

The TAT is relatively simple to perform and widely used in industries and laboratories as a routine quality control tool for thermal sprayed coatings. The TAT has been standardized, e.g. in ASTM C633-79. The arrangement for the ASTM test is shown in Fig. 16. A coated specimen is attached to a support fixture by epoxy so that a tensile force can be applied. The stress at failure, calculated as load over the area of the coating, is called the tensile adhesion strength or bond strength. Despite the standardization, some shortcomings of TAT include the possibility of epoxy penetration into the coating, misalignment of the test fixtures and fracture through the coating or coating/epoxy interface. TAT is also sensitive to local flaws, especially at coating/substrate interface close to the edge of the specimen.

#### 2.5.2 The Peel Adhesion Test

To overcome the inconclusive nature of TAT, the peel adhesion test (PAT) was developed at UBC by Sexsmith et. al. [39 - 44], which had the predictive ability of the

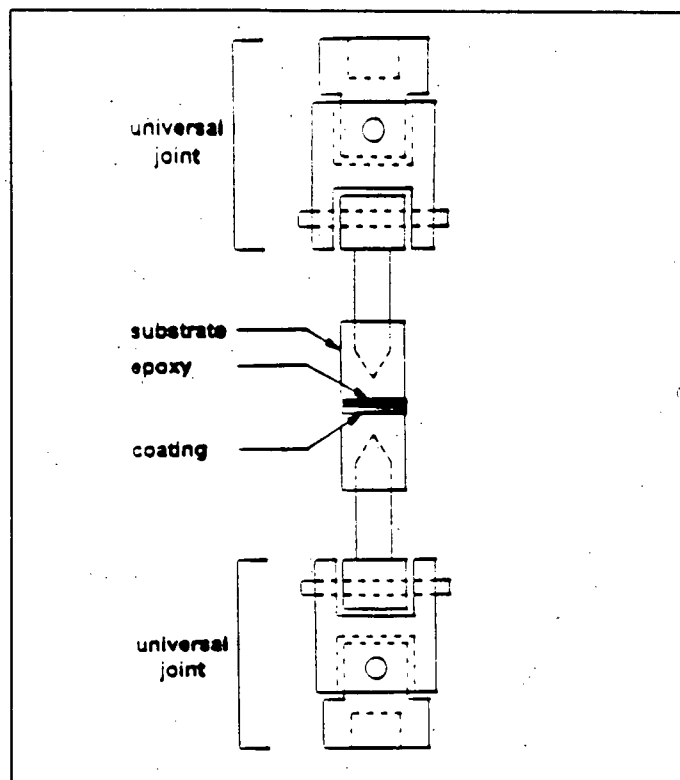


Fig. 16: Schematic of the Tensile Adhesion Test [39].

fracture mechanics tests and the simplicity of the force based tests. Peel test has been widely used to measure the adhesion of tapes and glues and also in microelectronics industries to measure the bonding of metal films to ceramics. Because of its widespread use there has been a number of studies into the mechanics of the process [49-52].

The process can be summarized as one where a thin adherent film or coating, is pulled from its substrate with a fixed geometry [39-44]. The schematic of peel test for thermal spray coatings is shown in Fig. 17. The force required to separate the foil from the substrate is recorded as a function of crack position. Because very little energy is stored in the bent foil, crack propagation is stable and controlled by the displacement of the sample. The peel strength is commonly reported as the force per unit width of the crack (N/m).

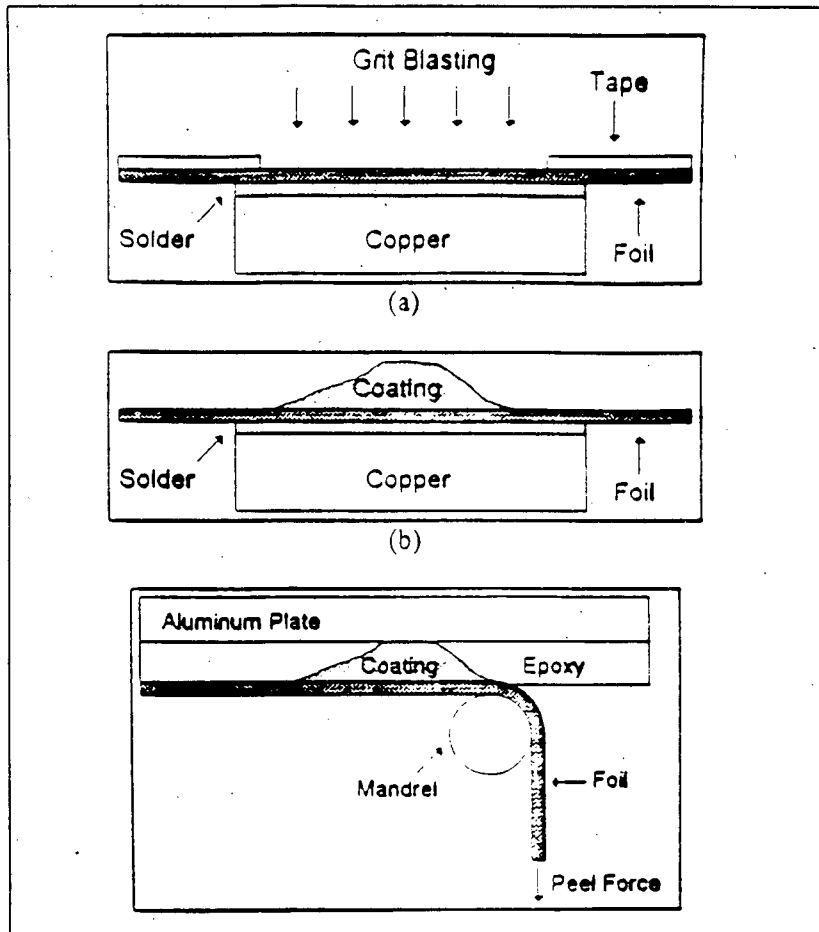


Fig. 17: Schematic diagram showing the steps in sample preparation for peel test [39].

There are several advantages of the peel test. It is relatively simple to perform and so is the equipment required for the test. Since the position of the crack is continuously monitored, the result shows the variation of the adhesion strength along the length of the coating and thus possibly the presence of local flaws. The test eliminates the requirement of expensive adhesives and the dependence on their performance.

The peel test has a few limitations of its own. The use of a thin foil is required to obtain stable fracture of the coating during peeling. A thicker foil has high stored elastic energy which causes unstable cracking. The thin foils are fragile and tend to overheat if

not properly bonded to the heat sink [39]. The residual stress generated from overheating of the substrate strongly affects the adhesion strength and coating properties.

## **2.6 Wear Tests**

### **2.6.1 Abrasive wear**

Laboratory experiments of abrasive wear are carried out to examine the mechanisms by which wear occurs or to simulate practical applications and provide useful design data on wear rates and coefficients of friction. Abrasive wear, which is common in machine components, takes place when two surfaces slide over each other and can be broadly classified into a) lubricated abrasive wear, which occurs when there is a lubricant present between the two mating surfaces and b) dry abrasive wear, where there is no lubricant as in two abrasive surfaces in air [40]. Since in Al-SiC composite, Al matrix has a lower hardness it gets abraded easily leaving the SiC particles exposed on the composite surface. Thus, for further wear to occur the reinforcing particles have to be removed. Chung et. al [11] suggested that can occur by one of the following three mechanisms - 1) brittle fracture of the reinforcements, 2) pullout of the reinforcement and 3) fracture of the matrix below the surface. The abrasive wear tests help in identifying the dominant one of these three mechanisms.

Many different experimental arrangements have been used to study abrasive wear. Fig. 18 shows the geometrical arrangements of the several common type of sliding wear testing machines. They can be classified into two types: those where both the wearing surfaces are similar and hence the wear is symmetrically disposed or the more common one where the wear is between two dissimilar surfaces.

The common test rigs for the asymmetric type of wear (for dissimilar surfaces) include a pin or block of constant cross sectional surface area against a disc or flat face under constant load. The contact area may be over an extended nominal contact area, e.g. a flat ended pin or block, or only a point or line as in the case of a round ended pin on a disc, as shown in Fig. 18.

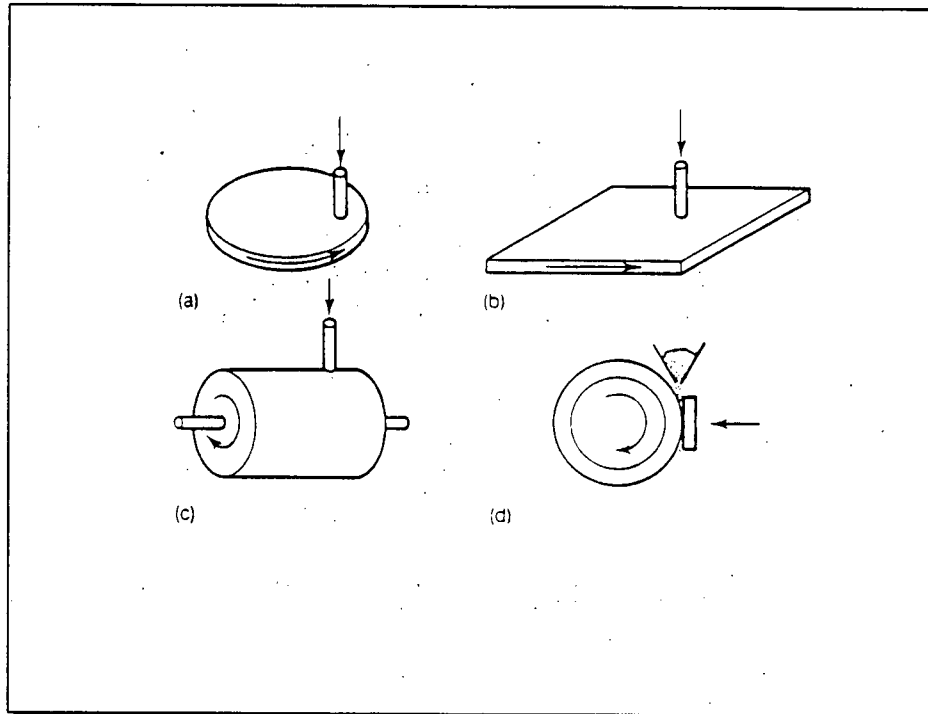


Fig. 18: Geometries employed in abrasive wear tests [40].

Wear under abrasive conditions depends not only on the sliding distance, but also on the sliding velocity [40]. The sliding velocity affects the rate of frictional energy dissipation and hence the temperature at the interface. Wear also depends on the nominal contact pressure between the sliding surfaces, as transition in mechanisms have been reported by changes in the contact pressure. The linear dimensions of the specimen also influence the wear result, since the wear debris are generally formed at the leading edge

of a long specimen. This will have more influence during its passage through the contact zone than it would have on a shorter specimen.

### 2.6.2 Erosion Wear

Solid particle erosion is said to occur when discrete solid particles impinge on a surface with a high velocity, which causes an indent on the material surface resulting in material removal. Several forces of different origin may act on a particle impacting on a solid surface. However, the dominant force on the erosive particle which is responsible for decelerating it from its initial impact velocity, is usually the contact force exerted by the surface. In erosion, the extent of wear depends on the number and mass of the individual particles striking the surface and on their impact velocity [40].

The erosion wear resistance is assessed by a jet nozzle type erosion equipment. The material loss, due to the impingement of the gas entrained solid particles on the surface of the body, is determined and erosion wear is estimated. The erosion test is standardized by the ASTM G 76-83 test, which utilizes a repeated erosion approach involving a small nozzle delivering a stream of gas containing abrasive particles. The schematic of the suggested process is shown in Fig. 19. The nozzle is of 1.5 mm inner diameter, 50 mm long and manufactured from an erosion resistant material like WC/Co and  $Al_2O_3$ . The nozzle is perpendicular to the specimen surface. The recommended abrasive particles are 50  $\mu m$  diameter angular alumina and should be used only once. The recommended particle velocity is around 30 m/s at the time of impact with the gas flow being maintained at 140 kPa (20 psig). A test time of 10 min is suggested by the

ASTM standards to achieve a steady state condition. The distance between the nozzle and specimen should be maintained at  $10 \pm 1$  mm. The particle feed rate should be maintained at  $2.0 \pm 0.5$  g/min. The erosion is assessed by the mass loss after a constant time of the test.

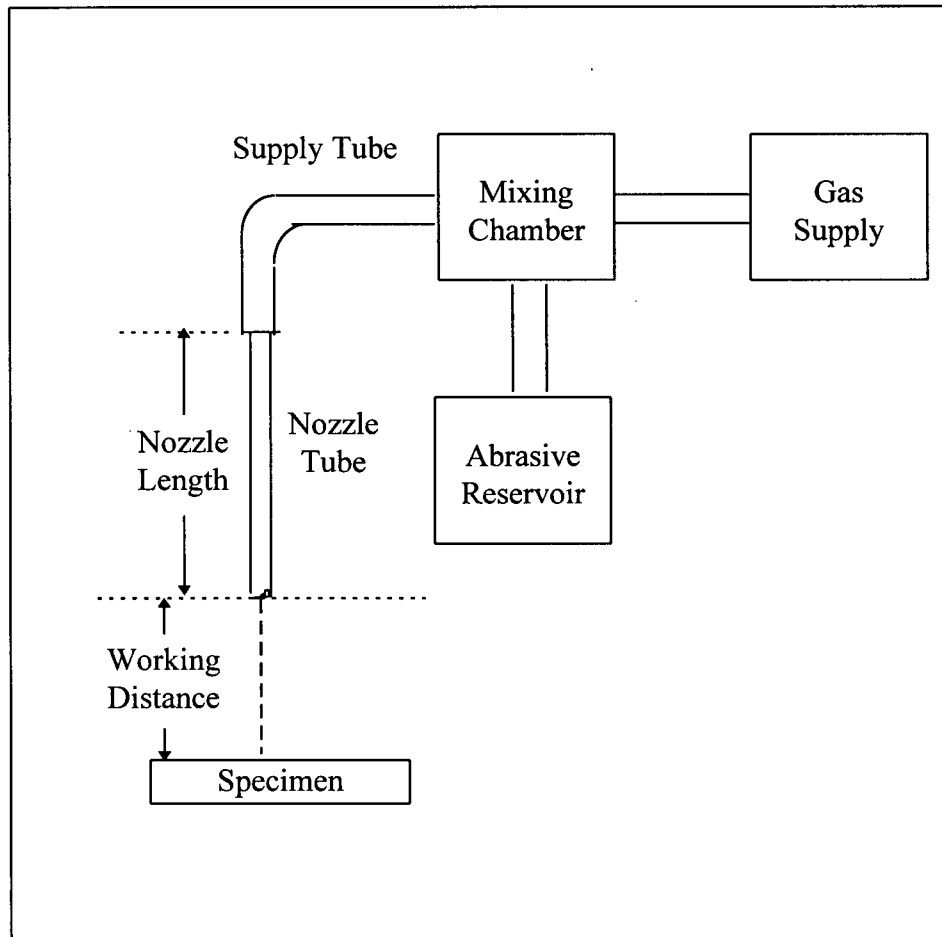


Fig. 19: Schematic drawing of solid particle erosion equipment (ASTM G76-83).

## 2.7 Previous Work on Al-SiC Coatings

Not many studies have been reported on plasma spraying of Al based MMC. Two of the reported results have been cited in the present work. Ilyuschenko et. al [5] reported the deposition of Al based MMC, where the reinforcing phase was SiC or TiC particles.

The volume percentage of the reinforcement was varied from 50 to 75 vol%. The work was limited in the absence of proper characterization of the powder and the coatings that were subsequently produced. Undue emphasis was given on the hardness of the coatings, which, as was proved in the present work, can show extensive variation depending on the microstructural uniformity and size of the second phase. The other reported investigation was conducted by Khor et. al [15] where they plasma sprayed Al-Li (2.54 wt%) based MMC. The reinforcement particles were limited to electronic grade (sub-micron) sized SiC particles. The electronic grade SiC increased the cost of the powder and showed a tendency towards agglomeration. The clustering of the SiC particles was avoided by extensive processing of the powders through plasma spraying which further added to the costs. The coatings that were produced were not characterized for their wear and other physical properties.

### **Chapter 3: Scope and Objective**

Al and its alloys are preferred as structural components due to their high strength to weight ratio. However, they have low wear, erosion and abrasion resistance which limit their use. For, many of the engineering applications where the wear and surface properties are critical than the strength of the component, a wear resistant surface coating on the Al substrates becomes an attractive alternative.

The objective of the present work is to develop a technique for depositing a wear resistant coating which would adhere strongly to the Al based substrates and have thermo-physical properties similar to the substrate. Plasma spraying is one of the most economical techniques for producing coatings on large sized components so it was chosen as the deposition method. To ensure the compatibility of the properties like thermal expansion coefficient, elastic modulus, etc. between the coating and substrate, an Al based MMC was chosen as the coating material.

The present work involved the synthesis of the MMC powders with Al as the matrix and different sized SiC reinforcements. The powders were characterized for their morphological and microstructural properties. The coatings were produced by atmospheric plasma spraying and were then extensively studied for their microstructural homogeneity, density, adhesion, hardness, abrasion, erosion resistance and other physical and chemical properties. Lastly, an attempt was made to optimize some of these properties namely the wear, adhesion and hardness of the coating, based on the SiC content and particle size.

## Chapter 4: Experimental Procedures

### 4.1 Powder Preparation

#### 4.1.1 Starting material

Aluminum alloy 6061 of average particle size 45  $\mu\text{m}$  was mechanically alloyed with SiC particles of 1200 grit (equivalent to the average size  $\approx 8\mu\text{m}$ ), 800 grit ( $\approx 15\mu\text{m}$ ), 600 grit ( $\approx 22\mu\text{m}$ ) and 400grit ( $\approx 37\mu\text{m}$ ). The aluminum particles<sup>1</sup> were spray dried and atomized showing spherical morphology (Fig. 20a), whereas the SiC<sup>2</sup> is fused-crushed and has an angular structure (Fig. 20b). The chemical composition of the Al 6061 alloy is shown in Table 3.

**Table 3.** Elemental composition of the Al 6061 alloy used as the matrix material.

Element	Cr	Cu	Fe	Mg	Si	Zn	Al
% by wt.	0.07	0.23	0.22	0.88	0.96	0.04	Bal.

Pure Al normally does not wet SiC, but the presence of alloying elements like Si, Mg, etc. improves the wettability. Moreover, Al-Mg-Si alloys like Al 6061 can be age hardened which increases the strength of the matrix considerably. These intermetallics make the matrix material considerably stronger than pure Al matrix. Commercially pure Al (Al 1060 - 99.6% Al, Si and Fe impurities) shows a tensile strength of 131 MPa in the

---

<sup>1</sup> Supplied by Valimet Inc., Stockton, CA

<sup>2</sup> Supplied by Norton Company, Saint Gobain, Boston, MA

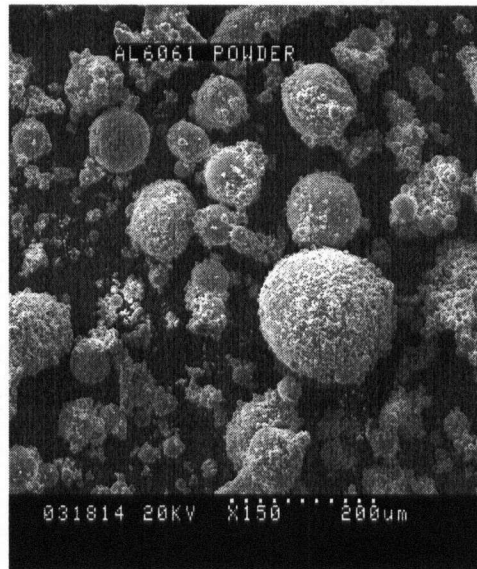


Fig. 20a

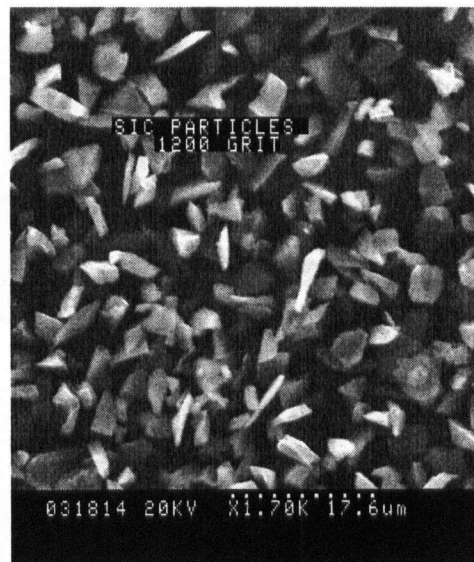


Fig. 20b

Fig. 20: Morphology of starting powders under SEM a) Al 6061 powder b) SiC 1200grit powders.

wrought, strain hardened (ASTM H18) condition and compared to this Al 6061 shows a tensile strength of 310 MPa in the artificially aged (ASTM T6) condition.

#### 4.1.2 Powder preparation

The blending was done in acetone using a rotary ball mill and alumina balls. The actual mechanical alloying was done in alumina ceramic vial sets, 5.7 cm diameter and 7 cm height, using a SPEX<sup>3</sup> Mixer 8000 mill. The mill vibrates in the three mutually perpendicular directions at approximately 1200 rpm (quoted by the supplier). A mixture of SiC balls and stainless steel ASI 52100 bearing balls of 12-16 mm in diameter were used as grinding media. The weight ratio of the powder to balls was kept at 5:1 with 15 g of powder being processed at every load. The time of milling was varied from 5 to 40 minutes. The corresponding changes in particle size were monitored as a function of milling time. Between the millings, the interior of the vials were grit blasted to remove traces of cold welded aluminum.

The composition of the composite powder and SiC size variations were conducted in two stages to minimize the number of experiments. In the first stage, the powder contained 20, 30, 50 and 75 vol% of SiC the balance being Al 6061 alloy. The SiC used for this stage was of 1200 grit ( $\approx 8 \mu\text{m}$ ). The compositions of the powder are coded using volume percentage and grit size of SiC, for example Al-75SiC1200 denotes the composite having 75 vol% SiC of 1200 grit as the reinforcement, the balance being matrix Al 6061. The above four volume percentages of SiC were repeated with the

---

<sup>3</sup> Trademark of Sytech Corporation, Houston, TX

additions of small amounts (< 4 wt%) of an organic process control agent (PCA), which modified the nature of interaction of metallic and nonmetallic surfaces. PCA is added to enhance entrapment of SiC particles within cold welded aluminum. In the second phase of the investigation, the powder composition was kept constant at 50vol%SiC and the SiC particle size was varied using the 1200, 800, 600 and 400 grit sizes. Table 4 gives an overview of the composition and reinforcement sizes of the powders processed in this work.

**Table 4:** Overview of the composition and reinforcement sizes of the processed powders.

Grit Size Vol% SiC	400 (37 μm)	600 (22 μm)	800 (15 μm)	1200 (8 μm)
20	-	-	-	Al-20SiC1200
30	-	-	-	Al-30SiC1200
50	Al-50SiC400	Al-50SiC600	Al-50SiC800	Al-50SiC1200
75	-	-	-	Al-75SiC1200

After mechanical alloying, the powders were sieved and classified. Sizes ranging between +325 mesh (44μm) and -100 mesh (149μm) were used for plasma spraying. The yield of the powders and the distribution of the SiC particles (in the composite powders) were monitored for each of the four compositions and for different amounts of PCA.

### 4.1.3 Powder Analysis

The distribution of the SiC particles in the composite powders was observed by optical and scanning electron microscopy on the cross sections of the mechanically alloyed powder particles, vacuum impregnated in a fluorescent epoxy. The effect of MA and plasma spraying on the morphology of SiC particles was observed. Particle size analysis of the powders was done using the Horiba<sup>4</sup> particle size distribution analyzer and was also calculated by using an SEM.

Compositional analyses of the powders were conducted by using an image analyzer, EDX along with an SEM and also by wet chemical analysis. While using the image analyzer and SEM for the composition analysis it was assumed that the distribution of SiC was identical in the third dimension to that observed in the cross section. The wet analysis was carried out by the method of back titration [41] by which the weight percentage of aluminum in the powder was assessed.

## 4.2 *Coating Experiments and Analysis*

### 4.2.1 Plasma Spray Process

Spraying was done in air using two type of torches, an Axial III<sup>5</sup>, and an Axi-Jet system<sup>6</sup> operating with 82.5 vol% Ar +12.5vol%N<sub>2</sub> +10vol%H<sub>2</sub> plasma. All powders having different compositions were sprayed under the same condition except for Al-75SiC1200. Table 5 summarizes the spraying conditions using the Axial III plasma spray

---

<sup>4</sup> Horiba particle size distribution analyzer, Model: Capa-7000, Horiba Ltd., Kyoto, Japan

<sup>5</sup> Product of Northwest Mettech Corp. of Richmond, BC, Canada.

<sup>6</sup> Product of Metcon Thermal Spray of Abbotsford, BC, Canada

system. The Axi-Jet torch was operated under identical conditions except for some changes in the operating power and gas flow rate due to the differences in the design of the two torches. Coating thickness varied between 120 and 220  $\mu\text{m}$ . However, some  $\approx 6$  mm thick coatings were also produced for the purpose of density measurements and to observe any delamination of the coating due to the accumulation of residual stress. Coatings were mostly sprayed directly on flat plain carbon steel coupons (80 mm  $\times$  37.5 mm  $\times$  10 mm). These were subsequently polished across the cross sections for metallography, measurement of coating density, volume fraction of SiC in the coating and microhardness of the coatings. Polishing was done using SiC polishing papers and pullouts were minimized by using small increments in the grit size of successive polishing papers. Density of the thick coatings was determined by using a helium pycnometer<sup>7</sup>.

**Table 5.** Summary of the plasma spraying conditions using Axial III torch.

<b>Plasma Conditions</b>	<b>Al-20SiC1200 Al-30SiC1200 Al-50SiC1200</b>	<b>Al-75SiC1200</b>
Total gas flow (l/min)	220	220
Plasma gas	Argon	Argon
Nitrogen Content (% of total gas)	7.5	10
Current (A)	180	210
Power (kW)	66	79

<sup>7</sup> Micromeritics Instrument Corp., Model 1302, (Norcross, GA, USA)

#### 4.2.2 Hardness Measurements

Vickers<sup>8</sup> microhardness measurements were carried out on polished cross sections of the coatings on the coupons with a load of 100 g. This load produced indentations of 40 to 50  $\mu\text{m}$  (across diagonal), which resulted in averaging the hardness difference due to microstructural characteristics. Microhardness was also measured by the depth sensing indentation technique using a Fischerscope<sup>9</sup> H-100 model with a load of 30 g which helped in assessing hardness at selective locations in the microscopic level.

#### 4.2.3 Adhesion Measurements

Spraying was also done on mild steel rods of 1" diameter and either 1/2" or 1" long, suitable for the standard ASTM C633 tensile test of adhesion. The longer specimens, although not exactly confirming to the ASTM standard, were preferred to avoid the effects of nonuniform stress distribution [39]. The tests samples were assembled using a 3M structural epoxy (EC 1386) as an adhesive, which has a maximum tensile strength of 120 MPa. A standard Instron machine was used for conducting the tests.

Coatings were also made by spraying on thin Al, Ni, stainless steel and plain carbon steel foils (thickness  $\approx 178 \mu\text{m}$ ) mounted on copper blocks as test samples for the Peel Adhesion Test (PAT) which is a modified version of ASTM D-3167 peel test [39]. The copper blocks, which acted as heat sinks during plasma spraying, were fixed to the

---

<sup>8</sup> Vickers Micrometer 3 microhardness tester (Buehler Ltd., IL, USA)

<sup>9</sup> Fischerscope Nano-indentor, H-100, (FischerTech. Inc., CT, USA)

foils by using common Pb-Sn (50-50) solder or by using a mixture of a silicone sealant<sup>10</sup> and copper powder in the ratio of 1:2 by weight. In the later case, the adhesive was cured for 12 hr at room temperature till an appreciable strength was obtained. The schematic of the sample preparation and the actual tests are shown in Fig. 17.

The oxygen pickup during spraying was assessed from the height of aluminum oxide peak, obtained on the surface of the coating from X-ray diffractometry. The same analysis was also repeated for various levels below the surface of the coatings, by polishing off 50  $\mu\text{m}$  from the top and subjecting it to a similar analysis.

#### 4.2.4 Wear tests

Abrasive wear test was conducted in which samples with  $\approx 1 \text{ cm}^2$  of the coating were mounted in a hard epoxy resin<sup>11</sup> and abraded under a constant load with 400 grit SiC papers as the abrasive medium. For this purpose a Buehler<sup>12</sup> autopolisher, where six samples could be loaded at a time, were used. The uniformity of the SiC papers was maintained by replacing them every 3 minutes. Besides, to maintain the uniformity, chromium oxide coatings were used as one of the samples amongst the six. Chromium oxide has a wear resistance superior to any of the MMC tested and this ensured that the rate of wear of the SiC papers was uniform and regular. The loss due to wear was monitored by measuring the changes in the thickness and weight of all the specimens.

A dry erosion test, modification of the ASTM (G76-83), was conducted where a

---

<sup>10</sup> Dow Corning 732, Scellant RTV manufactured by Dow Corning Canada.

<sup>11</sup> Epofix manufactured by Struers, Copenhagen Denmark

<sup>12</sup> Buehler Autopolisher, Model Ecomet III, Buehler Ltd., Illinois, USA.

comparative erosion wear was obtained by grit blasting the samples at an angle of ninety degrees. A commercial grit blaster<sup>13</sup> was used for the test. The conformity to ASTM standards was maintained by using a constant value of particle velocity of 70 m/s and grit flow rate of 55 g/min. The samples were obtained from the coupons having coatings of 1 cm<sup>2</sup> surface area. The loss of material due to erosion was calculated from the weight loss of the specimens. Bulk samples of Al-20vol%Al<sub>2</sub>O<sub>3</sub> (having the Al<sub>2</sub>O<sub>3</sub> particles of  $\approx$  35  $\mu$ m diameter, matrix of Al alloy 6061) were obtained from ALCAN, Montreal, Canada. The composite was obtained after one step extrusion of cast billets of 185 mm diameter into rods of 51 mm diameter. This composite was also tested to study the different forms of wear and also was used as a reference for the wear behavior of the coatings developed in the present work.

---

<sup>13</sup> Model 3040S Manufactured by Empire Abrasive Equipment Corporation, PA

## Chapter 5: Results and Discussion

### 5.1 Powder Preparation

One of the main problems in manufacturing Al-SiC composite powders is agglomeration of the SiC particles in the Al matrix. Mechanical alloying is one of the better processing routes by which these powders can be produced with a minimum amount of segregation. Amongst the different type of equipment commonly used for MA (Table 2), a SPEX mill offers a higher power compared to a planetary ball mill or the attritor. As a result attritors and the planetary ball mills typically have batch times of 10-12 hr., while the SPEX mill can completely mechanically alloy a batch in less than one hour [27].

#### 5.1.1 Powder Morphology

##### a) Al Particle Size Distribution

Figures 21 to 24 show the gradual change in powder morphology of Al-50SiC1200 as a function of mechanical alloying time, both with and without Process Control Agents (PCA).

The results of 5 minutes of milling are shown in Fig. 21. Figure 21a illustrates the powder morphology when the milling was conducted with PCA, whereas, Fig. 21b shows the powder after 5 min of milling without PCA. The Al particles fractured in presence of PCA (3 wt%) and were reduced from their initial size of 45  $\mu\text{m}$  to less than 8  $\mu\text{m}$ . The powder shows a homogeneous distribution of the Al and SiC particles. There was a reduction in the angular nature of SiC compared to what was seen in the starting material,



Fig. 21a

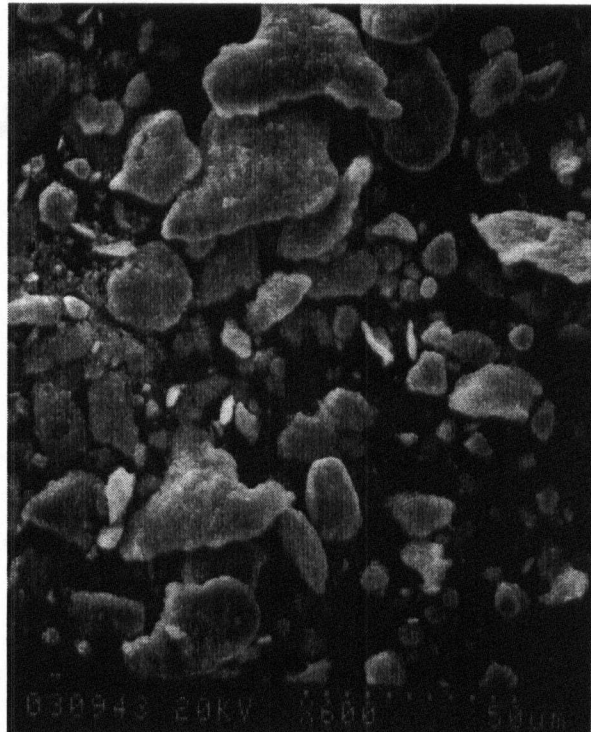


Fig. 21b

- Fig. 21: a) Powder Morphology under SEM after 5 min. of milling with 3wt% PCA.  
b) Powder Morphology under SEM after 5 min. of milling without PCA.

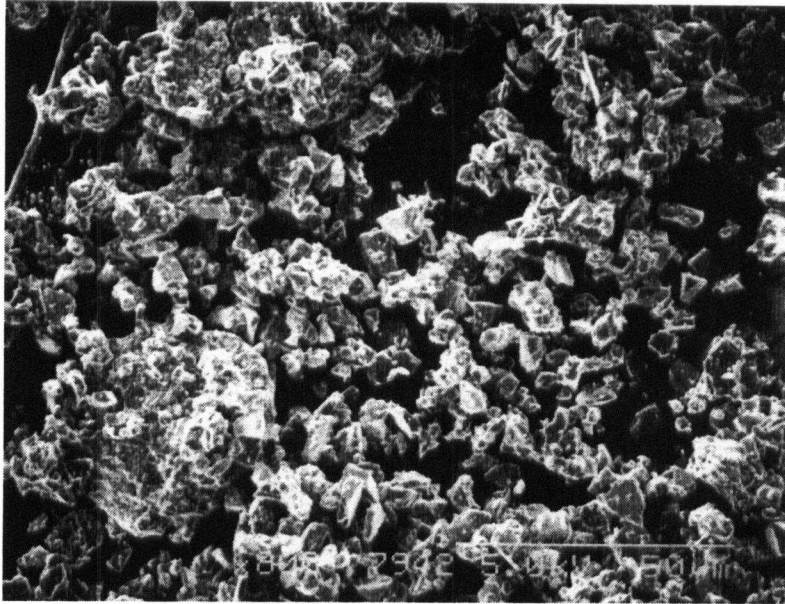


Fig. 22a

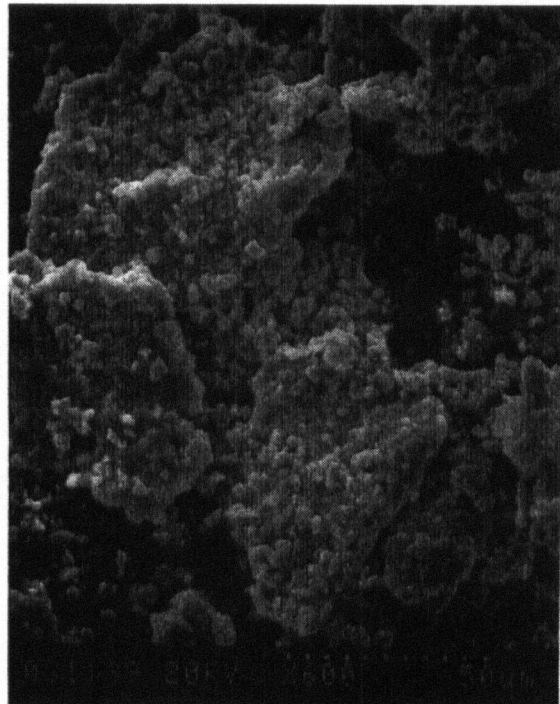


Fig. 22b

- Fig. 22: a) Powder Morphology under SEM after 10 min. of milling with 3wt% PCA.  
b) Powder Morphology under SEM after 10 min. of milling without PCA.

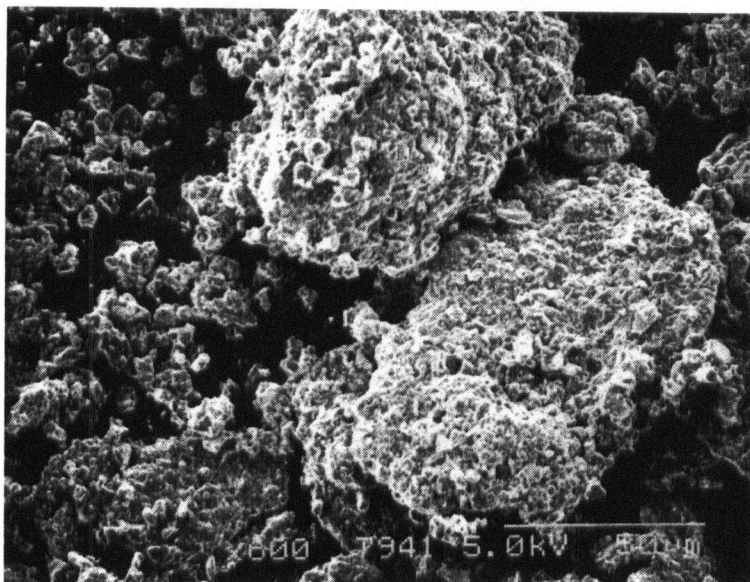


Fig. 23a

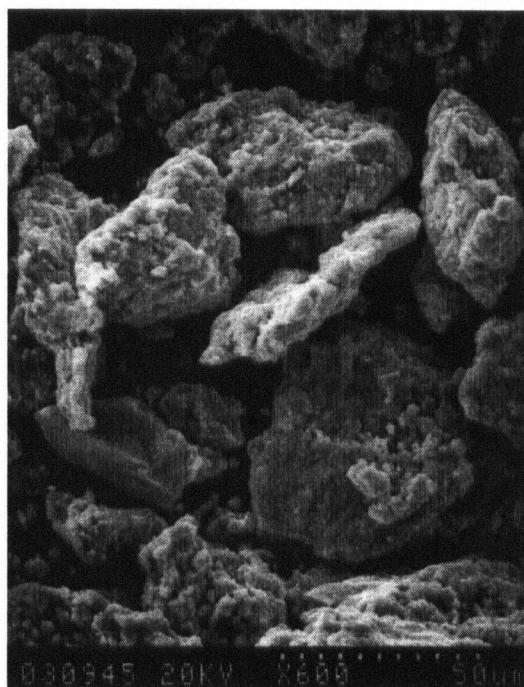


Fig. 23b

- Fig. 23: a) Powder Morphology under SEM after 20 min. of milling with 3wt% PCA.  
b) Powder Morphology under SEM after 20 min. of milling without PCA.

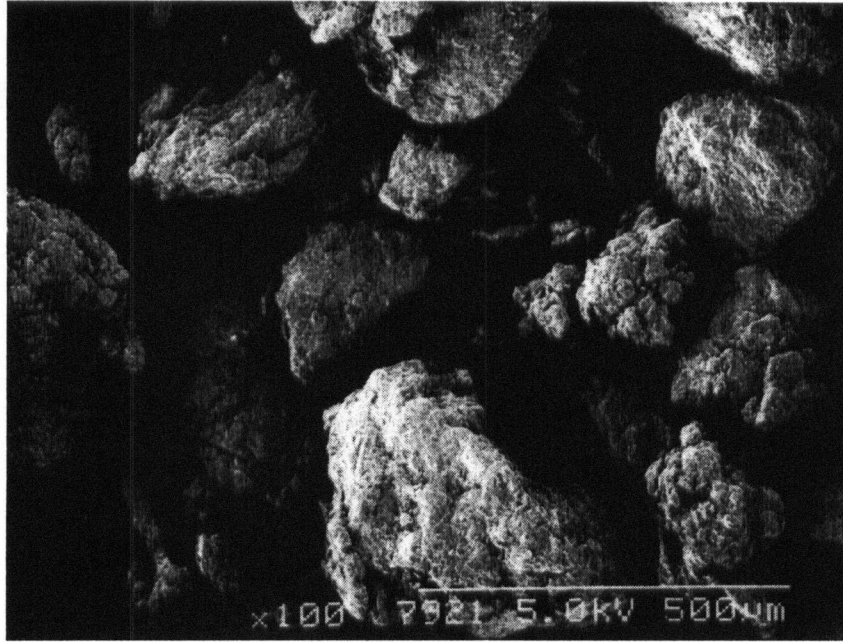


Fig. 24a



Fig. 24b

- Fig. 24: a) Powder Morphology under SEM after 30 min. of milling with 3wt% PCA.  
b) Powder Morphology under SEM after 30 min. of milling without PCA.

(Figure 20b). The morphology of the powder was different in the absence of PCA as can be seen in Fig. 21b. The amount of fracture in the composites was reduced and flattening of the particles was the dominant phenomenon. Hence, the average particle size remained  $>20\ \mu\text{m}$ . The SiC particles are present as fines in the microstructure and were confirmed to be so by conducting a Si mapping using the EDX facility of the SEM.

With increase in time of milling, the Al particles begin to cold weld and thereby increase in size. Figure 22a, where the powder morphology is shown after 10 min. of milling with 3 wt% of PCA, shows a decrease in the amount of fines and formation of agglomerated or cold welded Al particles. As the Al particles cold welded, the SiC was absorbed within the MMC particles and this was confirmed from the amount of free SiC left as fines in the powder mixture. Comparison of the morphology of the powder between Figures 21a and 22a shows that there is an increase in the particle size of the MMC. Thus the process of cold welding was dominant compared to the rate of fracture. The cold welded particles in Figure 22b show a stratified structure for the large Al particles indicating their formation by the cold welding of several particles.

Figure 23a shows the powder morphology after 20 min of milling with PCA. The average MMC particle size is approximately  $80\ \mu\text{m}$  and roughly spherical in shape. The amount of fines and free SiC in the microstructure decreased in comparison to what was seen after 5 and 10 min of milling in Figures 21a and 22a respectively. Figure 23b shows the powder that was milled for 20 min without PCA. The particles increased in size but the flattened structure of the powder was retained. The stratification of the powders was more pronounced than in the previous stage of milling. Although the amount of free SiC

and fines in the microstructure decreased, Si mapping of the powder reveals that most of the SiC phase is present on the surface of the MMC. The fine particulates in Fig. 23b (less than 10  $\mu\text{m}$ ) seen on the surface of the Al particles were revealed to be SiC from the X-ray maps. In contrast, there was not any significant SiC concentration on the surface of the MMC in Fig. 23a.

The final sprayable Al-50SiC1200 composite powders are shown in Fig. 24a, which shows spherical particles between 45 and 200  $\mu\text{m}$ . Most of the fines and SiC present in the intermediate stages of milling, Figures 21a, 22a and 23a was not seen in the final powder after 30 min. of milling with PCA. The final powder without PCA had SiC present on the surface of the MMC particles, as shown in Fig. 24b.

The change in average size of the particles, as measured by the particle size analyzer, with milling time is summarized in Fig. 25, for milling done with and without PCA. When the milling was conducted without PCA the size of the particles increased at a faster rate compared to what was seen when PCA was used. In Figure 25, the size distribution of the particles for milling without PCA has been supplemented by a dotted line for the initial 15 min of milling along with the values obtained from the particle size analysis. The dotted line indicates the particle sizes obtained from the microstructures of the powders under an SEM. The reason for the difference between the two values is due to the morphology (i.e. flake or platelet shape) of the particles observed when the milling was done without PCA. The particle size analyzer determines the particle size assuming spherical shape of the particles. However, the flakes obtained, have a high aspect ratio which may account for the erroneous particle sizes obtained by the particle size analyzer.

Compared to this, the values from the SEM were obtained by calculating the diameter of spheres of equivalent volume of the lamellar particles. The difference in the particle size analysis obtained from the SEM and the particle size analyzer decreased with the milling time and becomes equal after approximately 20 min of milling. With longer milling time, the thickness of the discs also increased. Thus, the high aspect ratio of the discs gradually decreased and the particle size obtained by either of the two methods becomes similar.

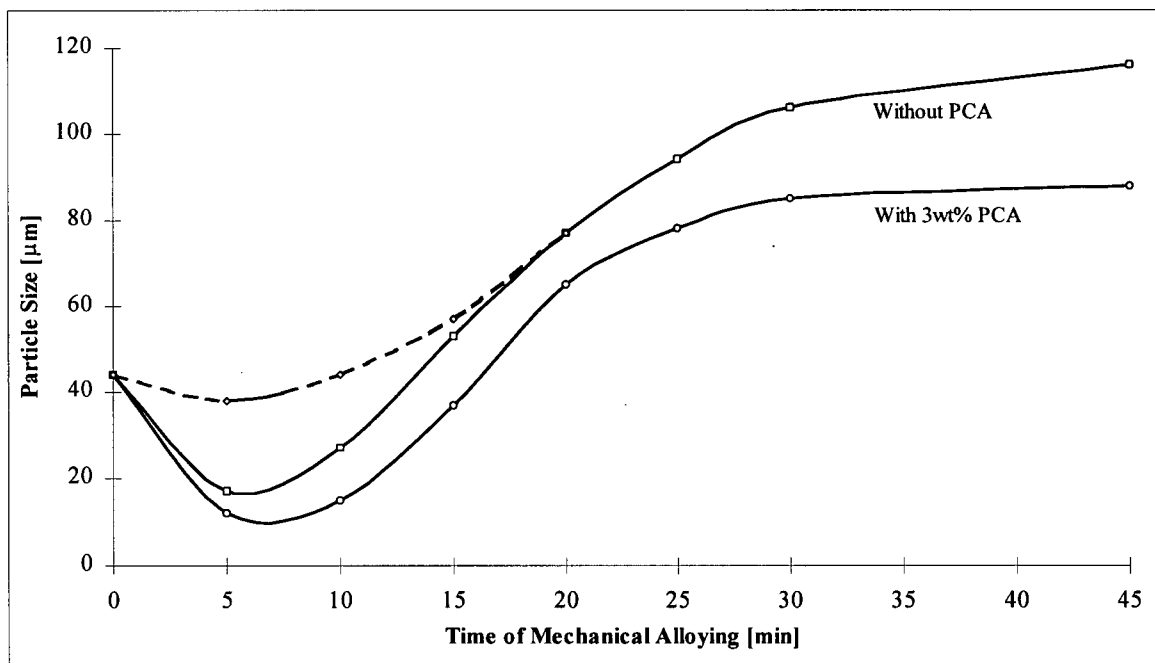


Fig. 25: Change in particle sizes of Al-50SiC1200 without and with 3wt% PCA.

The observed behavior of the Al particles during cold welding can be explained through analysis of the MA process. Mechanical alloying, as observed by Benjamin et. al [18-21] is essentially a combination of fracture and cold welding. Al being a soft ductile metal does not easily mechanically alloy. It is cold welded at a faster rate than the

competing process of fracture. As shown in Figures 21b, 22b, 23b and 24b, in the absence of PCA, the decrease in particle size of the Al powder is minimal and the impact energy of the balls is absorbed in flattening of the cold welded aluminum particles. When PCA is added during the process of MA, it acts as a barrier to the process of cold welding. The mechanism of action of the PCA is still disputed, however, it is believed that PCA acts as a surfactant decreasing the surface free energy of the metal. This reduces the wettability of the surface and prevents atomic diffusion between the two atomically clean surfaces in contact thereby preventing cold welding [18,20,29]. Hence, after the initial 5 min of milling fractured Al particles can be seen.

The ductile fracture in the Al particles can take place in an identical fashion as shown in Fig. 13. Mechanical alloying is characterized by the high strain and high strain rate on the powder resulting from the collision of the balls. The stress state developing in each of the Al particles from the collisions is given by Eq. 2. Besides, friction force at the contact surface generates a tensile stress perpendicular to the impact direction. The presence of PCA reduces the rate of cold welding and the resultant shear stress in the individual particles causes the ductile fracture. In the absence of PCA, the high rate of cold welding allows the particles to combine and form larger ones which prevents the occurrence of fracture.

Fracture of the particles releases the accumulated strain energy and exposes fresh surface areas. With progress in milling, the PCA is entrapped within the Al particles and the free PCA is exhausted. Thus, as the mechanical alloying proceeds the particles start cold welding and agglomerating and the particle size increases with milling time. Hence, as shown in Fig. 25, it can be ensured that when the milling was done with 3wt% PCA,

after an initial decrease in the size of the MMC, the particles increase in size. On attaining a certain size ( $\approx 85 \mu\text{m}$  for Al-50SiC1200 powder with 3wt% PCA) which depends on the composition of the powder, a state of equilibrium is reached between the rate of fracture and cold welding. In Figure 25, this state is attained after 30 min. of milling and particle size remains constant (within 5% of the average size  $\approx 85 \mu\text{m}$ ). In contrast to the above observation, in the absence of PCA, the powders tend to increase in size even after 45 min. of milling. Thus, the PCA was responsible for attaining the equilibrium size. The equilibrium size of the MMC particles was also found to be a direct function of the content of PCA, as can be seen in Fig. 26. Al-30SiC1200 powders were milled with different content of PCA for 45 min and the average particle sizes of the milled powders were obtained. In Figure 26, it can be seen that with the increase in the PCA content the equilibrium particle size decreases. In the absence of Process Control Agents, as seen in Fig. 25, the particles do not achieve an equilibrium size, whereas with the PCA content of 10 wt% powders reached an equilibrium with an average particle size of  $< 50 \mu\text{m}$ .

#### b) Effect of Mechanical Alloying on SiC particle Size

The changes seen in SiC particles during MA can be broadly classified into two categories: 1) changes in size of the particles and 2) changes in morphology of the SiC reinforcements. The effect of MA on SiC particle size depended on the original size of the reinforcement particles used in the composites. The SiC particles of 1200 grit did not undergo any visible change in size during milling. This was confirmed by observing the

particle sizes of SiC obtained in the Al-30SiC1200 and Al-50SiC1200 composite powders, (shown later in Figure 31). However, the 400 grit ( $\approx 37 \mu\text{m}$ ) and 600 grit ( $\approx 22 \mu\text{m}$ ) SiC showed a reduction in size. The fine particles produced by fracture of the reinforcements were entrapped in the coatings, can be seen in Figure 36.

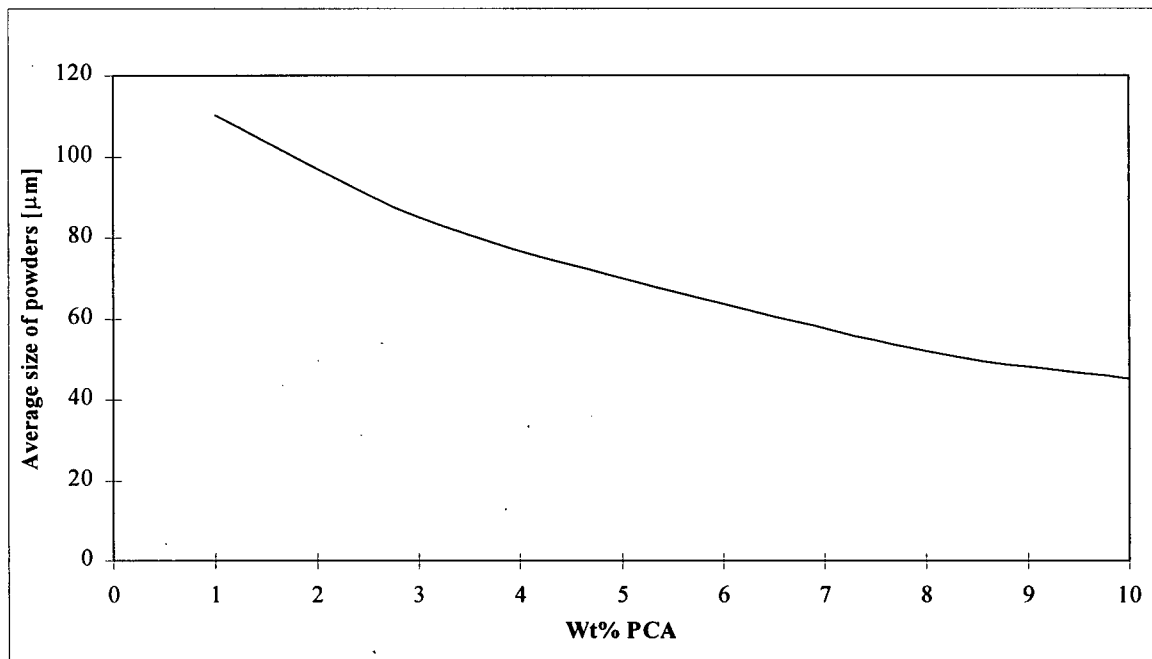


Fig. 26: Change in the equilibrium particle size for the Al-30SiC1200 composites after 45 min of milling with increase in the PCA content during milling.

The change in morphology of SiC particles was similar in all the four grits used. The angularity of the SiC reinforcement particles was reduced. The change in the angularity of SiC particles can be observed by comparing the morphology of the starting powder as shown in Figure 20b with the morphology of the second phase obtained in the composite powders, Figure 31. The SiC in the composite powders after mechanical

alloying showed smoother shapes compared to the sharp, straight edges seen in the starting material.

The reduction in the particle size only for the larger sized SiC particles can be attributed to the presence of inherent flaws. As a result, the strength of the brittle materials is inversely proportional to their volume: [55]:

$$\sigma_1/\sigma_2 = (V_1/V_2)^{1/M} \quad (6)$$

where,  $\sigma_1$  and  $\sigma_2$  are the strength of the brittle SiC particles of different sizes.

$V_1$  and  $V_2$  are the respective volumes of the particles.

$M$  is the Weibull's modulus and varies between 5 and 20 depending on the material.

The smaller the size of the SiC particle, the lower is the probability of finding a critical flaw which can cause a brittle fracture. The larger SiC particles have a higher number of inherent flaws and therefore fracture at lower stress during milling.

The estimation of the kinetic energy required to reduce the SiC particles to submicron sizes also helps in explaining their observed behavior during milling. The kinetic energy required for milling SiC can be estimated from the following equation [56]:

$$U_T = A_C \left[ \frac{1}{a^m} - \frac{1}{a_o^m} \right] \quad (7)$$

where,  $U_T$  = Total kinetic energy in producing a unit amount of powder, [kW]

$A_C$  = Efficiency constant for a particular milling system, [kW( $\mu\text{m}$ )<sup>m</sup>]

$m$  = Fracture constant for a particular material,

$a_o$  = Initial diameter of the particle, [ $\mu\text{m}$ ]

$a$  = Final diameter after milling, [ $\mu\text{m}$ ]

The constant  $m$  depends on the particle size, porosity and mode of fracture and has a value of 1.3 for dense sintered silicon carbide [56]. The value of  $A_c$  is lower for a vibratory type SPEX mill ( $520 \text{ kW}(\mu\text{m})^m$ ) compared to that of an attritor ( $A_c = 2680$ ) or a ball mill ( $A_c = 3350$ ), indicating that the specific energy consumption is less for the SPEX mill [56]. The input energy ( $U_T$ ) required for reducing the SiC particle size to different fraction of their original size are shown in Fig. 27.

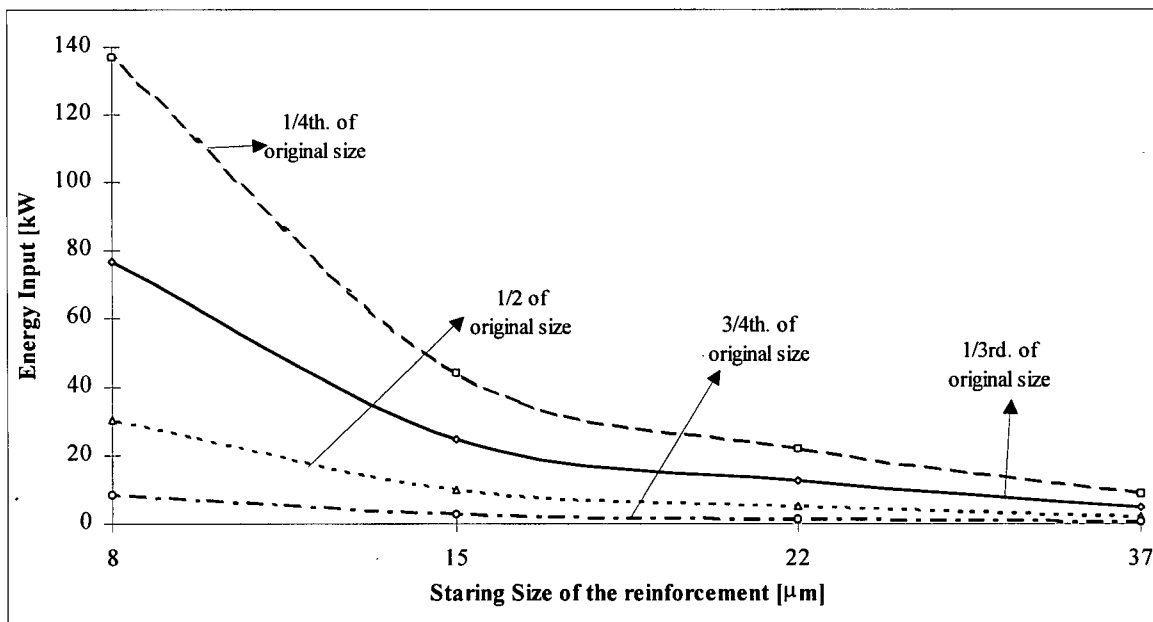


Fig. 27: The energy required to reduce  $1 \text{ m}^3$  of SiC powder from their starting sizes to the different fraction of their respective original sizes. The lines indicate the energy requirement for milling to the same fraction of the original size.

The energy required for fracture provides an explanation for the observed decrease in the particle size of the higher grit SiC during the process of mechanical

alloying. According to Figure 27, reduction of a particle to one fourth of its original size required the highest energy. This value is as low as  $8.7 \text{ kW/m}^3$  for the 400 grit ( $37 \mu\text{m}$ ) or as high as  $137 \text{ kW/m}^3$  for the 1200 grit ( $8 \mu\text{m}$ ) reinforcements. The energy requirements for reducing the  $37 \mu\text{m}$  and  $8 \mu\text{m}$  particles to three quarters of their original sizes differ by a factor of 17. Thus, from the above observations we can conclude that the energy requirement for the size reduction of the smaller sized SiC is much higher thereby showing very little changes in their dimensions.

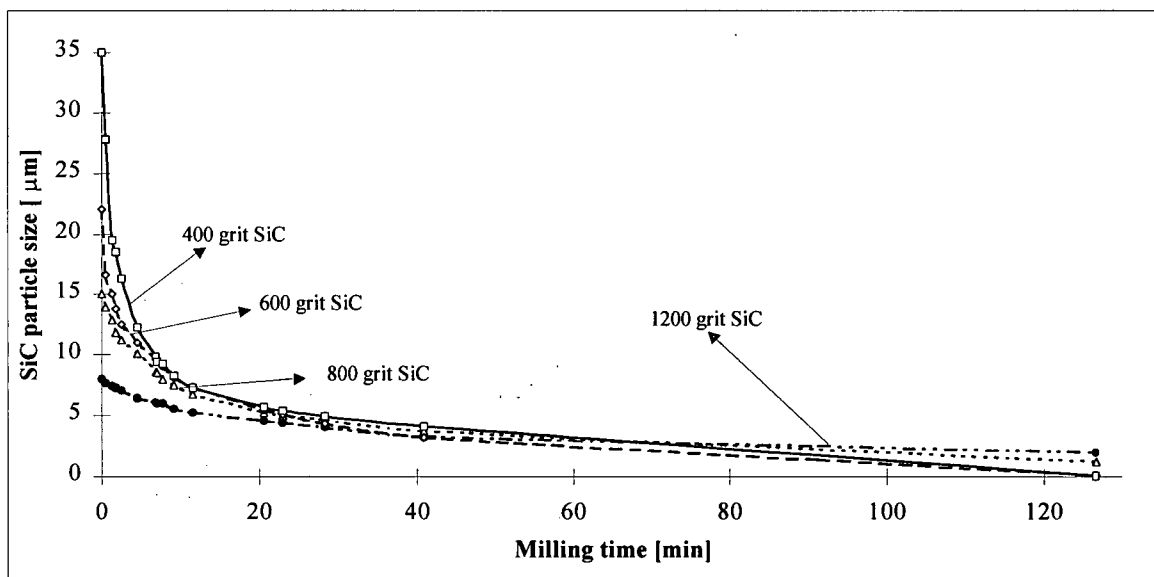


Fig. 28: Change in particle size with milling time for the four different SiC reinforcement sizes: a) 1200 grit ( $8\mu\text{m}$ ) b) 800 grit ( $15\mu\text{m}$ ) c) 600 grit ( $22\mu\text{m}$ ) d) 400 grit ( $37\mu\text{m}$ ).

The rate of reduction of the SiC particles during SPEX milling can be obtained using the value of the power delivered in a SPEX mill, as shown in Table 2. The time to attain the energy values in Fig. 27 can thus be obtained and the change in the particle size with the milling time is calculated in Fig. 28. The size change is a function of the

original particle size. The larger volume of each particle in the 400 (37  $\mu\text{m}$ ) and 600 (22  $\mu\text{m}$ ) grit reinforcements contained larger number of critical flaws and hence had a low fracture strength. However, a rapid reduction of the particle size occurs only in the initial stages (approximately up to 20 min of milling).

Figure 28 predicts a gradual but definite reduction in the particle size of the 1200 grit (8  $\mu\text{m}$ ) reinforcements after 30 min of milling. In contrast to this, the SiC in the mechanically alloyed powders with 1200 grit reinforcements do not show any significant change in their sizes, Figure 31. It is concluded therefore that during mechanical alloying, ductile Al absorbs a significant amount of the impact energy and does not allow SiC particles to fracture.

It is observed that the absence of PCA increases the rate of cold welding which results in larger sizes of Al particles, Figure 24b. The larger Al particles absorb most of the impact energy of the collision process thereby not allowing fracture of the second phase particles.

c) Yield of MMC powder

The yield of the composite powders from MA was assessed by the weight percentage of the MMC obtained between 44  $\mu\text{m}$  and 149  $\mu\text{m}$ , which represented the size range used for spraying, Figures 29 a, b. The yield of the powders depended on the reinforcement size (i.e. SiC particle size) and content: 1) yield decreased with increasing volume percentage of SiC and 2) yield decreased with increasing reinforcement particle

size. The yield also increased with the amount of PCA in the powder and was maximum at 3 wt% for most of the powders.

A higher SiC content corresponds to a lower volume percentage of the matrix material and hence a higher packing density is required to entrap the reinforcing phase. Thus, the entrapment of the reinforcement into Al is more difficult for composites having a high volume percentage ( $\approx 75\%$ ) of second phase. The low volume (i.e. 25%) of the matrix material in the Al-75SiC1200 was primarily responsible for the low yield.

A similar reasoning can be applied in explaining the trend seen with changes in SiC size for the Al-50SiC powders, Figure 29b. The finer sized SiC particles are entrapped easier within the Al matrix. As the average diameter of the MMC particle size ( $85\ \mu\text{m}$ ) that were used for spraying is much larger than the 1200 grit SiC ( $\approx 8\ \mu\text{m}$ ), it is believed that this makes the entrapment of the finer SiC easier. Compared to this, the size of the 400 grit SiC particles is  $37\ \mu\text{m}$  and each reinforcement particle can occupy as much as 10 vol% of the average sized MMC particle. As shown in Fig. 30, the yield of the milling process increases with the ratio of the particle size of the MMC and the second phase. Thus, attaining the same composition with a larger reinforcement size is difficult and the yield decreases.

The addition of PCA increases the yield of the powders (size fraction 44-149  $\mu\text{m}$ ) for all the powder compositions investigated in the present work. The improvement in yield of the process with the use of PCA could arise from two reasons. The fracture of Al particles in presence of PCA allows easier entrapment of SiC in Al as the cold welding

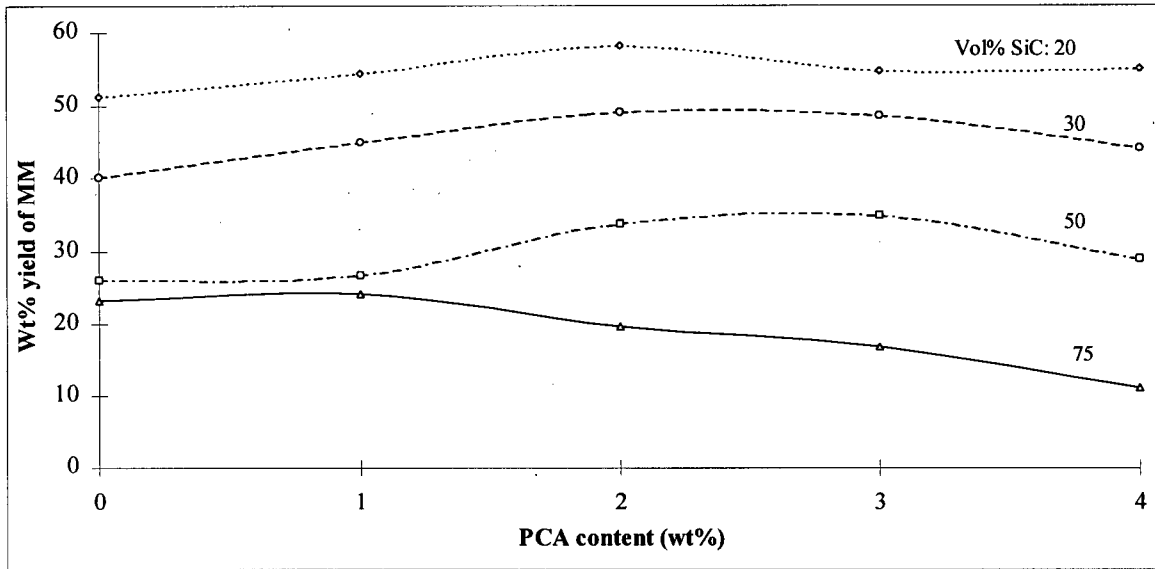


Fig. 29a: Variation in yield (wt% of powder obtained between 325 mesh (44 μm) and 100 mesh (149 μm)) with changes in PCA and SiC content.

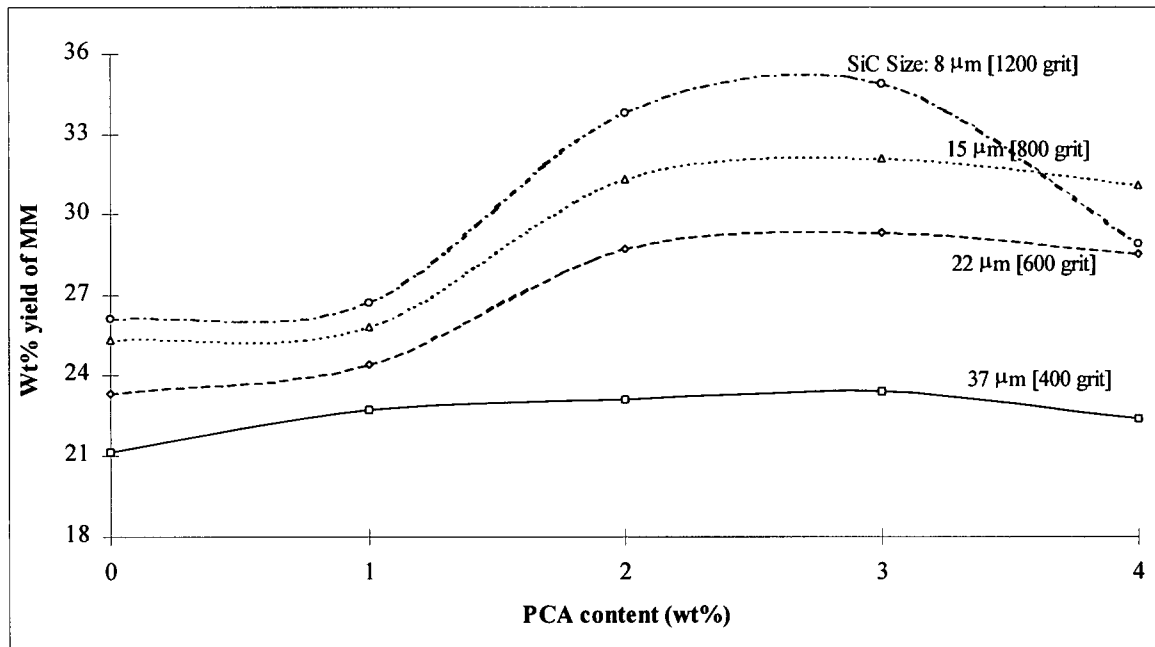


Fig. 29b: Variation in yield (wt% of powder obtained between 325 mesh (44 μm) and 100 mesh (149 μm)) with changes in PCA and SiC particle sizes for Al-50vol% SiC.

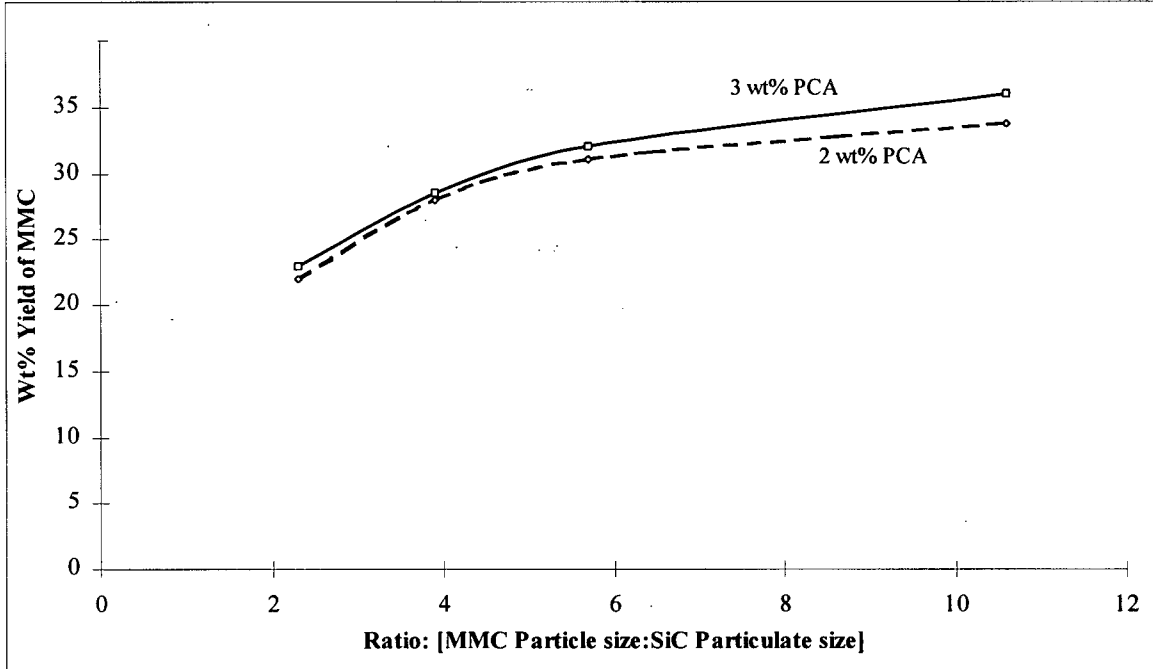


Fig. 30: Variation of the yield of Al-50SiC1200 as a function of the ratio of MMC particle size to the SiC reinforcement particulate size.

starts. The larger sized SiC particles, i.e. the 400 and 600 grits (37  $\mu\text{m}$  and 22  $\mu\text{m}$ , respectively), also show a reduction in their sizes during milling due to the use of PCA. This allows an easier introduction of the reinforcement particles into the Al matrix as shown in Fig. 30. However, higher amounts of PCA ( $\geq 4\text{wt}\%$ ) reduces the yield as it produces a higher weight percentage of fines ( $< 44 \mu\text{m}$ ) due to excessive fracture of the Al and a low rate of cold welding. This reduction in the yield due to excess PCA content was best observed for the composites with finer SiC, i.e. Al-30SiC1200 and Al-50SiC1200 MMC powders.

### 5.1.2 Powder microstructure

Scanning Electron Microscope (SEM) and optical photomicrographs of the powders impregnated in a fluorescent epoxy are shown in Figures 31(a,b,c) for three compositions of the powder: Al-30SiC1200, Al-50SiC1200 and Al-50SiC800. They show a uniform distribution of SiC in the aluminum alloy matrix. The uniformity of SiC distribution in the matrix was confirmed using back scattered X-ray mapping of Si in an SEM along with an EDX. Figure 31d shows the Si mapping of the microstructure of the MMC powder particle shown in Fig.31c. The estimation of porosity from the microstructure was difficult due to the presence of pullouts introduced during the final stage of polishing. Therefore, it is believed that the polished cross sections do not indicate the true SiC content in the MMC particle.

Compared to the microstructures in Fig. 31, the Al-75SiC1200 powder, Figure 32, did not show the circular cross section and had a lamellar flattened structure. The SiC phase showed clustering and was concentrated at the peripheries of the cross sections i.e. at the surface of the powder particles. The higher volume fraction of the reinforcement and the low volume fraction of the matrix material resulted in most of the impact being absorbed by the SiC particles and hence, the Al alloy was flattened and deformed rather than being fractured.

Comparing the microstructures in Figs. 31 and 33, it was seen that for the same time of milling, the distribution of SiC was more homogeneous with PCA than without PCA. It is believed that the fracture of Al in the initial stage of milling with PCA allowed a more homogeneous distribution of SiC within the Al matrix, than that could be

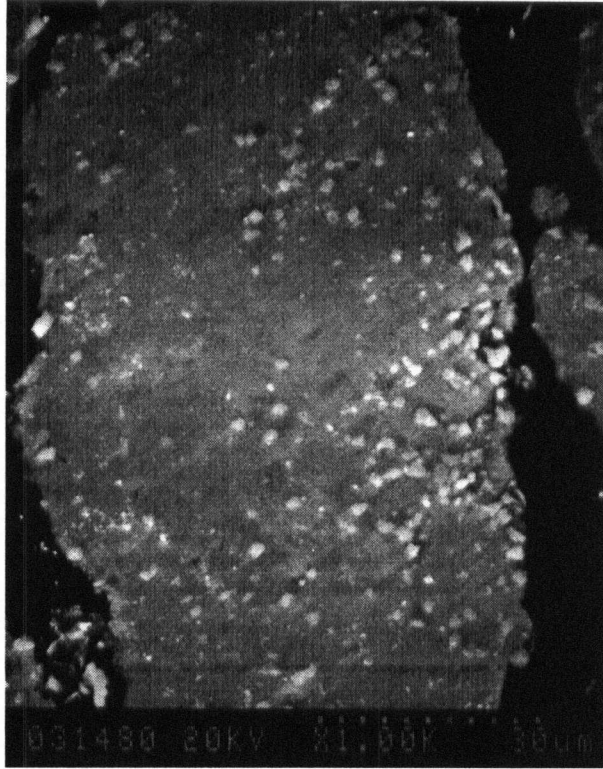


Fig. 31a

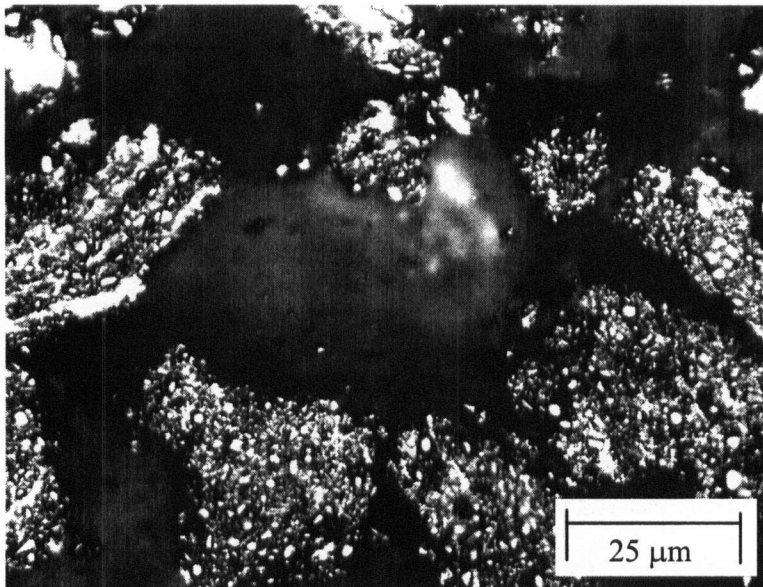


Fig. 31b



Fig. 31c

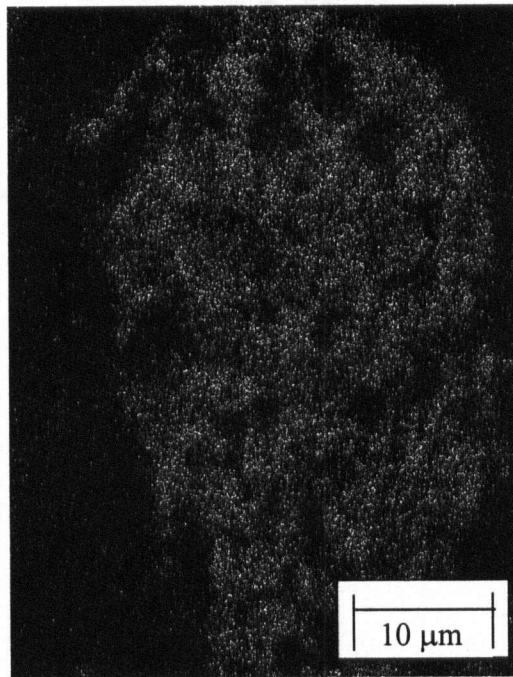


Fig. 31d

Fig. 31: Cross section of the mechanically alloyed MMC powders impregnated in epoxy.  
a) Al-30SiC1200 powder particle (SEM). b) Al-50SiC1200 powder particle (OM). c) Al-50SiC800 powder particle (SEM). d) Si mapping Al-50SiC800 powder of Fig. 31c.

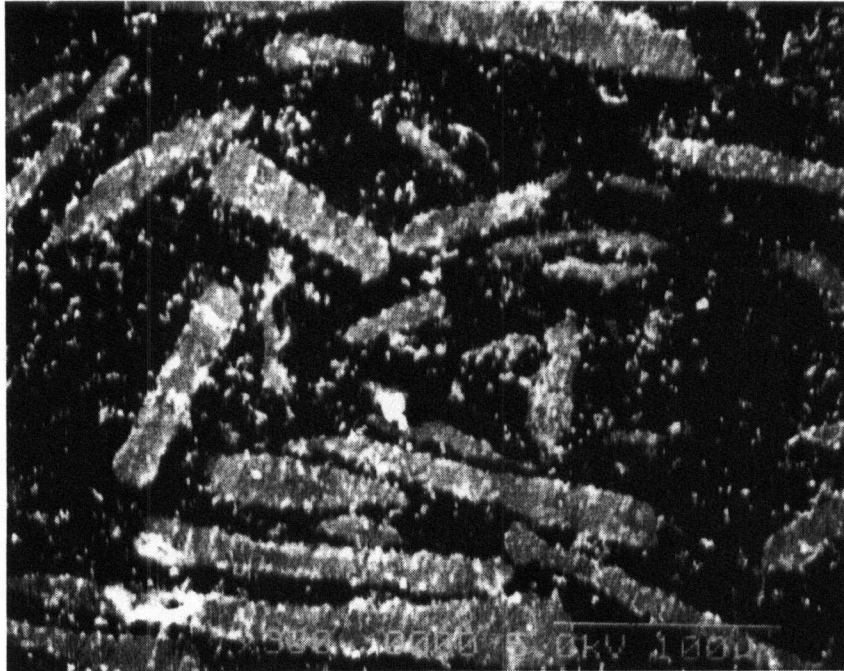


Fig. 32

Fig. 32: Cross section of Al-75SiC1200 powders after 45 min. of milling with 3wt% PCA under optical microscope.



Fig. 33

Fig. 33: Al-50SiC1200 powders when milled without PCA showing a lamellar structure as seen under SEM.

achieved by the plastically deformed Al particles. In the absence of PCA, the SiC reinforcements were concentrated near the surface of the MMC powder. The high concentration of SiC near the surface of the powder results in low entrapment rate of the reinforcements and hence, for the same time of milling, the actual SiC content was less without PCA than it was with PCA. For example, when Al-50SiC1200 powder was milled for 30 min. with and without PCA the SiC content with MMC particles were 46.5 vol% and 41.1 vol%, respectively.

### 5.1.3 Powder Composition Analyses

The accuracy of powder composition analysis by the EDX and image analyzer depended on the microstructural quality of the cross section of the powders. The pullouts of SiC during polishing can drastically affect these results. Moreover, the composition analysis by image analyzer relied on the difference in the brightness of the second phase SiC and the Al matrix. Thus, the reinforcement content obtained through the image analyzer was lower than the actual values as can be seen in Table 6. The compositions obtained by the wet chemical method were not affected by the quality of the microstructure of a particular powder particle. This method assessed the aggregate composition of a larger quantity (5 to 10 g) of powder. The second phase contents obtained for the composite powders, in their sprayed particle size range (44 - 149  $\mu\text{m}$ ), is summarized in Table 6. The SiC content in the composite powder was lower in the samples milled without PCA. As discussed above, the reduction in the rate of fracture

and the resulting microstructural inhomogeneity are the plausible explanations for this observation.

**Table 6:** Compositional analysis obtained from the wet chemical method and image analysis

Powder Composition and Milling Time	Volume percentage SiC obtained from image analyzer for samples with PCA	Volume percentage of SiC obtained from wet analysis for samples with PCA	Volume percentage of SiC obtained from wet analysis for samples without PCA
Al-20SiC1200 milled for 20 min	13.2	19.1	16.2
Al-30SiC1200 milled for 30 min	22.1	28.3	25.1
Al-50SiC1200 milled for 30 min	38.2	46.5	41.1
Al-75SiC1200 milled for 45 min	54.6	67.7	57.2
Al-50SiC800 milled for 30 min	37.2	46.1	ND
Al-50SiC600 milled for 45 min	36.1	45.2	ND
Al-50SiC400 milled for 45 min	31.1	43.9	ND

The large particle size of the reinforcing phase with 400 grit SiC (37  $\mu\text{m}$ ) has particle volume comparable to the average MMC particle size and thus entrapment of the second phase into the Al matrix is more complicated. This reduces the efficiency of entrapment of second phase particles within the matrix with increase in SiC size or volume percentage.

#### 5.1.4 X-ray Diffractometry

X-ray Diffractometry offers one of the easier methods to analyze the entrapment of SiC within the Al matrix without requiring a microstructural inspection of the

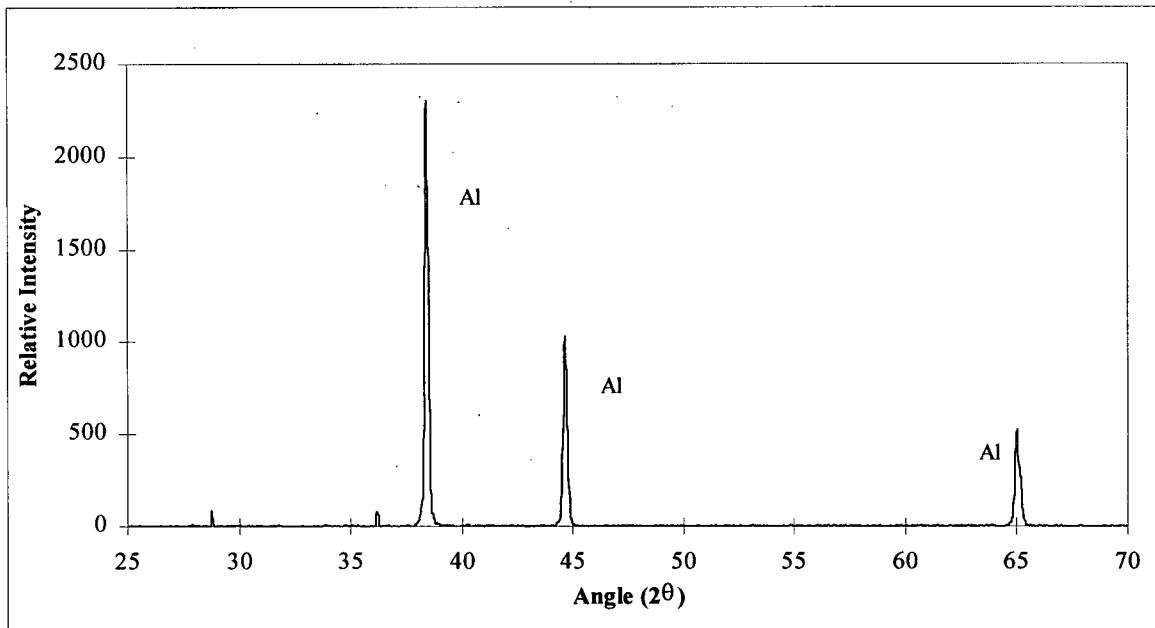


Fig. 34 a: X-ray diffraction pattern of the starting Al 6061 alloy.

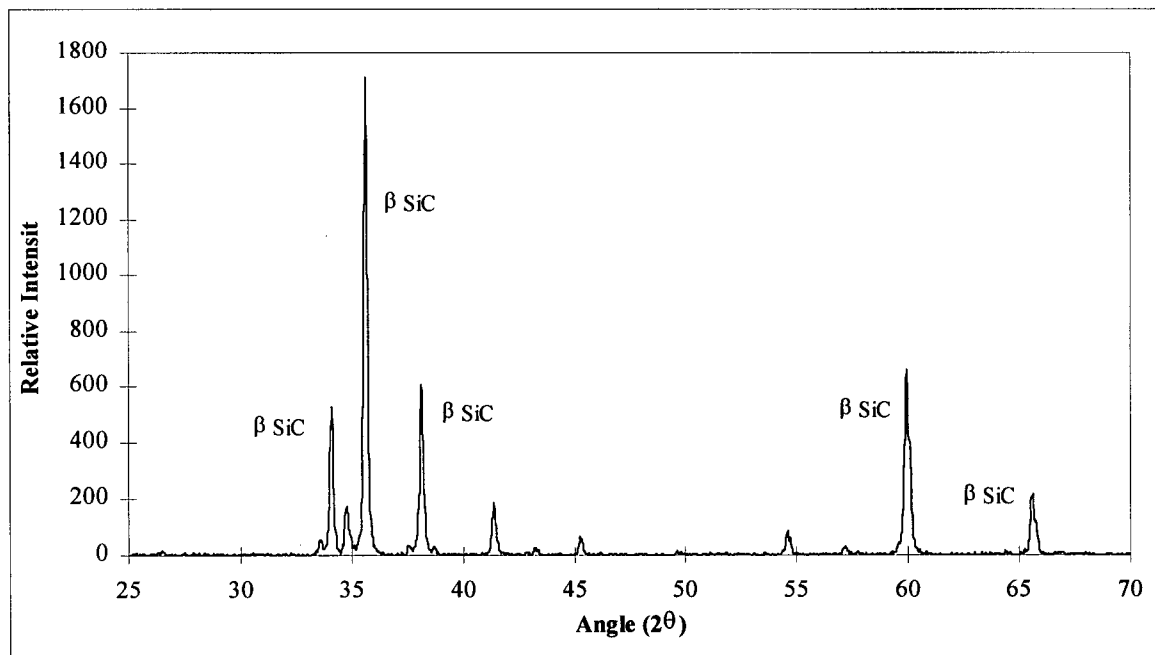


Fig. 34 b: X-ray diffraction pattern of the 1200 grit (8 μm) SiC powder.

powders. Figures 34 (a and b), show the XRD diffractograms of the starting 6061 Al alloy and 1200 grit SiC, respectively. The X-ray for the Al alloy prominently shows the peaks of Al. Figure 34b shows that  $\beta$ -SiC is the major constituent of the SiC phase and the lesser peaks were found to be polymorphs of SiC (e.g.  $\alpha$ -SiC). The main peak for  $\beta$ -SiC lies at  $35.45^\circ$  on the X-ray diffractogram, whereas, the prime peak for Al (111 plane) is at  $37.5^\circ$  on the respective X-ray diffractogram. Figures 35(a-e) show the X-ray diffractograms for the Al-50SiC1200 composition, as a function of milling time. The ratio of the peak intensity for the primary peaks of Al and SiC were found to decrease with increase in milling time, (Figures 35 b-e), compared to the intensities seen in the

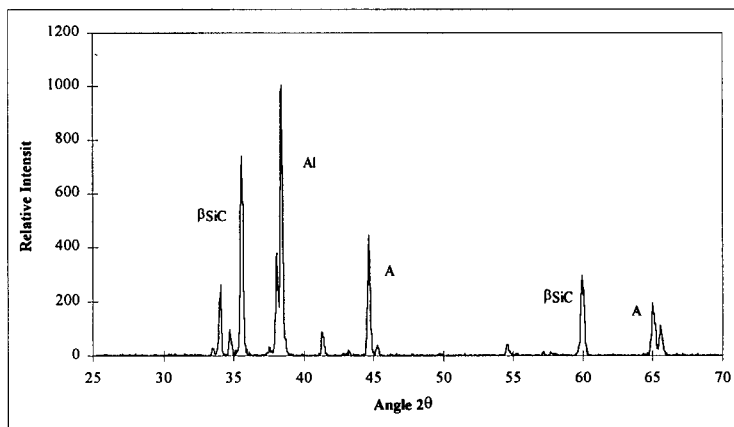


Fig. 35 a.

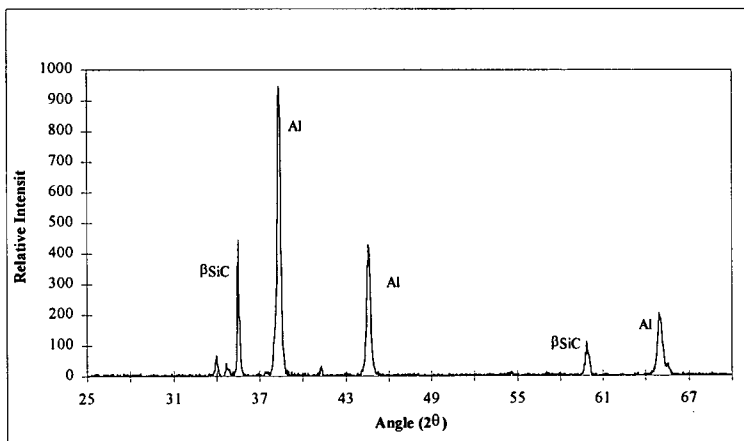


Fig. 35b.

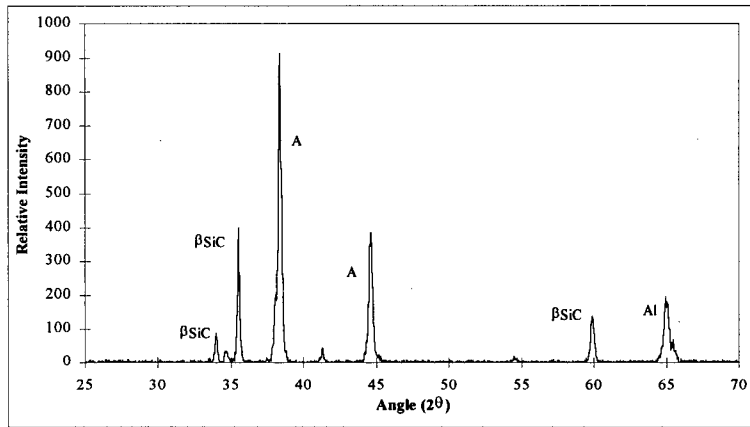


Fig. 35c

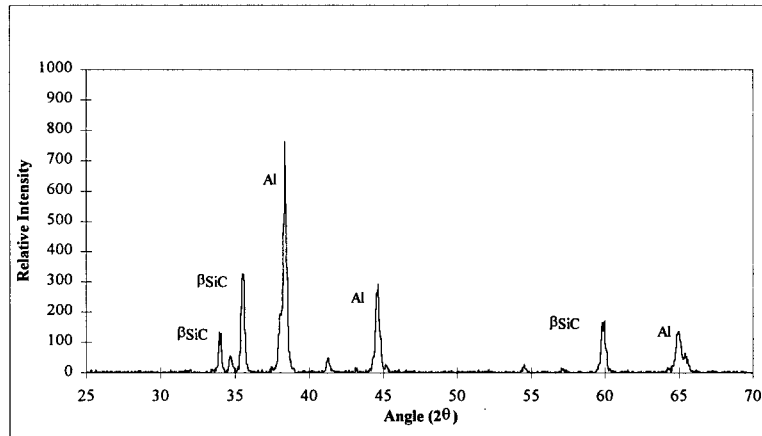


Fig. 35d

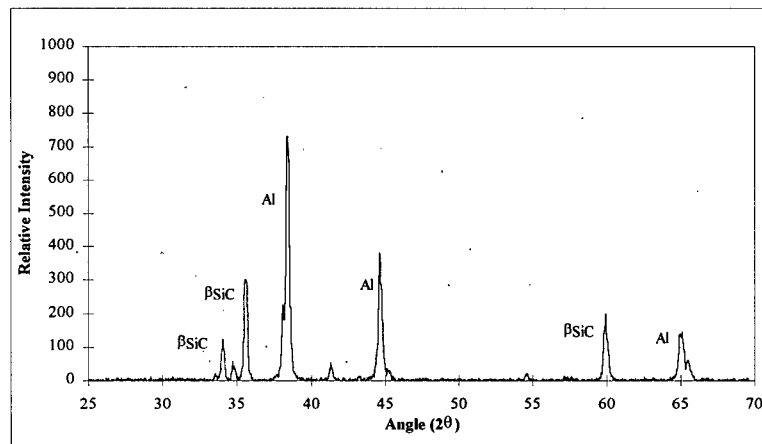


Fig. 35e

Fig. 35: X-ray patterns of the powders with progress in mechanical alloying time a) MA time = 0 min. b) MA time = 5 min. c) MA time = 10 min. d) MA time = 20 min. e) MA time = 30 min.

blended mixture, (Figure 35a). This indicates entrapment of SiC within the Al matrix. The penetrability of the X-ray is of the order of 70  $\mu\text{m}$  for Al [56] which is approximately equal the average size of the MMC particle (85  $\mu\text{m}$ ). The SiC entrapped in the Al matrix is expected to show a lower intensity due to the attenuation of the incident and diffracted rays from the SiC in the matrix Al. Thus with the decrease in the amount of free SiC particles, the height of the SiC peak reduces. Similar observations were reported by Lu et. al [20] where they reported a decrease in the intensity of the peaks of the alloying elements while mechanically alloying with matrix Al.

## **5.2 Coating Deposition**

Coatings were deposited under the conditions listed in Table 5. Along with nitrogen and argon,  $\text{H}_2$  was used as plasma gas to improve the enthalpy of the gas. The enthalpy of the gas was around 7.8 kJ/l. The substrates were cooled by using compressed air injected parallel to the plasma plume axis. Additionally a air knife was also used which produced a lamellar flow of air across the flame adjacent to the substrate surface. The use of the air knife reduces the amount of hot plasma gas reaching the substrate and coating surface, thereby reducing the residual stresses developed during spraying.

Coatings with thickness varying between 200 and 250  $\mu\text{m}$  were sprayed. The samples to be sprayed were mounted on a turntable, rotating at 300 rpm about a vertical axis. The torch was moved in a vertically across the height of the substrates. The combination of the two movements produced a raster scanning across the substrate

surface and resulted in a uniform thickness coating. The substrates that were sprayed have are described in Table 7.

**Table 7:** Summary of the different type of sprayed substrates.

<b>Substrate</b>	<b>Material</b>	<b>Geometry</b>	<b>Uses</b>
Coupons	Mild Steel	(80mm×37.5mm×10mm)	Metallography, hardness, density, wear resistance
Foils	Al, Ni, Stainless steel, plain carbon steel	150 -180 μm thick	Peel Adhesion Test
Rods	Mild steel, Al	1" diameter, ½" or 1" in length	Tensile Adhesion Test

### **5.3 Coating Characteristics**

#### **5.3.1 Coating microstructure**

Figure 36 shows the SEM micrographs of the Al-30SiC1200 and Al-50SiC1200 coatings. The coatings show a dense and clean microstructure with some isolated pores. The porosity of the coatings was less than 2 vol% as determined by helium pycnometry. The isolated pores (darkened areas in the microstructures) result from SiC pullouts during polishing. No unmelt particle of Al 6061 alloy was encountered in the microstructure. This was expected as the alloy had a low melting point of 652°C [52]. The coatings show some oxide contamination and this was confirmed by the X-ray diffraction of the coatings as shown in Fig. 37. It is believed that the expected oxidized products of the composites are alumina (Al<sub>2</sub>O<sub>3</sub>) and silica (SiO<sub>2</sub>) from oxidation of Al and SiC, respectively. Thus, the height of the Al<sub>2</sub>O<sub>3</sub> and SiO<sub>2</sub> peaks indicate the extent of oxidation in the material.

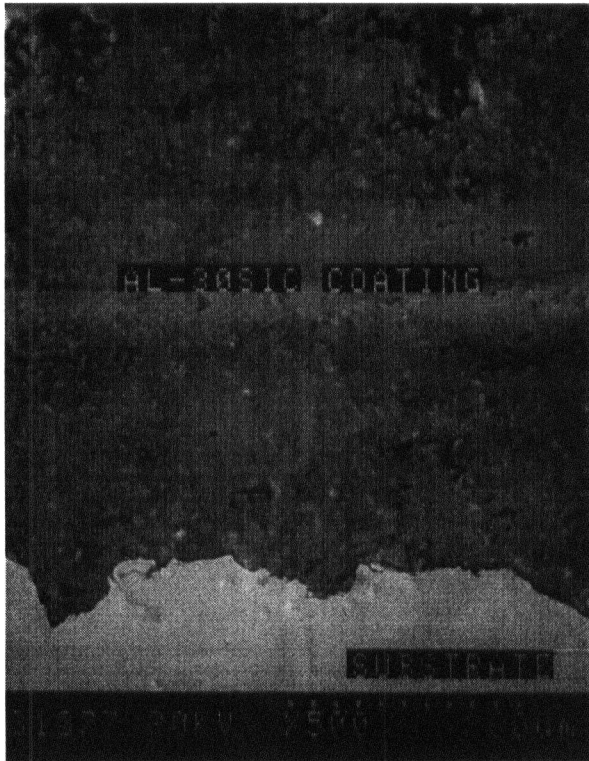


Fig. 36a

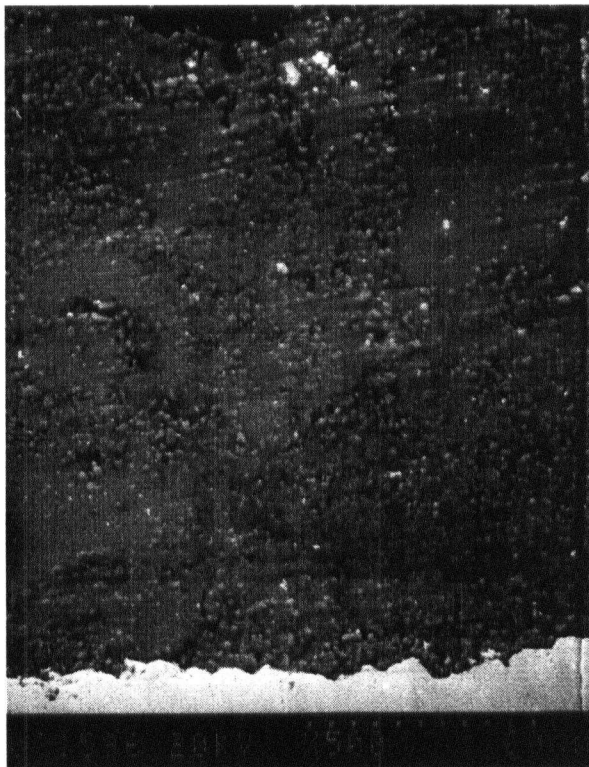


Fig. 36b

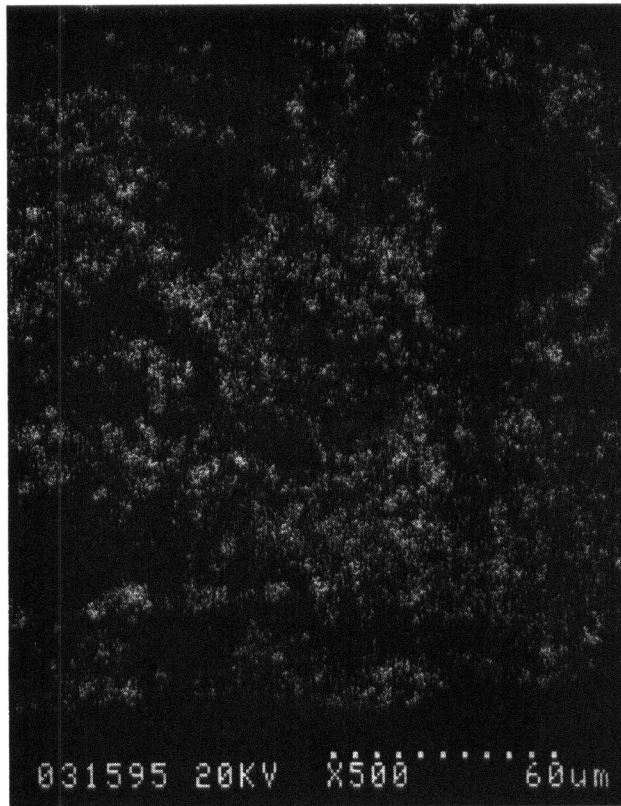


Fig. 36c

Fig. 36: a) Cross section of Al-30SiC1200 coating under SEM b) Cross section of Al-50SiC1200 coating under SEM. c) Si mapping of the Al-50SiC1200 coating in Fig. 36b.

The X-ray diffraction pattern of the Al-30SiC1200 coating, Figure 37, does not indicate the presence of silica. Silica should be in an amorphous form from the quenching of the coatings. The low volume of the amorphous silica, if present, are not expected to be detected by the X-ray. This indicates that most of the SiC particles

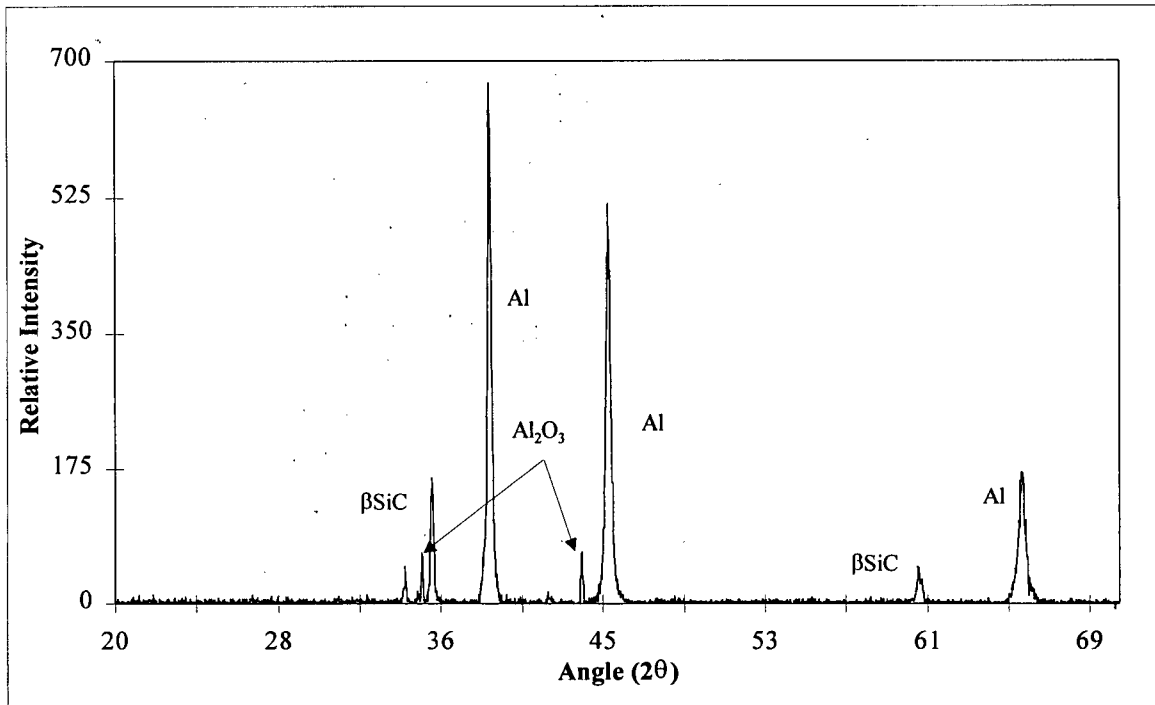


Fig. 37: X-ray diffraction pattern of Al-30SiC1200 coatings.

The SiC particles in the coatings showed a distribution and morphology similar to that in the powders that were sprayed. The presence of SiC was confirmed by X-rays of the coatings which showed a distinct SiC peak in addition to the Al peak. The SiC was distributed as individual particles in the matrix as shown in Figs. 36 a, b. The distribution of SiC was obtained by using back scatter X-ray mapping of Si along with the EDX. Figure 36c shows the Si mapping of the Al-50SiC1200 coating (shown in Fig. 36b) indicating some clustering of SiC (areas devoid of white spots). The homogeneity of the coatings improved with increase in the SiC particle size and also with the increase in the volume percentage of SiC in the composites. The homogeneity of the coatings was assessed quantitatively by measuring the interparticle distance ( $\lambda$ ) between the second phase particles.

The interparticle distance was measured by a method used by Stone and Tsakirooulos and is shown in Fig. 38 [16]. In this method, the interparticle distances between two successive particles, on any one of the superimposed straight lines, were obtained. Thus,  $\lambda$  is the distance between two successive particles obtained by tracing any given line in the microstructure. The variation in the interparticle distance indicates the degree of clustering in the microstructure. Similarly, in this investigation a few sample microstructures were chosen which were considered to be representative of the coating and the distances between the successive particles in any linear direction were obtained. The variations of the interparticle distance are shown in histograms for some of

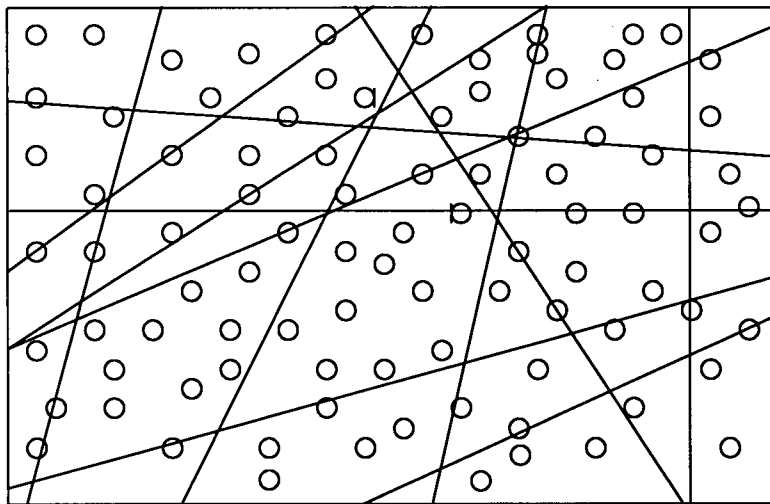


Fig. 38 : Schematic showing the method of estimating the interparticle distance between the second phase particles in a microstructure.

the Al-SiC coatings in Figs. 39 (a-d). In Figures 39 (b and d), the interparticle distances with the 1200 grit (8  $\mu\text{m}$ ) reinforcement particles are smaller than what was seen for the

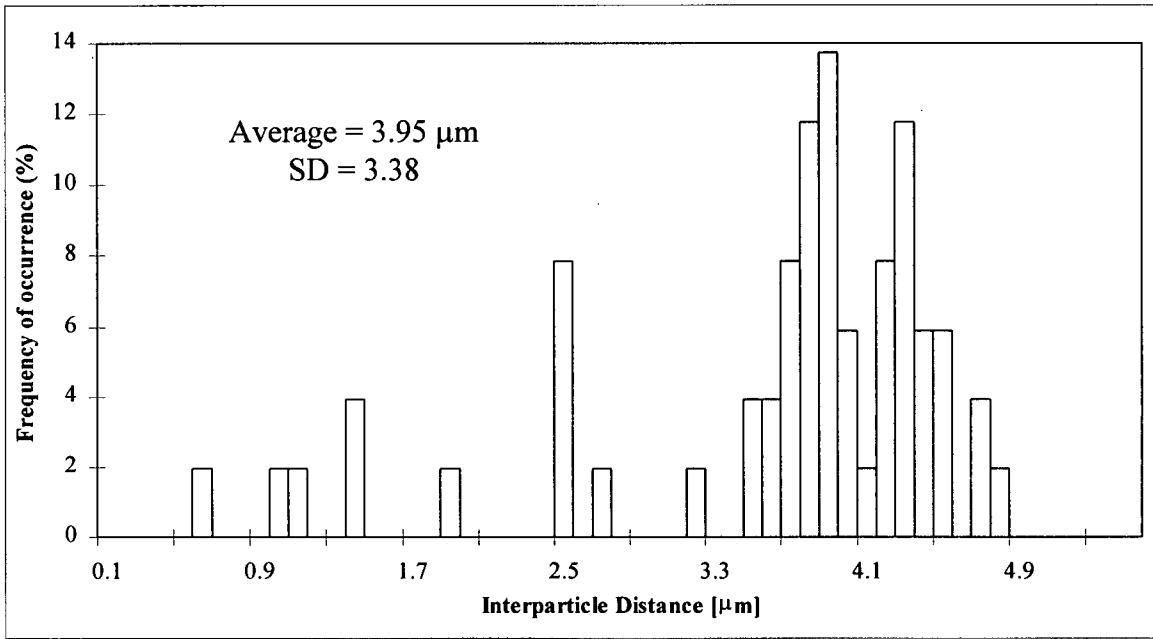
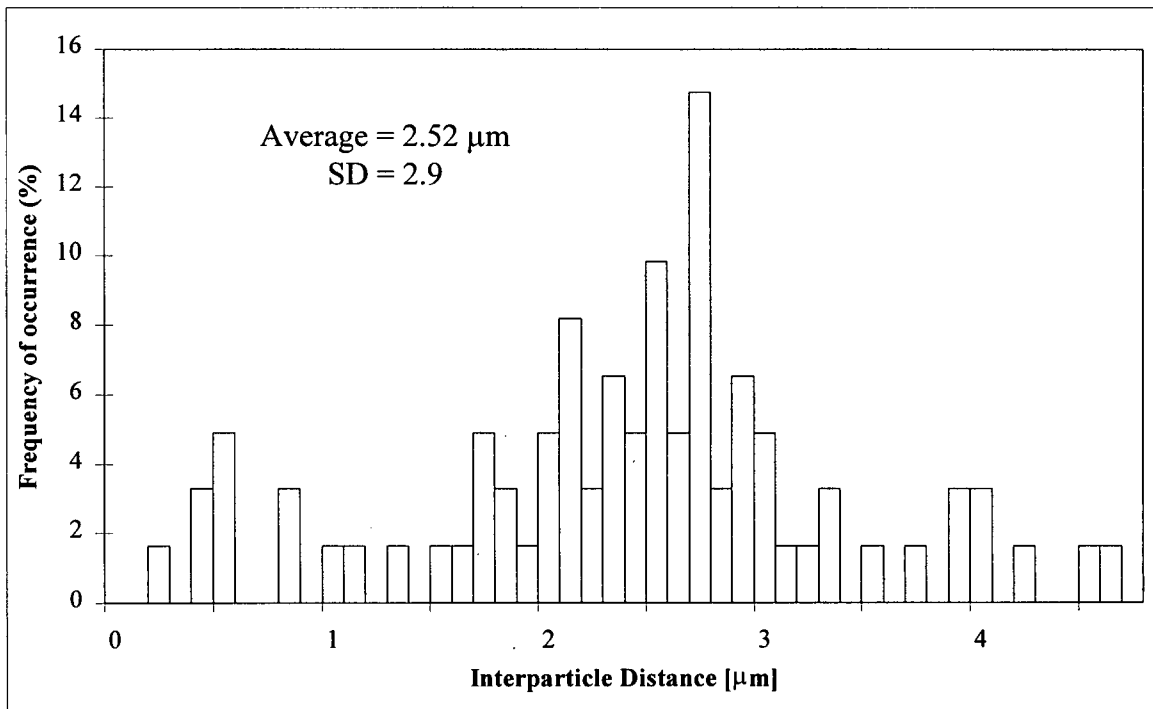


Fig. 39a: Distribution of the interparticle distance of Al-20SiC1200 coatings.



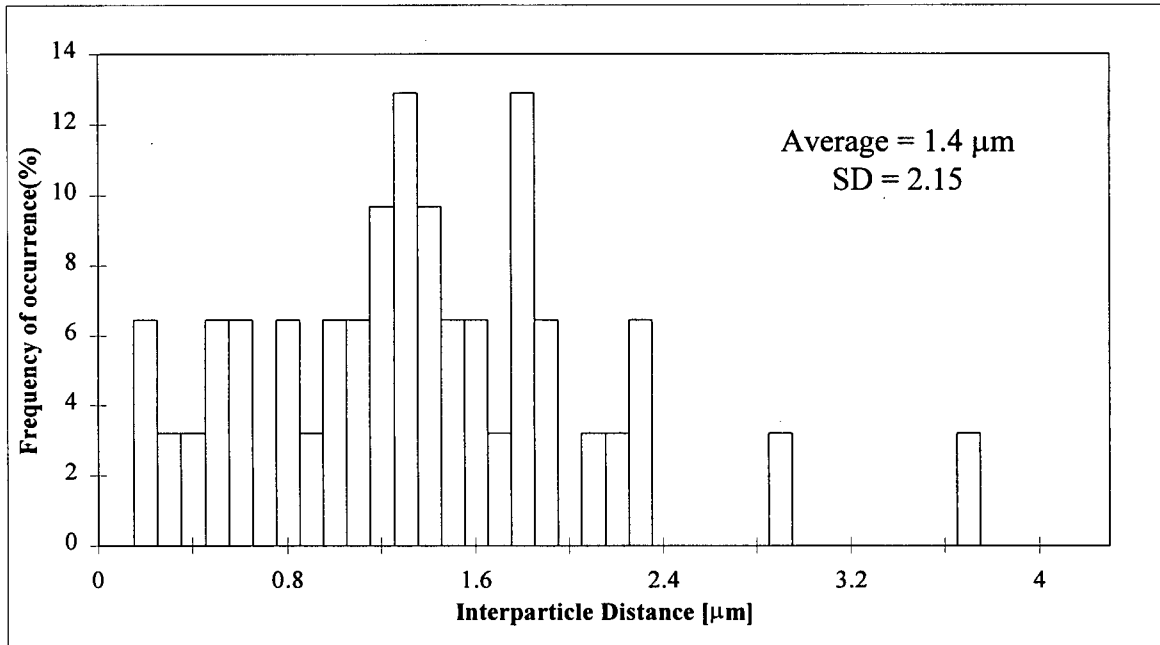


Fig. 39c: Distribution of the interparticle distance of Al-75SiC1200 coatings

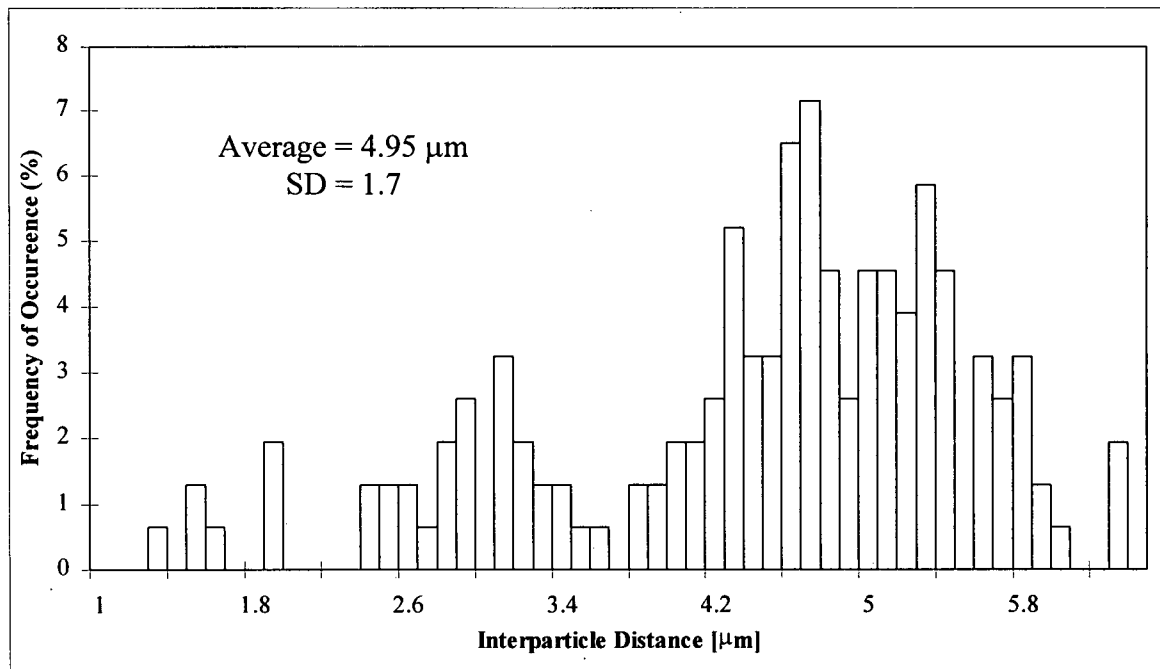


Fig. 39d: Distribution of the interparticle distance of Al-50SiC400 coatings.

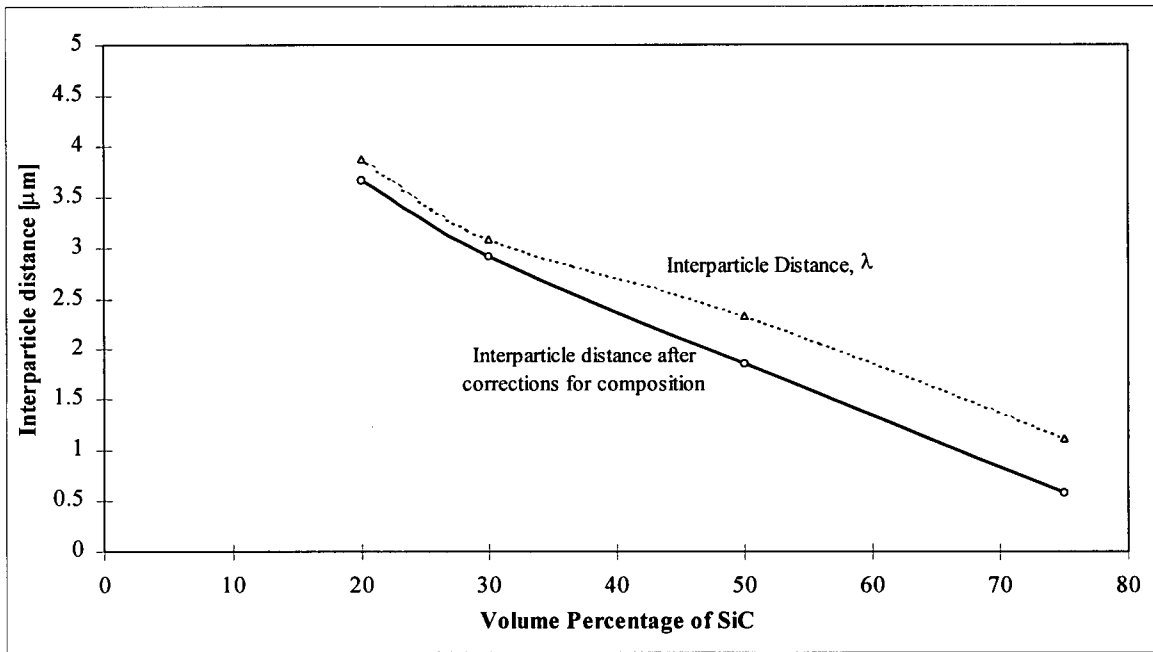


Fig. 40: Change in interparticle distance with SiC content in the composite.

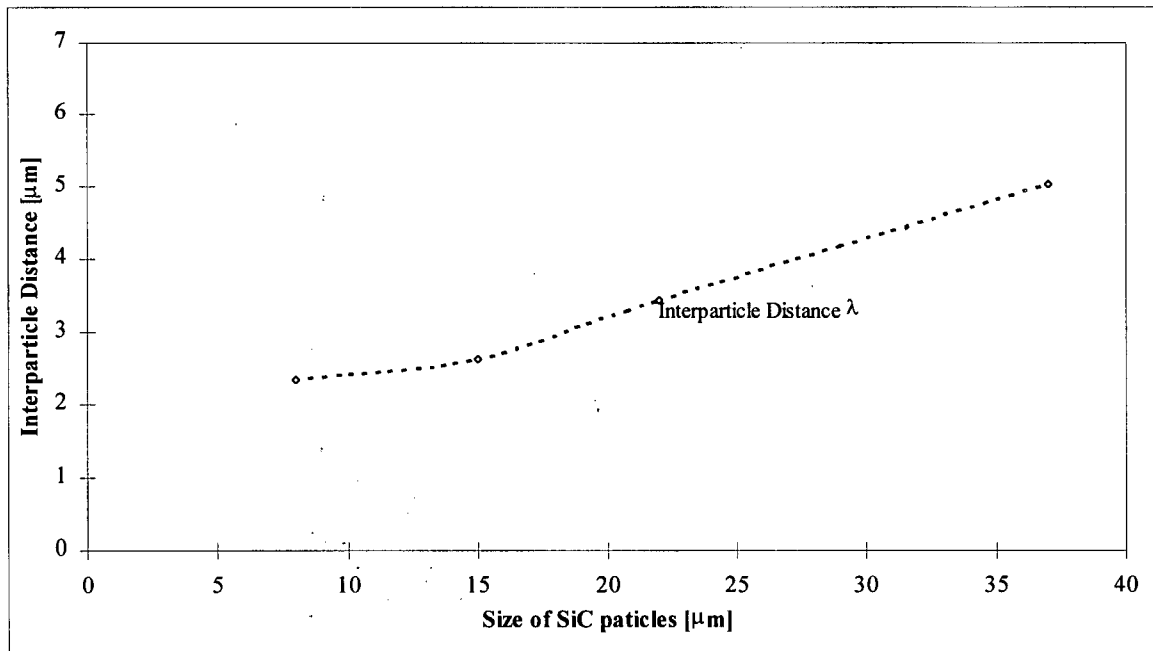


Fig. 41: Change in average interparticle distance with SiC particle sizes in Al-50vol%SiC composite.

400 grit (37  $\mu\text{m}$ ) particles for the same composition (50 vol% SiC) of the coatings. The range over which the  $\lambda$  varies gives an idea of the degree of clustering.

In Figure 39, the variation of the interparticle distance, (as indicated by the standard deviations (SD) of  $\lambda$ ) decreased with increase in the content of SiC in the matrix. Hence, the Al-20SiC1200 showed the highest variation and the Al-75SiC1200 had the least variation amongst the four coatings with the 1200 grit (8  $\mu\text{m}$ ) particle size. Similarly, the variation in  $\lambda$  values was found to decrease with increase in the SiC particle sizes. The above obtained results are similar to what has been reported elsewhere [16].

The change in average interparticle distance with SiC content and size in the Al matrix have been summarized in Figs. 40 and 41. The average interparticle distance was obtained from the weighted means of the values shown in Fig. 39. As expected, with the increase in the SiC content the interparticle distance decreased. In Figure 40, the change in the interparticle distance with the SiC content has been corrected by taking into account the actual SiC content in the composites obtained from the wet analysis method, Table 6. This is indicated by the line stating "Interparticle distance after correction for composition". As shown in Figure 41, the interparticle distance increased with the increase in the size of the second phase. Similar observations were also reported by Stone et. al [16].

### 5.3.2 Coating Hardness

The Vickers' microhardness values of the powders and coatings are summarized in Table 8. The Vickers test produced indentations which were between 40 and 50  $\mu\text{m}$

**Table 8.** Hardness of the mechanically alloyed powders and the subsequent coatings produced.

<b>Powder Composition</b>	<b>Hardness of the powders (VHN)</b>	<b>Hardness of the coatings (VHN)</b>
Al-20SiC1200	85	92
Al-30SiC1200	101	102
Al-50SiC1200	117	121
Al-75SiC1200	–	132
Al-50SiC800	122	124
Al-50SiC600	126	128
Al-50SiC400	130	134

in size under a load of 100 g. The composites having 1200 grit SiC as reinforcements had the average SiC particle size smaller than that of the indentation, and therefore the effect of microstructure on the hardness values should be minimal. Compared to the hardness of the coatings in Table 8, Al 6061 alloy had a maximum hardness value of 90 VHN (in ASTM T6 condition) [57]. The hardness values varied  $\pm 5\%$  from the mean for the first six powder compositions in Table 8. The 400 grit SiC powders had an average particle size which was comparable to that of the indentation size and hence, showed the highest variation in hardness values ( $\pm 25\%$ ). The Al-75SiC1200 had a flattened lamellar structure as shown in Figure 32. Thus, the indentations were not contained within the powder particles and hence no hardness values were obtained for this composition. The average hardness value increased with the increase in the SiC content and particle size of the reinforcement. The scatter in the results increased with the increase in SiC particle size. It is believed that this can be directly related to the increase in the interparticle distance with increase in SiC particle sizes. The increase in the interparticle spacing of SiC reinforcements produced an inhomogeneous hardness in the composite coatings.

The hardness of the coatings was higher than the hardness of the powders of the same composition. This difference can be attributed to formation of nitrides and oxides, during spraying. Although, the amount of oxygen in the coatings obtained through the XRD was insignificant, Mohanty et. al [8] suggested that the traces of dispersed oxides and nitrides increases the hardness of the coatings by a factor of 4.

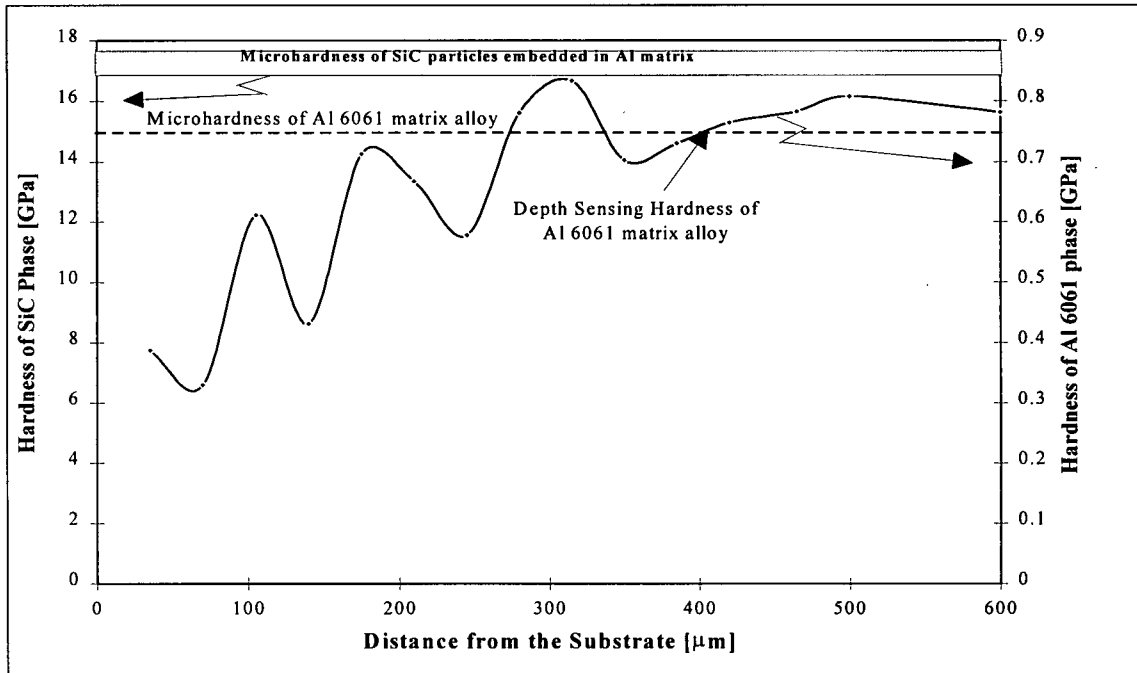


Fig. 42: Change in hardness (using depth sensing indentation) of an Al-30SiC1200 coating with increase in the distance from the substrate. The microhardness values of Al 6061 alloy, SiC reinforcements in the coating and Al-30SiC1200 have also been shown.

The hardness values using the depth sensing indentation had large variations due to microstructural inhomogeneity. The indentations produced by the nano-indenter under a load of 30 g were approximately 5  $\mu\text{m}$  in size. The small size of the indentations allowed measurement of hardness at close intervals. The variation of the hardness along the coating cross section for the Al-30SiC1200 composite is shown in Figure 42. The

hardness of the coatings increased with distance from the substrate. Similar trends have been reported elsewhere for plasma sprayed ceramic coatings [61].

One of the main drawbacks in using the depth sensing indenter is that the size of the indentation is comparable to the interparticle distance. The values shown in Figure 42 have been obtained for the matrix material after eliminating the aberrations due to microstructural inhomogeneity. The range hardness values of the SiC particles have been shown separately in Fig. 42. They are less than that obtained for a sintered SiC particle (27 GPa). The difference can be attributed to the presence of the softer Al matrix below the SiC particles in the composites. The coating layers adjacent to the substrate have the highest cooling rate and due to the immediate buildup of further sprayed layers the splats adjacent to the substrate have the highest amount of residual stress. This residual stress might be responsible for causing damage in the coatings, e.g., producing cracks in the Al-SiC interface, which reduces the hardness of the coatings. This may be the prime reason for the low hardness near the substrate.

### 5.3.3 Adhesion Strength

#### a) Tensile Adhesion Tests (TAT)

Tensile Adhesion Tests (TAT), were conducted according to the ASTM standard C633-79 test, Figure 16. These proved to be inconclusive as very few of the failures were limited to the coating/substrate interface. The results obtained from the TAT are summarized in Table 9. Most of the failures occurred at loads between 68-75 MPa.

**Table 9.** Summary of ASTM C633 pull adhesion test results

<b>Substrate material</b>	Al20SiC1200	Al30SiC1200	Al50SiC1200	Al75SiC1200
Aluminum	75MPa	72MPa	76MPa	68MPa
Mild steel	68MPa	72MPa	69MPa	70MPa

Due to the inconclusive nature of the results obtained with 1200 grit SiC composites, the TAT was not conducted for compositions other than those mentioned in Table 9. The failure of the test specimens can be in three possible ways: 1) interfacial failure, which occurs at the coating-substrate interface, 2) cohesive failure within the coating or, 3) mixed mode failure which is a combination of the above two failure paths. However, any one of the above modes of failure can occur only if the bond strength of coating is less than that of the adhesive used. Although the epoxy (EC-1386) used for the tests had a maximum tensile strength close to 120 MPa, such high values were rarely obtained. Most of the failure surfaces were not limited to a single plane and the cracks propagated between the coating-adhesive or adhesive-substrate interfaces and in some samples cohesive failures occurred within the coating. Lin et. al. [36] argued that the inhomogeneity and defective nature of coatings produced local stress concentrations within the coating and hence the stress distribution should be far from uniform. This also produces the shear component and the results of TAT often shows a wide scatter.

b) Peel Adhesion Test (PAT)

The Peel Adhesion Test (PAT) results for the different powder compositions on different substrates are summarized in Table 10. Some of the typical peel strength curves

of the composite powders on various substrates are shown in Figs. 43 (a-e). The peel curves as seen in Fig. 43 are not smooth curves but show significant variations. The variations resulting from the test process itself have been estimated by Sexsmith et. al [41] to be  $\approx 10\%$  of the average peel strength. Many of the large variations in strength can

**Table 10.** Summary of peel test strength in N/m (without calibration).

Foil material	Foil thickness [ $\mu\text{m}$ ]	Al-30 SiC1200	Al-50 SiC1200	Al-75 SiC1200	Al-50 SiC800	Al-50 SiC600	Al-50 SiC400
Ni	178	2460	1760	1415	1820	1925	2140
Steel	178	950	780	595	ND	ND	ND
Stainless Steel	102	530	510	510	ND	ND	ND
Al.	76	ND	>2880	ND	ND	ND	ND
	152	ND	3180	ND	3330	4060	>4690

• ND = Not Determined

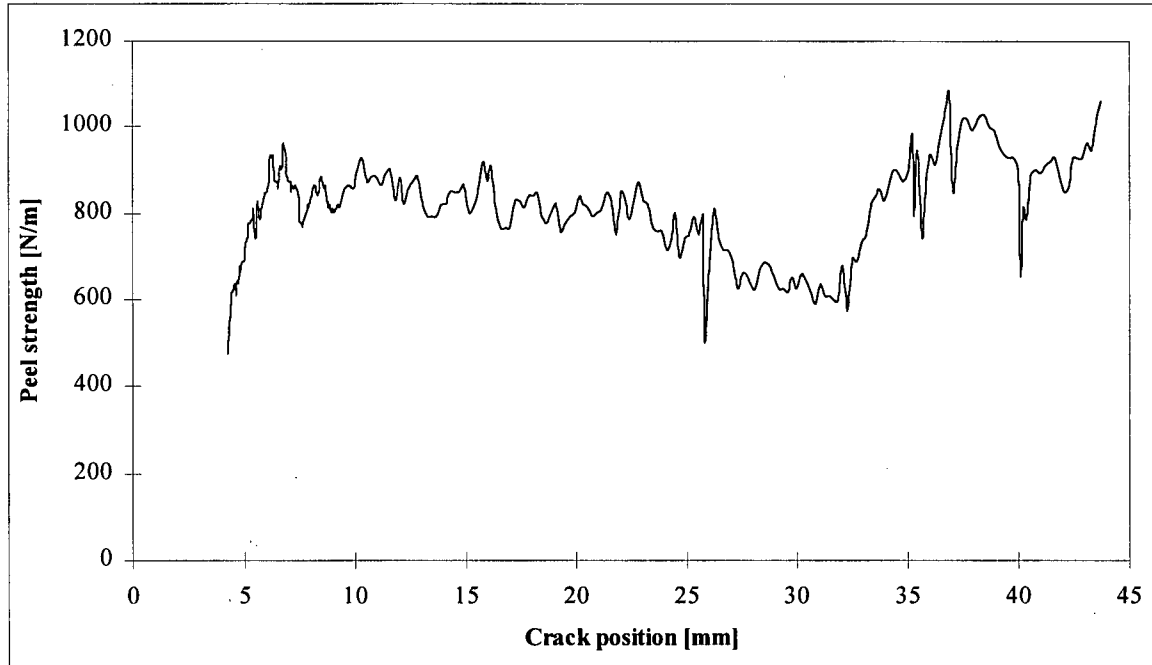


Fig. 43a: Peel strength of an Al-20SiC1200 coating on 0.007" Ni foil.

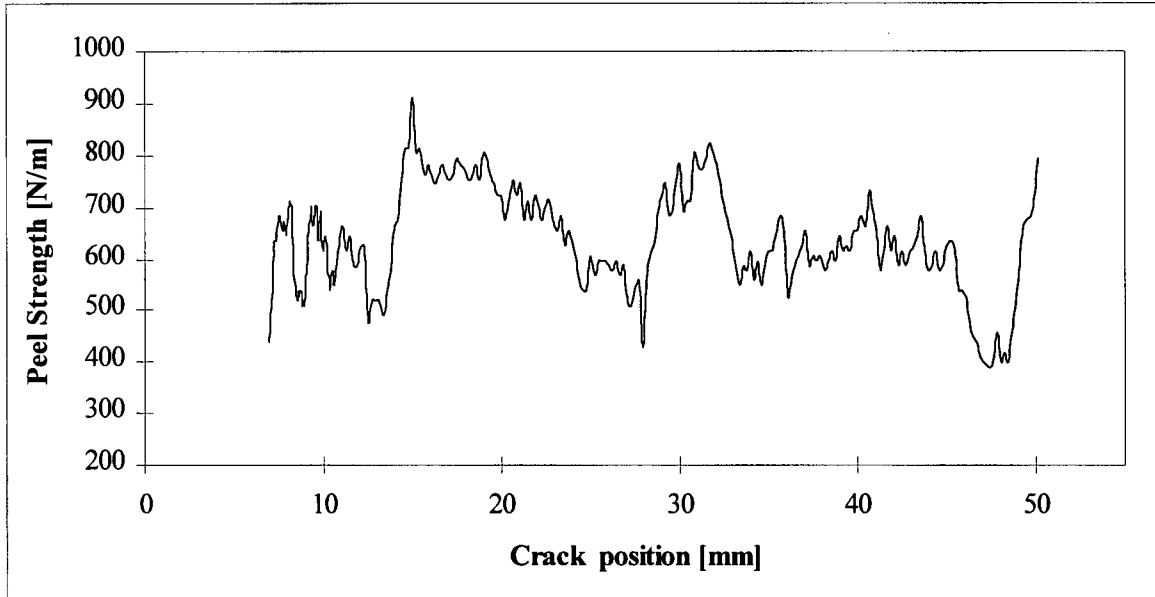


Fig. 43b: Peel strength of an Al-30SiC1200 coating on 0.007" Ni foil.

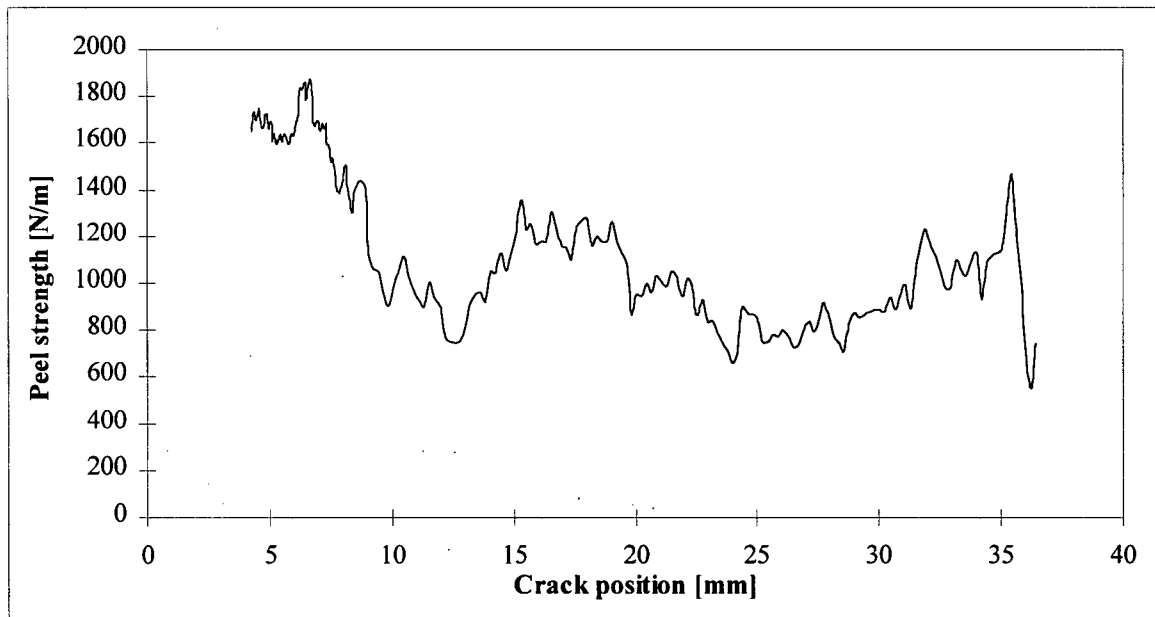


Fig. 43c: Peel strength of an Al-50SiC800 coating on 0.006" Al

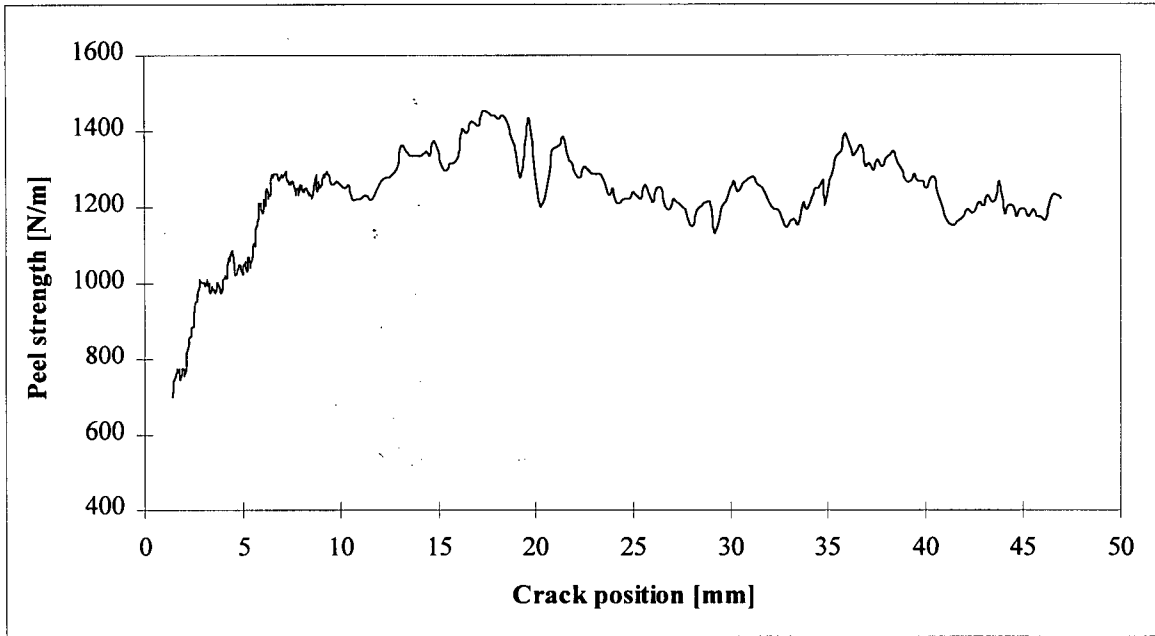


Fig. 43d: Peel strength of an Al-50SiC600 coating on 0.007" Ni

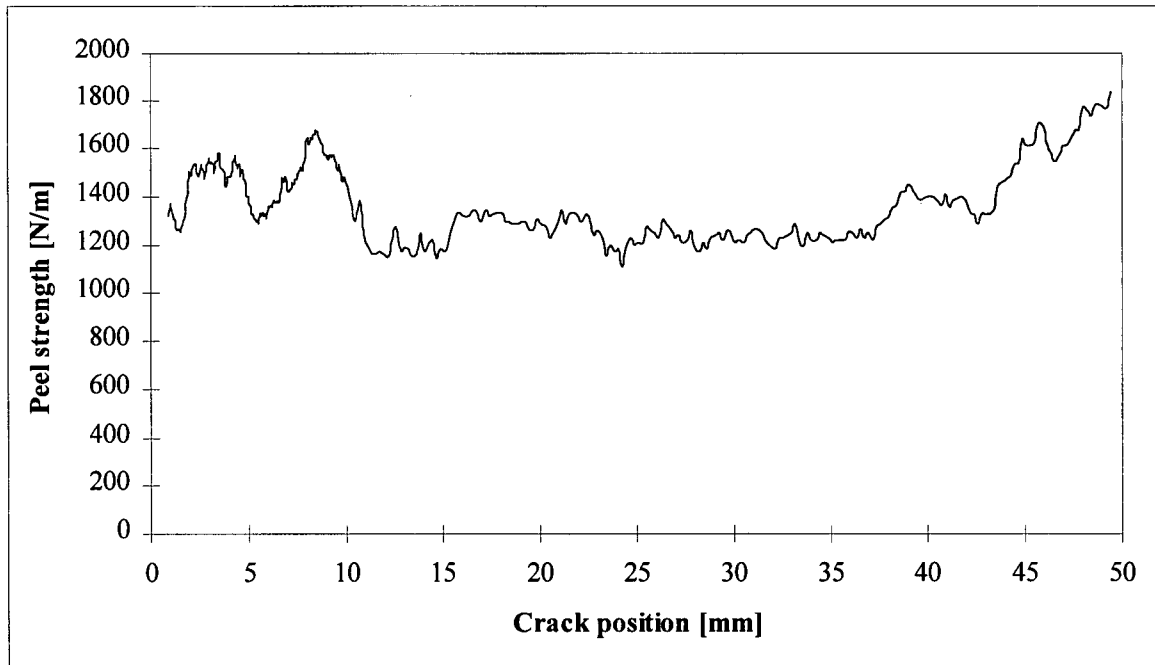


Fig. 43e: Peel strength of an Al-50SiC400 coating on 0.007" Ni

be attributed to surface defects on the substrate or macrostructure of the coating in that localized zone. The average peel strengths were obtained after eliminating the variations in strength due to localized surface defects.

The values of peel strength in Table 10 include the plastic work done on the foil during peeling and the friction between the foil and the mandrel. Methods to assess and estimate the friction force between the foils and the mandrel have been suggested by Sexsmith et. al [39]. The friction force is directly proportional to the force holding the foil against the mandrel and hence is also proportional to the peel strength [39-44]. Similarly, the plastic work is also directly proportional to the peel strength. Thus, by eliminating the friction and plastic work the actual peel strength values have been obtained and are shown in Table 11.

**Table 11.** Summary of peel test strength in N/m (after calibration).

Foil material	Foil thickness [μm]	Al-30 SiC1200	Al-50 SiC1200	Al-75 SiC1200	Al-50 SiC800	Al-50 SiC600	Al-50 SiC400
Ni	178	1840	1560	1100	1350	1360	1350
Steel	178	740	615	470	ND	ND	ND
SS.	102	420	400	400	ND	ND	ND
Al.	76	ND	>2000	ND	ND	ND	ND
	152	ND	2250	ND	2350	2950	3500

\* ND = Not Determined

The adhesion strength of the coating was highest when Al substrate (foils) were used. Nickel showed the next highest average peel strength for a given composition of the powder, while stainless steel (SS) showed the lowest adhesion strength. The low flow stress of Ni, compared to that of steel or stainless steel foils, is one of the probable reasons for the high peel strength. The low flow stress allows an easier relaxation of the residual stress in the coatings. There are two possible reasons for the high adhesion

strength shown by Al substrates. Al has a lower flow stress than Ni and thus can accommodate higher residual stresses at the interface. Also, as shown in Fig. 44, there is a considerable fusion at the interface of the coatings and the Al foils. Aluminum having a low melting point (667°C), most likely develops a thin molten layer at the interface during spraying. The molten Al of the coatings form a continuous medium with the molten substrate Al, thereby eliminating a regular interface. Thus, the peeling in these cases occur by fracture through the Al matrix.

There is no well established conversion factor available to correlate the peel strength results to the ASTM tensile adhesion test. The results of the peel strength tests compare favorably with the reported results for the other commercially used coatings [39-42].

The change in average peel strength with SiC content is shown in Fig. 45 for Ni and steel substrates. The peel strength decreased with the increase in SiC content for all the different substrates used in this investigation. This can be directly related to the variation in interparticle distance,  $\lambda$ , with increasing concentration of the SiC reinforcements. The increase in the content of the ceramic particulates reduces the interparticle distance and also reduces the area fraction of metal in contact with the substrate at the interface. Since metallic coatings have a higher adhesion strength [39], the decrease in metal content at the interface reduces the peel strength of the composite. Moreover, since the Al in the MMC only melts during spraying, there is no actual bonding between the SiC particles and the substrates. The peel strength was also found to be directly proportional to the SiC particle size, Figure 46.

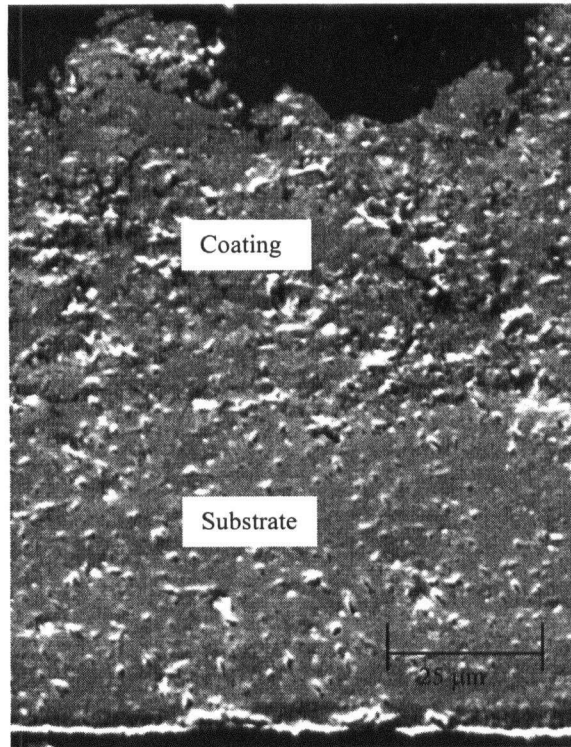


Fig. 44a

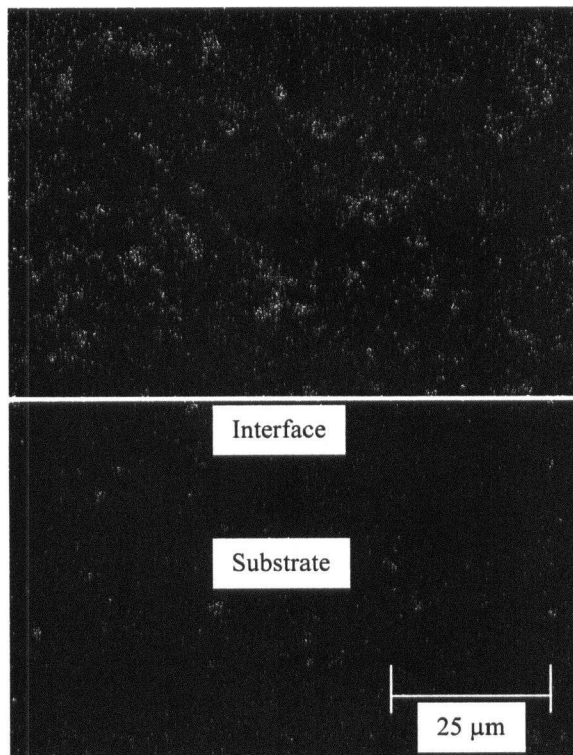


Fig. 44b

Fig. 44: a) Al-50SiC400 coating on an Al foil observed under SEM showing the removal of a regular interface. b) Si map of Fig. 44a showing the distribution of the SiC.

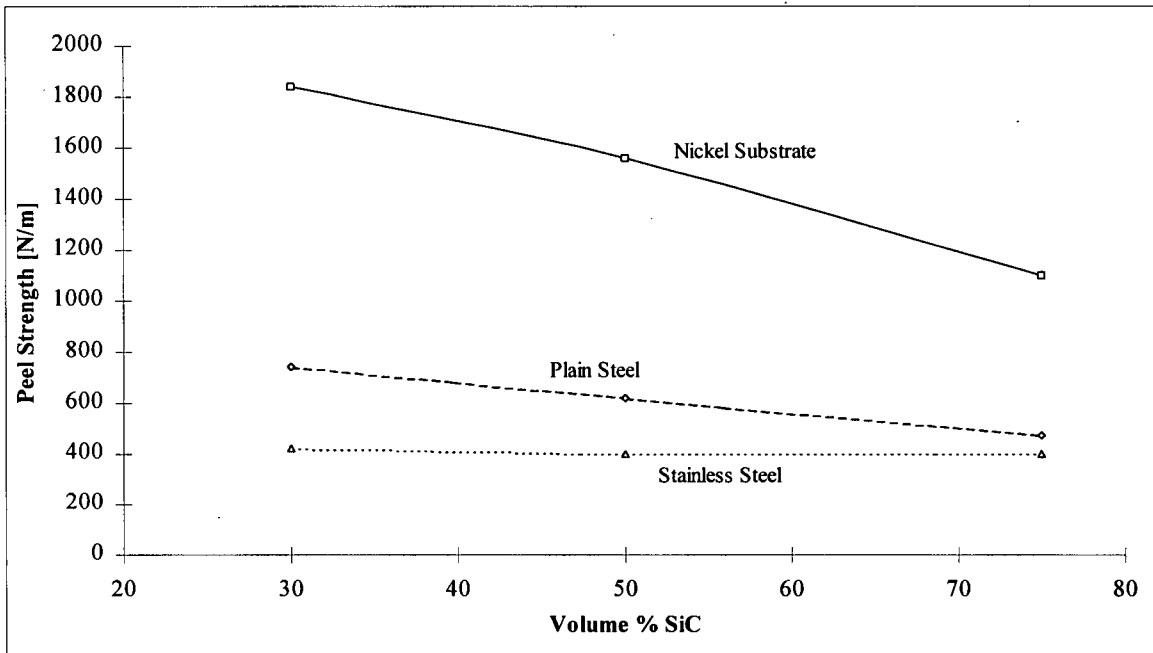


Figure 45: Variation of the average peel strength with SiC content for different substrates.

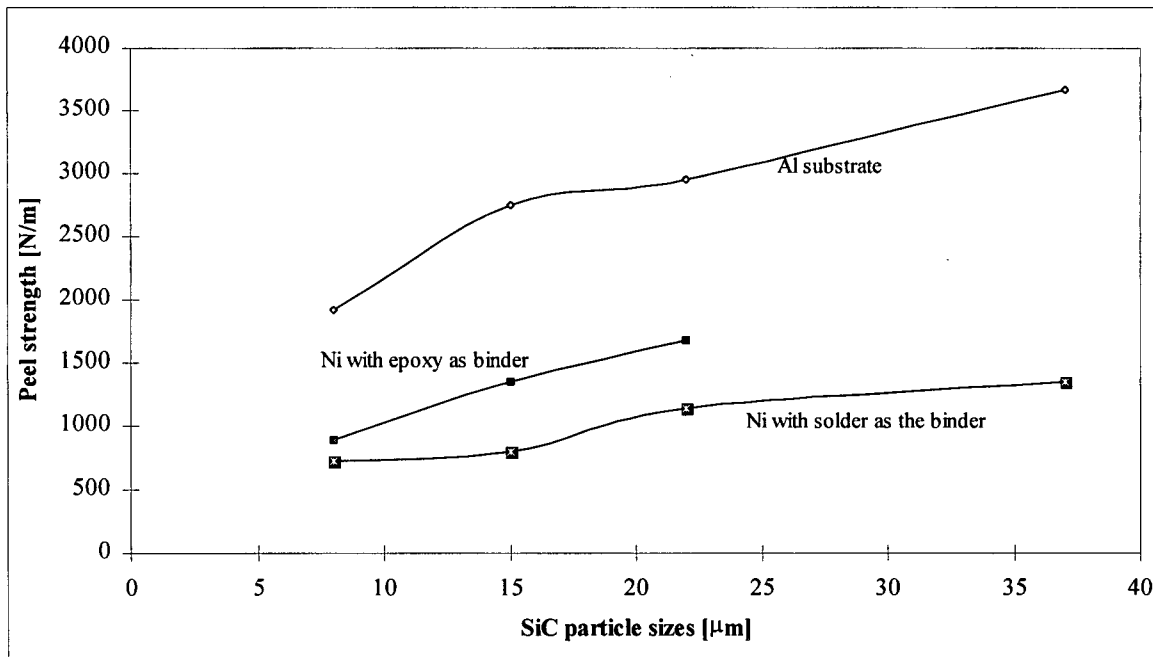


Figure 46: Variation of the Peel strength with the SiC particle sizes.

This observation can similarly be explained by the change in metal content at the interface with reinforcement size. It is believed that the resultant higher area of metal at

the interface for larger content of SiC reinforcements is the probable reason for this increase.

### 5.3.4 Wear Tests

#### a) *Abrasive Wear Tests*

The results of the abrasive wear tests using SiC abrasive papers are shown in Figs. 47 and 48. In Figure 47 changes in the wear rate with SiC content is shown for the four different compositions of MMC, whereas Figure 48 shows the wear resistance with the different SiC particle sizes. The wear of the coatings was assessed by the weight and volume loss of the samples. The wear properties of all the coatings were either similar or better than the commercially available Al-20Al<sub>2</sub>O<sub>3</sub>/400 cast and extruded composites which were used as the reference for comparing wear resistance. The wear resistance of

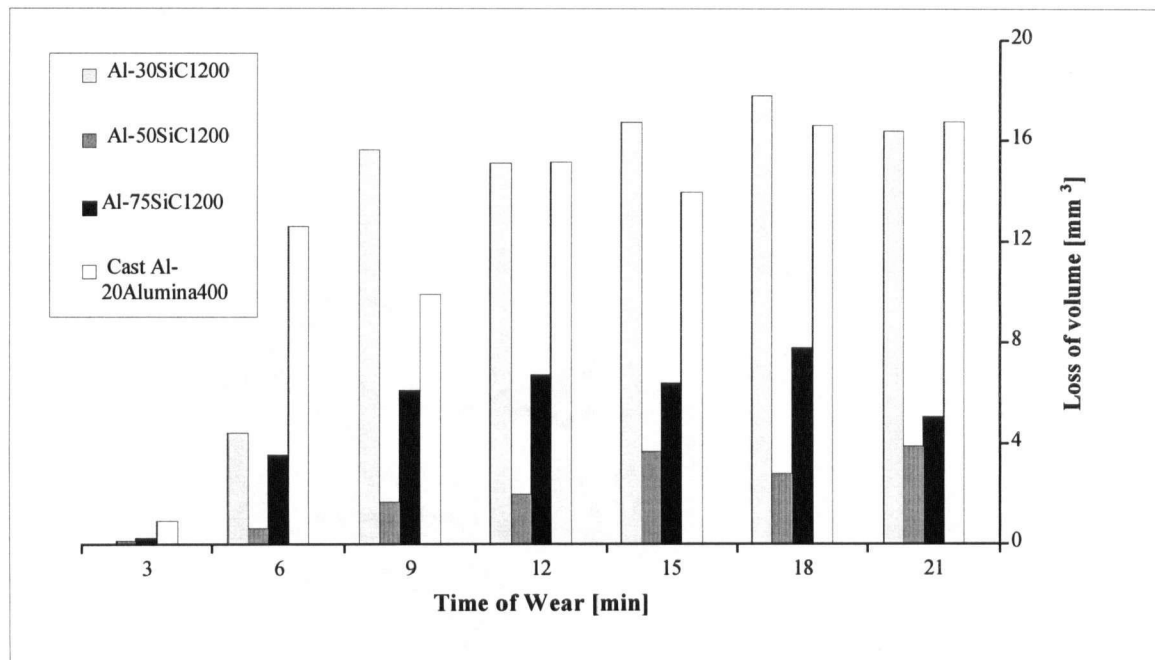


Fig. 47a : Change in abrasive wear resistance with SiC content under a load of 35 N.

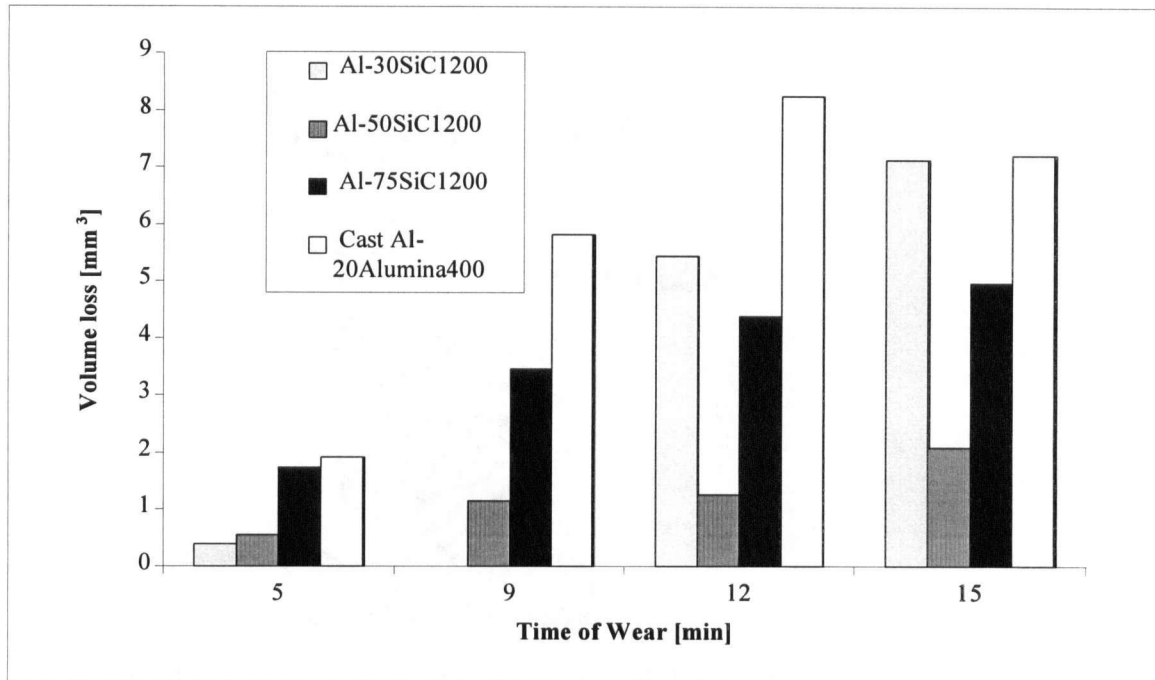


Fig. 47b: Change in abrasive wear resistance with SiC content under a load of 20N.

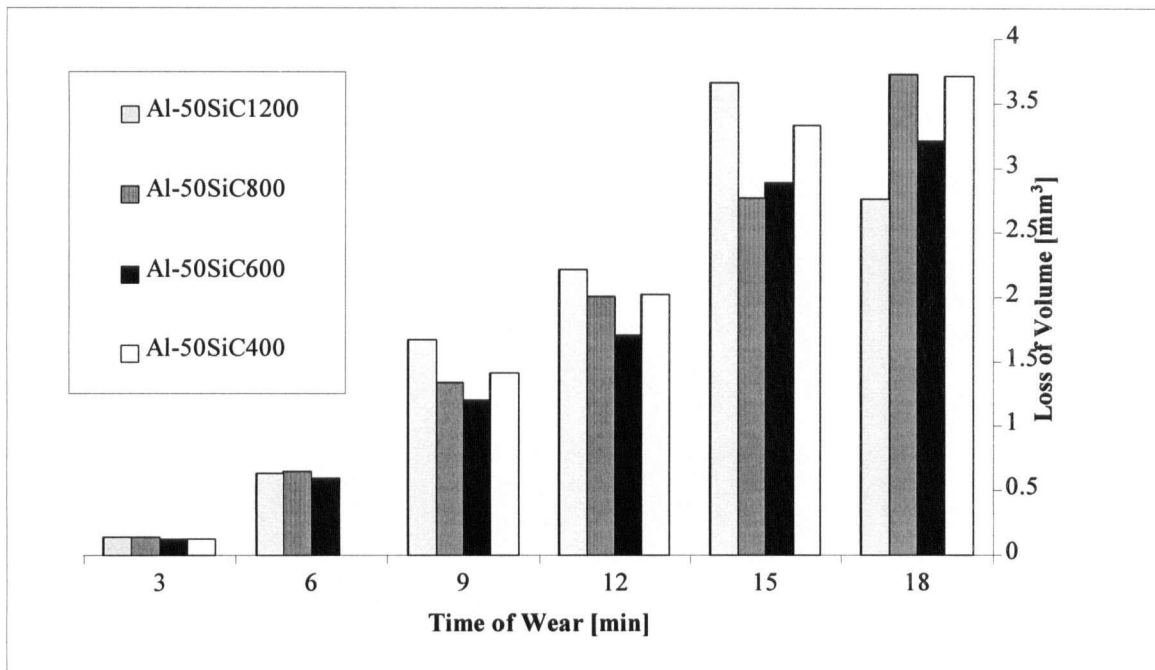


Fig. 48a: Change in abrasive wear resistance with SiC particle size under a load of 35 N.

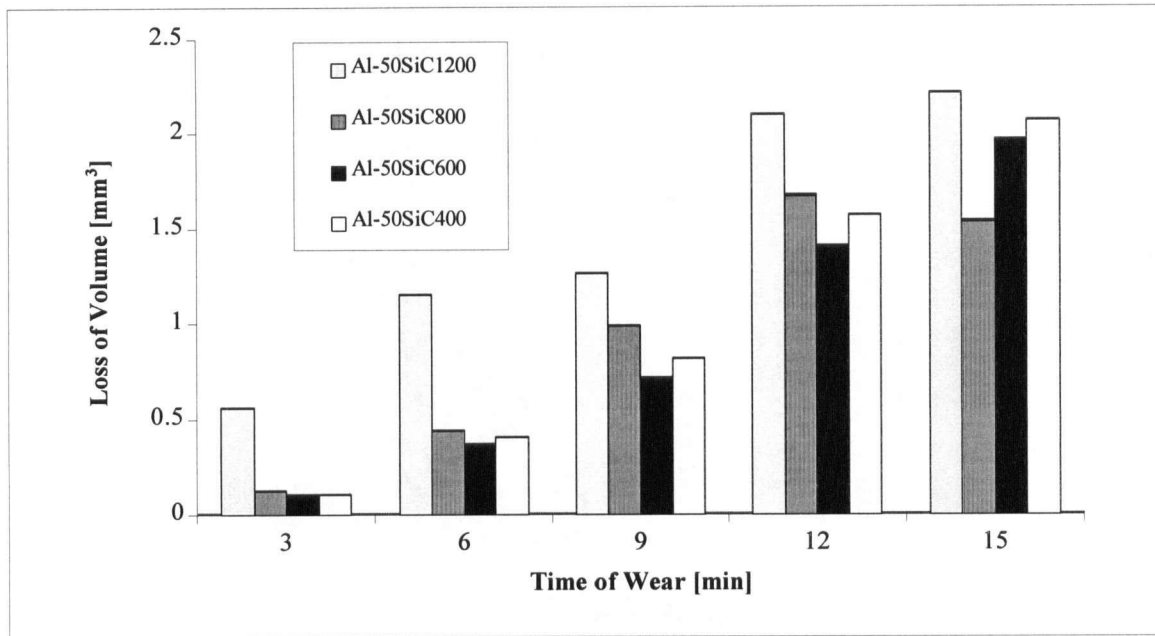


Fig. 48b: Change in abrasive wear resistance with SiC content under a load of 20 N.

the composites increased with the increase in SiC content up to a maximum value of 50 volume percent, Fig. 47 a, b. Amongst the four compositions presented in Fig. 47a, Al-50SiC1200 showed the highest wear resistance. The wear resistance of Al-30SiC1200 was comparable to that of the reference Al-20Al<sub>2</sub>O<sub>3</sub>400. The wear resistance of the composites did not change significantly with the SiC particle sizes as shown in Figs. 48 (a, b). The abrasive wear resistance of Al-50SiC600 was higher than any of the other coatings of same composition and the reference Al-20Al<sub>2</sub>O<sub>3</sub>400 composite.

To eliminate the variations or errors in the abrasive wear test, the experiments were repeated under different loads of which the results at high and low loads of 35 N and 20 N are presented. By comparing the wear behavior under different loads the experimental errors could be estimated. For example, the instances where wear volume decreased with increase in wear time can be attributed to the errors in the experimental

procedure. Similar observations of the dependence of wear resistance of composites on the second phase size and content have been also reported by others [11] .

Archard's law states that the wear resistance of a material is directly proportional to its hardness values. However, this is not always true for the composites, as wear resistance is also dependent on the toughness of the composite and strength of the Al/SiC interface. Thus, although the hardness of Al-75SiC1200 was higher than other coatings with 1200 grit (8  $\mu\text{m}$ ) SiC as shown in Table 8, the wear resistance was not the highest. It is expected that the low volume of the matrix metal produces a weak interface, resulting in easy pullouts and hence a low wear resistance of the coatings. A similar observation was reported by Mohanty et. al [8] for Ti/TiC coatings.

b) Erosive Wear Test

The results of the erosive wear tests are summarized in Figs. 49 and 50. Figure 49 shows the variation in the erosive wear resistance with SiC content and Fig. 50 shows the changes with SiC particle sizes. The erosive wear resistance improved with increase in SiC content. Al-75SiC1200 showed the highest erosive wear resistance amongst the four coating compositions having 1200 grit SiC and the Al-20Al<sub>2</sub>O<sub>3</sub>400 reference composite. The increase in the SiC particle size decreased the erosive wear resistance. Al-50SiC800 coatings showed a higher erosive wear resistance amongst the four powders of that composition, Figure 50.

The results of the erosion test can be explained by studying the mechanism of erosive wear in composite materials and observation of the eroded surface. Erosion in

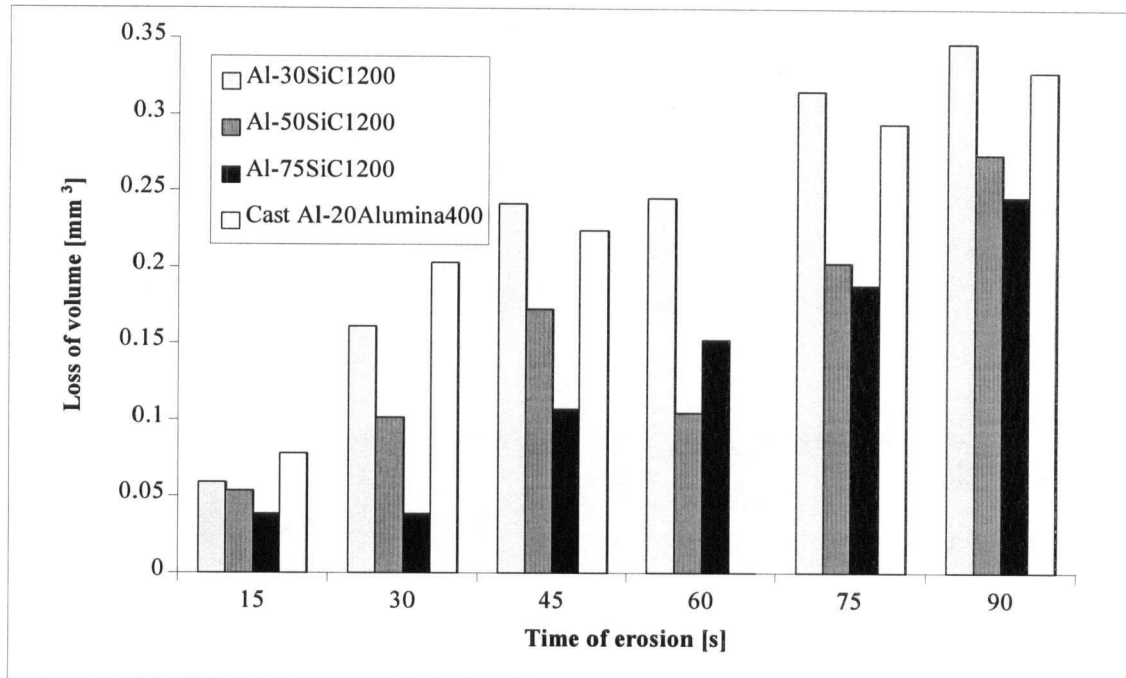


Fig. 49: Variation of erosive wear resistance with SiC content in the composite.

- - Data for the wear of the cast composite material was not available for  $t = 60s$ .

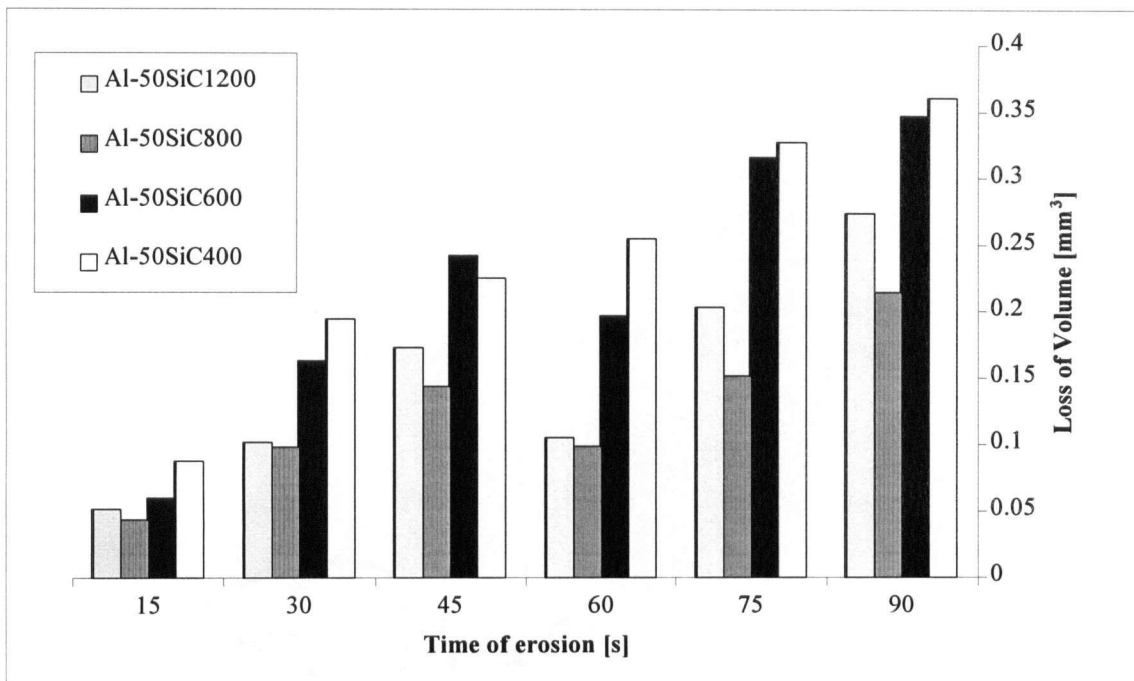


Fig. 50: Change in erosion wear resistance with SiC particle sizes.

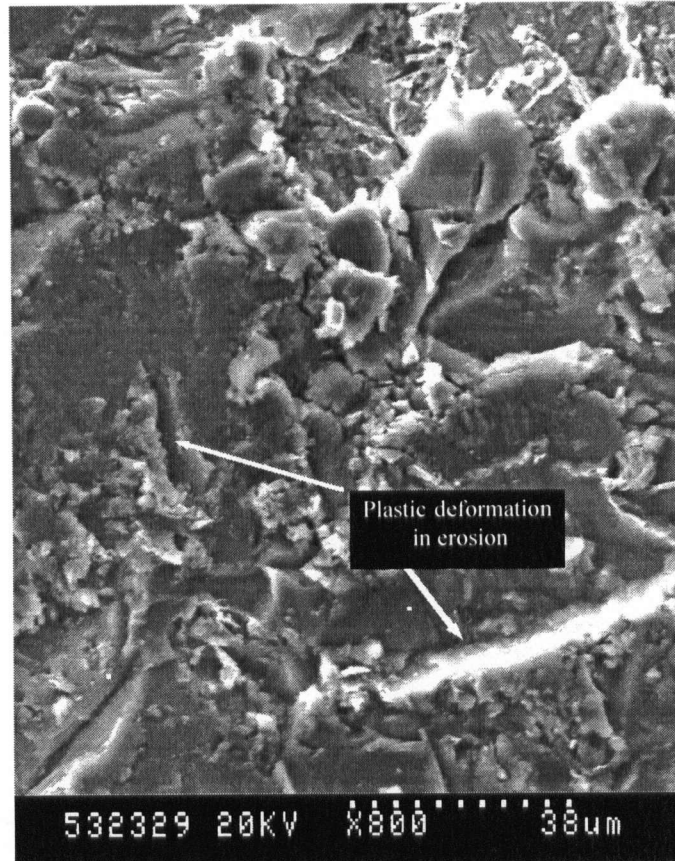


Fig. 51: Erosion surface of Al-50SiC800 coating showing plastic deformation

MMC can occur by two mechanisms: plastic deformation of the ductile matrix or by brittle fracture of the reinforcements. SiC having a higher hardness ( $H_v = 28.0$  GPa under a load of 2N) [58] than the eroding medium,  $Al_2O_3$  - ( $H_v = 23.0$  GPa under a load of 2N) [58] is not expected to undergo significant brittle fracture. This was found to be so from the inspection of the eroded surface in Fig. 51. As shown in the microstructure, the eroding medium leaves distinct eroded marks (areas as labeled in the microstructure) from plastic deformation in the Al matrix. Hence, deformation and removal of the ductile Al is the dominant erosive wear mechanism. The extent of wear depends on the size and

depth of the indentation left from the impact of the individual striking particles. The indentation size depends on the size of the hard phase particles and the interlamellar spacing.

Thus, the mechanism described above provides a reasoning for the improvement in erosion resistance with SiC content. The Al-75SiC1200 coating has the least interparticle distance amongst the composites with same sized SiC reinforcements. Thus, the least amount of ductile Al was exposed to the eroding medium and hence the wear of these coatings was the least amongst the composites in Fig. 49.

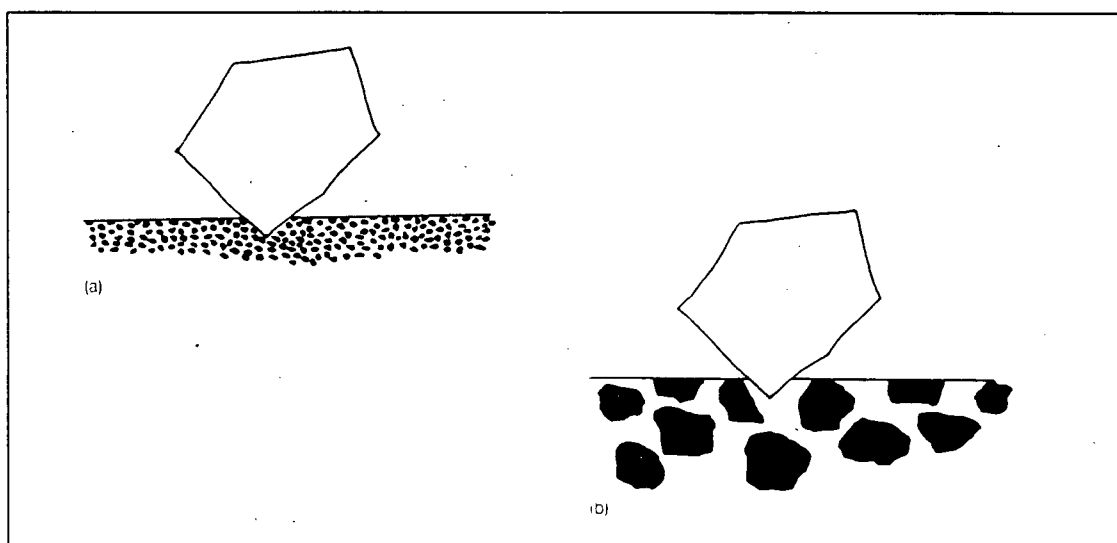


Fig. 52: Dependence of the erosion wear properties with reinforcing particle sizes.

Figure 52 helps in explaining the change in wear resistance with SiC particle size. The increase in SiC particle size increases the interparticle distance and this exposes a greater area of the matrix Al to the erosive medium. The inter-particle spacing is comparable to indentation size caused by the impinging abrasives on Al and depending

on the abrasive particle force and geometry it can lead to crack formation by plastic flow or fracture at the interface. Thus, the abrasive wear resistance decreases with increasing SiC particle size. Although, Al-50SiC1200 had the smallest size of the reinforcements ( $\approx 8 \mu\text{m}$ ) and hence the least interparticle distance, it did not show the highest wear resistance amongst the coatings of same composition. This may be because of the microstructural inhomogeneity of the Al-50SiC1200 coatings compared to that of Al-50SiC800 coatings. The inhomogeneity produces clustered areas in the microstructure with high concentration of SiC and having other areas devoid of any reinforcement, Fig. 31b. Thus, the Al-50SiC800 coatings had the highest erosive wear resistance amongst the coatings of Al-50vol%SiC compositions.

## **Chapter 6: Interparticle Distance: Model vs Experiment.**

### **6.1 Background**

From the observations in the present study, it can be concluded that one of the key features obtained from the present investigation is the correlation of wear, adhesion and other physical properties of the Al-SiC composite coatings with the concentration and size of SiC particles. For example, the peel adhesion strength of the coatings, was found to change with the SiC content and particle sizes, Figures 45, 46 respectively. Investigation of the wear mechanisms by Chung et. al [11] proved that the interparticle distance between the second phase particles is critical in determining the wear resistance of the coatings. Thus, attempts were made in this work to correlate the properties with the SiC interparticle distance,  $\lambda$ , within the Al matrix.

The interparticle distance,  $\lambda$ , was measured from the photomicrographs of the coatings using the method shown in Fig. 38 and discussed in section 5.3.1. This method provides the distribution in the two dimensions, on a plane perpendicular to the surface of the coating. However, because of the low thickness of the coatings the interparticle distances were calculated assuming a similar distribution in the third dimension.

### **6.2 Geometric Model**

The interparticle distance can be calculated from the type of packing by which the SiC particles are arranged in the Al matrix. Three commonly found packing types -

simple cubic, hexagonal prismatic (HCP) and rhombic dodecahedron are considered and are shown in Fig. 53.

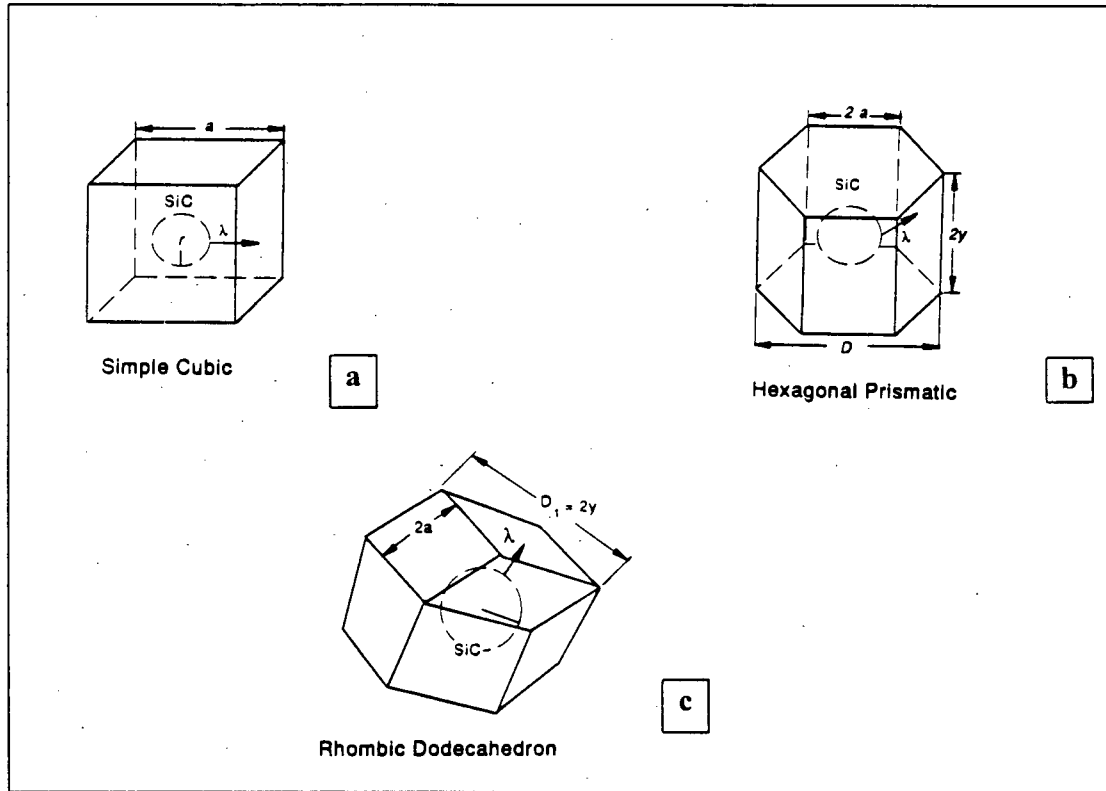


Fig. 53: Commonly found modes of packing considered in the present model. a) Simple cubic b) Hexagonal prismatic c) Rhombic Dodecahedron.

### 6.2.1 Assumptions

In the development of the geometric model of the interparticle distance  $\lambda$ , the following assumptions are made:

- 1) Unit cell represents the typical composition of the material.
- 2) Particles are spherical in shape.
- 3) Particles are of uniform size.

- 4) Particles centers coincide with the center of each cell.

### 6.2.2 Derivations and Experimental Verifications

In calculating the interparticle distance ( $\lambda$ ), it is assumed that the volume of each cell can be represented by the composition of the coating. Thus, the volume of each unit cell is composed of the volume of SiC particle and the Al matrix surrounding it. It was also assumed that the geometric center of the cell was the same as the center of the reinforcing particle and based on that the distances between the particles are obtained. The interparticle distance " $\lambda$ " is determined as the distance between the surfaces of particles of adjacent SiC reinforcements. The details of the derivations are shown in Appendix (I).

As a result, the interparticle distance  $\lambda$  for the geometric models considered are given by the following equations:

Simple Cubic Packing:

$$\lambda = 2(a/2 - r) \quad (1.4)$$

Hexagonal Prismatic Packing:

$$\lambda = 2(\sqrt{3}a - r) \quad (1.9)$$

Rhombic Dodecahedron Packing:

$$\lambda = 2(y - r) \quad (1.12)$$

where,  $r$  = Radius of the SiC particle size

$a$  = Lattice Parameters

$y$  = Length of the major diagonal of the base of the hexagonal prism or major diagonal of any rhombus of the rhombic dodecahedron.

$r$  = Radius of the SiC particle.

Using these equations and expressing the value of  $a$  and  $y$  as a function of the SiC content in the composite, the interparticle distances were obtained. The theoretical values for the above three models along with the experimental values are shown in Fig.

54.

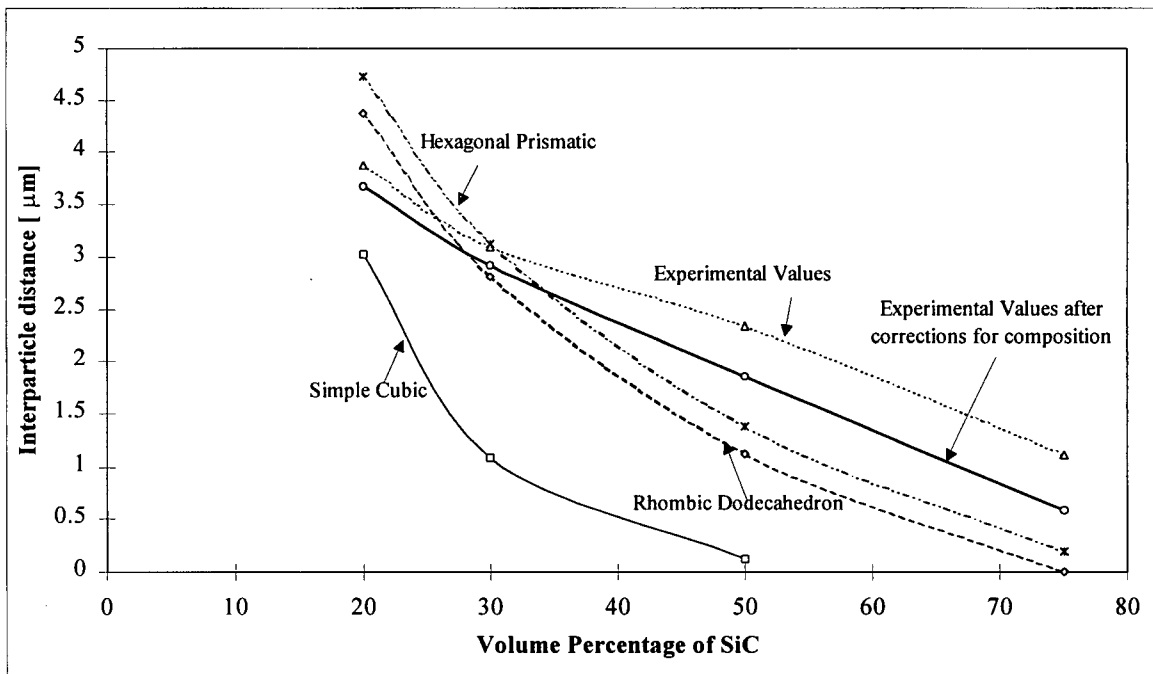


Fig. 54: Change in interparticle spacing with SiC content in the Al-SiC composite. Interparticle distance with three commonly found packing modes a) Simple Cubic b) Hexagonal Prismatic c) Rhombic Dodecahedron has been compared with the experimental values.

Similarly, the variations of the interparticle distance  $\lambda$ , with the SiC particle sizes were obtained using the above equations where the lattice parameters were obtained as a function of the SiC particle size. The SiC content in the composite was kept constant at 50 volume percentage.

The theoretical lines along with the experimental values are shown in Fig. 55.

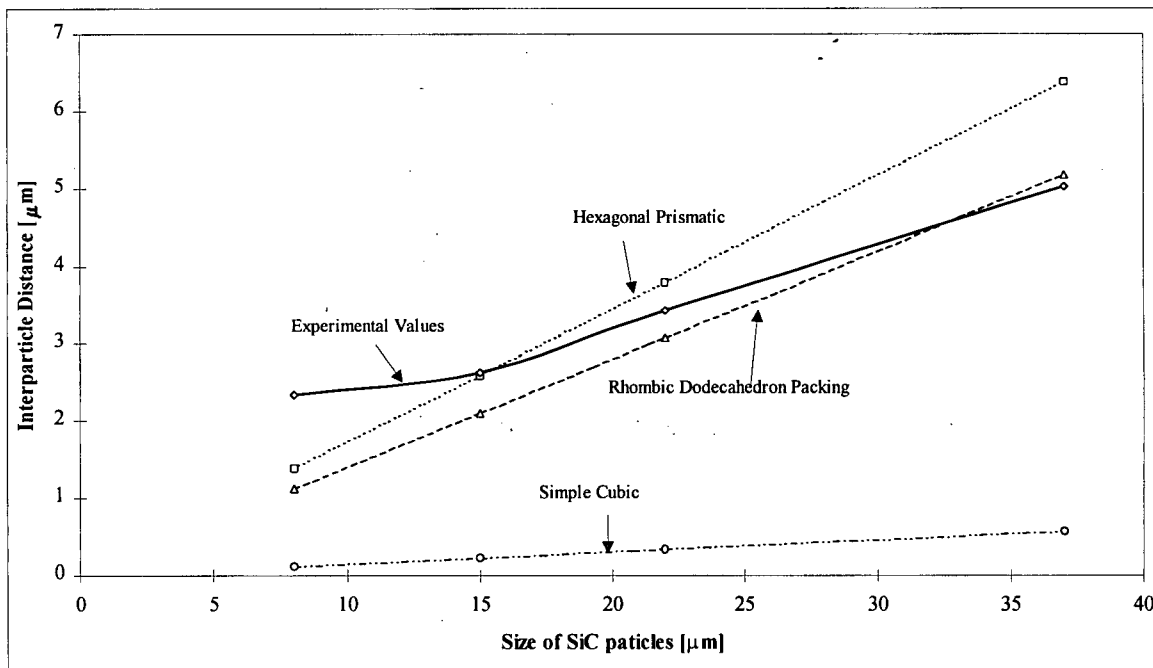


Fig. 55: Change in interparticle spacing with SiC particle sizes in Al-50SiC composites.

Interparticle spacing with three commonly found packing modes a) Simple cubic b) Hexagonal prismatic c) Rhombic Dodecahedron has been compared with the experimental values.

### 6.3 Discussion of model

The experimentally determined  $\lambda$  values are close to the values obtained by the hexagonal prismatic and the rhombic dodecahedron packing modes. The maximum density achievable by a given packing mode is decided by the volume percentage at

which the SiC particles are in contact with each other. A simple cubic mode of packing can achieve at most 56% of the theoretical density. Since, in the present investigation SiC content was as high as 75vol%, it is believed that simple cubic could not be the packing mode for the investigated coatings.

The interparticle distance obtained from the hexagonal packing and the rhombic dodecahedron packing have similar values. The interparticle distance increases linearly with the increase in SiC particle size, as shown in Fig. 55. The interparticle distance,  $\lambda$ , is proportional to  $(1/v)^{1/3}$  where  $v$  is the volume percent of SiC in the composite.

## Chapter 7: Summary and Conclusions

In this study, an attempt has been made to develop a method to improve the surface properties of Al by plasma spraying MMC coatings. The present work consisted of a) developing homogeneous, plasma sprayable Al-SiC powders b) characterization of the composite powders c) plasma spraying of these powders and d) assessing the properties of the plasma sprayed coatings, such as abrasion resistance, erosion resistance, adhesion strength hardness and density.

The following conclusions can be drawn based on the results obtained in the present investigation:

- i) The process of mechanical alloying using a SPEX mixer mill was used to get a uniform distribution of the SiC in the Al matrix. The use of Process Control Agents (PCA) improved the efficiency of mechanical alloying.
- ii) The yield of the sprayable powders, defined as the weight fraction between 44 and 149  $\mu\text{m}$ , decreased with increase in SiC content and with increase in the SiC particle sizes. Al-20SiC1200 had the highest yield of 55wt% compared to the low yield of 17wt% obtained for the Al-75SiC1200 coatings.
- iii) Yield of the powders improved with the addition of PCA. For most of the investigated composite compositions, the highest yield was obtained for 3wt% PCA content.

- iv) Microstructure of the mechanically alloyed powder cross sections showed homogeneous distribution of SiC in the Al matrix. The composite powders showed spherical morphology for all the composites except the Al-75SiC1200 MMC.
- v) The plasma sprayed Al-SiC composite powders produced dense homogeneous coatings.
- vi) Hardness of the coatings was higher than that of Al 6061 alloy which was used as the matrix material. The hardness values increased with increase in SiC content and SiC particle size. The variation in the hardness value was limited to  $\pm 5\%$  of the mean for all the powders except Al-50SiC400 composite.
- vii) ASTM C633-79 tensile adhesion tests were inconclusive with most of the failures occurring in the glue-coating, glue-substrate interfaces or cohesive failures within the coating. Peel Tests provided adhesion strength of the coatings on various substrates. The adhesion strength increased with increase in SiC particle size and was proportional to the content of Al in the composite. Al substrates showed the highest adhesion strength for any given composition of the coating. The adhesion strength of Ni, steel and stainless steel decreased in the similar order.
- viii) The abrasive wear properties of the coatings was superior to the commercially available Al-Al<sub>2</sub>O<sub>3</sub>400 composites. The increase in SiC content from 30 to 50vol% of the MMC increased the wear resistance. However, the wear resistance decreased for the 75 vol% SiC coatings. Amongst the four SiC particle sizes with 50vol% of the reinforcements used in this present investigation Al-50SiC600 containing 22  $\mu\text{m}$ , showed the best abrasion resistance.

ix) The erosion resistance of the Al-SiC coatings was directly proportional to the SiC content. Consequently, Al-75SiC1200 showed the best erosion wear resistance amongst the coatings with the same size reinforcement particles. The erosion wear resistance decreased with increase in the SiC particle size.

The present investigation indicates conclusively that Al-SiC coatings can improve the surface characteristics of structural Al components. The wear resistance of the coating was better than the commercially available cast Al-20Al<sub>2</sub>O<sub>3</sub> composites, thereby providing an alternative to the costly manufacture of structural MMC components. Alternatively, the composites can also be used as a material for surface repair of worn structural MMC.

## Chapter 8: Future Work and Recommendations

Further studies are required to commercialize the plasma sprayable Al-SiC coatings. These should include - a) development of the powder manufacturing process, b) optimization of the coating deposition and c) characterization of coating properties and their performance in various environments.

a) Commercialization of the powder processing technique would require increasing the productivity of the mechanical alloying process. Using an attritor, instead of a SPEX mill is expected to increase the productivity. Optimization of the mechanical alloying in the attritor is equally important.

b) Optimization of the plasma spraying process should involve the essential parameters like the spraying distance, applied powder and plasma gas.

c) Although Al-50SiC600 coatings showed the best combination of abrasion and erosion resistance, the wear resistance of coatings of similar compositions (close to 50vol% SiC) and similar reinforcement particle sizes should also be assessed. The reasons for the difference should be further explored.

The main objective of the coatings is to improve of the wear and abrasion properties of the softer Al substrates. Hence, further studies on the wear properties of the coatings are required. The mechanism of wear in the coatings needs to be determined to obtain a better insight into the wear resistance. Standard ASTM tests need to be conducted for comparison of the wear resistance with the other commercially available materials.

## 9.0 References:

1. D.S. Rickerby and A. Matthews, *Advanced Surface coatings: a Handbook of Surface Engineering*, Chapman and Hill, 1991.
2. R.C. Tucker, Jr., *Proceedings of ITSC '95, Kobe (May, 1995)*, 253-258.
3. Ph. Roumilhac, M. Vardelle, A. Vardelle and P. Fauchais, *Proceedings of the National Thermal Spray Conference*, 1988, 111-116.
4. M.L. Thorpe and W.R. Kratochvil, *Proceedings of the National Thermal Spray Conference*, 1988, 9-18.
5. A. Ilyuschenko, P. Vityaz, V. Okovity, A. Verstak, E. Lugscheider and P. Remer, *Proceedings of the 8<sup>th</sup> National Thermal Spray Conference, Houston, (September 1995)*, 317-320.
6. S.J. Hong and P.W. Kao, *Materials Science and Engineering*, A119, (1989), 153-159.
7. J.F. Garneau, R. Angers, M.R. Krishnadev and L. Collins, *32<sup>nd</sup> Annual Conference of Metallurgists of CIM*, 1993, 27-36.
8. M. Mohanty and R.W. Smith, *Journal of Thermal Spray Technology*, Vol. 4(4), 1985, 384-394.
9. M. Sternitzke, M. Knetchel, M. Hoffman, E. Broszeit and J. Rodel, *Journal of American Ceramic Society*, Vol. 79(1), 1996, 121-128.
10. B. Venkataraman and G. Sundarajan, *Acta Materialia*, Vol. 44, No. 2, 1996, 451-460
11. S. Chung and B.H. Hwang, *Tribology International*, Vol. 27(5), 1994, 307-314.
12. M.I. Boulos, P. Fauchais and E. Pfender, *Advances in Thermal Spraying*, Short Course, June 1993, Anaheim, California.
13. R.W. Smith, M. Mohanty, E. Stessel and A. Verstak, *Proceedings of ITSC '95, Kobe (May, 1995)*, 1121-1126.
14. T.H. Stenberg, K.J. Niemi, P.M.J. Vuoristo, J.E. Vuorinen, T.A. Mantlya and T.J. Tianen, *Proceedings of ITSC '95, Kobe (May, 1995)*, 1145-1150.

15. K.A. Khor, Y. Murakoshi and T. Sano, *Proceedings of ITSC '95, Kobe (May, 1995)*, 1133-1137.
16. I.C. Stone and P. Tsakirooulos, *Material Science and Technology*, Vol. 11, March 1995, 213-221.
17. J.S. Benjamin and R.D. Schelleng, *Metallurgical Transactions A*, Vol. 12A, 1981, 1827-1832.
18. P.S. Gilman and J.S. Benjamin, *Ann. Rev. Mater. Sci.*, Vol. 13, 1983, 279-300.
19. G. Mahanty, A.N. Tiwari, V. Gopinathan and P. Ramakrishnan, *Key Engineering Materials*, Vol. 29-31, 1989, 747-754.
20. L. Lu, M.O. Lai and S. Zhang, *Key Engineering Materials*, Vol. 37, May 1995.
21. J. Kaneko, M. Sugamata and R. Horiuchi, *8th. International Light Metals Congress, Leoben - Vienna*, 1987, 776-780.
22. A. Bhaduri, A.N. Tiwari, V. Gopinathan and P. Ramakrishnan, *Materials Science Forum*, Vols. 88-90, 1992, 205-212.
23. T.G. Nieh, C.M. McNally, J. Wadsworth, D.L. Yaney and P.S. Gilman, *Proceedings of the six-session symposium on "Dispersion Strengthened Aluminum alloys"*, January 1988, 681-692.
24. E. Hochreiter, C. Kowanda and B. Ortner, *Journal de Physique IV*, Vol. 3, November 1993.
25. M. Abdellaoui and E. Gaffet, *Acta Materialia*, Vol. 43, No. 11, 1995, 1087-1098.
26. M. Abdellaoui and E. Gaffet, *Acta Materialia*, Vol. 44, No. 2, 1996, 725-734.
27. D.R. Maurice and T.H. Courtney, *Metallurgical Transactions A*, Vol. 21A, 1990, 289-303.
28. P.S. Gilman and W.D. Nix, *Metallurgical Transactions A*, Vol. 12A, 1981, 813-824.
29. K.D. Jayasuriya, S.J. Campbell, A. Calka and J. Jing, *Nuclear Instruments and Methods in Physics Research*, Vol. B76, 1993, 85-88.
30. R.F. Singer, W.C. Oliver and W.D. Nix, *Metallurgical Transactions A*, Vol. 11A, 1980, 1895-1901.

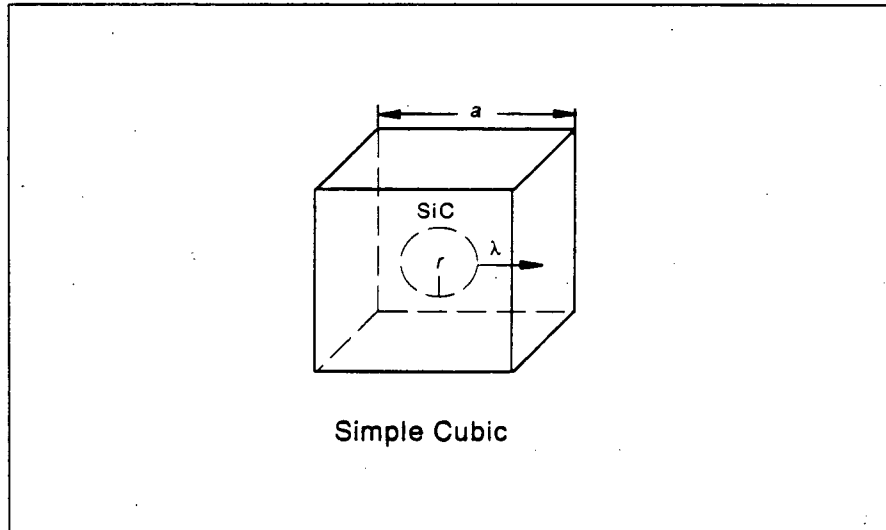
31. M. Magini, *Material Science Forum*, **88-90**, 1992, 121.
32. R.M. Davis, B. Mcdermott and C.C. Koch, *Metallurgical Transactions A*, 1988, **Vol. 19A**, 2867-2874.
33. P. Streb, H.T. Steine, W. Simm, H. Oechsle, R. Dumola and P.A. Kammer, *Proceedings of the National Thermal Spray Conference*, 1988, 367-374.
34. S.Sampath and H. Herman, *Proceedings of the National Thermal Spray Conference*, 1988, 1-8.
35. M. Fukumoto, H. Tsunekawa, M. Umemoto and I. Okane, *Nihon Kinzoku Gakkaishi (Journal of the Japan Institute of Metals)*, **Vol. 57(9)**, 1993, 1078-1082.
36. R.W. Smith, D. Gentner, E. Harzenski and T. Robisch, *Proceedings of the National Thermal Spray Conference*, 1988, 299-306.
37. S.H. Leigh and C.C. Berndt, *Journal of Thermal Spray Technology*, **Vol. 3(2)**, 1994, 184-190.
38. C.K. Lin and C.C. Berndt, *Journal of Thermal Spray Technology*, **Vol. 3(1)**, 1994, 75-104.
39. M. Sexsmith, *A Peel Adhesion test For Thermal Spray Coatings*, **M.A.Sc. thesis**, 1995, University of British Columbia.
40. M. Sexsmith and T. Troczynski, *Proceedings of ITSC '95, Kobe (May 1995)*, 897-901.
41. M. Sexsmith and T. Troczynski, *Journal of Thermal Spray Technology*, **Vol. 5(2)**, 1996, 196-206.
42. M. Sexsmith and T. Troczynski, *Proc. of 7<sup>th</sup>. Natl. Th. Spr. Conference*, Boston, 1994, 751-757.
43. M. Sexsmith, T. Troczynski and E. Breslauer, *J. of Adh. Sci. & Tech.* (to be published).
44. E. Breslauer and T. Troczynski, *J. of Adh. Sci. & Tech.* (to be published).
45. A. Kassman, S. Jacobson, L. Erickson, P. Hedenqvist and M. Olsson, *Surface and Coating Technology*, **Vol. 50**, 1991, 75-84.

46. I.M. Hutchings, *Tribology: Friction and Wear of Engineering Materials*, **Edward Arnold (Division of Hodder & Stoughton)**, Chapter 5, 77-122.
47. *Vogel's Textbook of Quantitative Chemical Analysis*, Fifth Edition, **Longman Scientific & Technical**, 1989.
48. P.V. Ananthapadmanabhan, K.P. Sreekumar, P.V. Ravindran, N. Venkatramani and S.C. Mishra, *Proceedings of ITSC '95, Kobe (May 1995)*, 1127-1131.
49. A.D. Crocombe and R.D. Adams, *Journal of Adhesion*, **Vol. 13**, 1982, 241-267.
50. A.D. Crocombe and R.D. Adams, *Journal of Adhesion*, **Vol. 12**, 1981, 127-139.
51. M.D. Thoules and H.M. Jensen, *Journal of Adhesion*, **Vol. 38**, 1992, 185-197.
52. K. Kim and J. Kim, *Journal of Engineering Materials and Technology*, **Vol. 110**, 1988, 266-273.
53. S.C. Lim and M.F. Ashby: *Acta. Metall.*, **Vol. 35**, 1987, 1-24.
54. G.E. Dieter, Jr., *Mechanical Metallurgy*, **McGraw-Hill Book Company, Inc.**, 1961.
55. R.W. Davidge, "*Mechanical Behavior of Ceramics*", Cambridge Univ. Press, Cambridge, 1979.
56. B.D. Cullity, "*Elements of X-ray Diffraction*", Addison Wesley Publishing Company, Inc., Second Edition, 1978.
57. ASM Metals Handbook, *Properties of Non-Ferrous Alloys*, **Vol. 2**, 10<sup>th</sup> Edition, Page 103.
58. I.J. McColm, *Ceramic Hardness*, **Plenum Press**, 1990.
59. A.K. Kakkar, *Deformation Theory of Hot Pressing*, **PhD. Thesis**, University of British Columbia, August 1967.
60. J.S. Reed, *Introduction to Principles of Ceramic Processing*, **John Wiley & Sons**, 1988.
61. L. Erickson, T. Troczynski and H. Hawthorne, *Proceedings of ITSC '95, Kobe (May, 1995)*, 743-749.

**Appendix (I): Calculations for the variation of interparticle distance with mode of packing and Al matrix content.**

**A) Change in Interparticle distance with SiC content**

**1. Simple Cubic Packing:**



Volume of each particle,  $V_p = \frac{4}{3}\pi r^3$  (where  $r$  = average radius of the SiC particles)

Since each of the unit cells represent the average composition of the composite, therefore,

For simple cubic geometry,

$$\text{Volume of each cell, } V_c = \left(\frac{4}{3}\right) \pi r^3 \times (100/v), \quad (1.1)$$

$$= a^3$$

$a$  = lattice parameter of a unit cell.  
and  $v$  = Vol% of SiC in the composite.

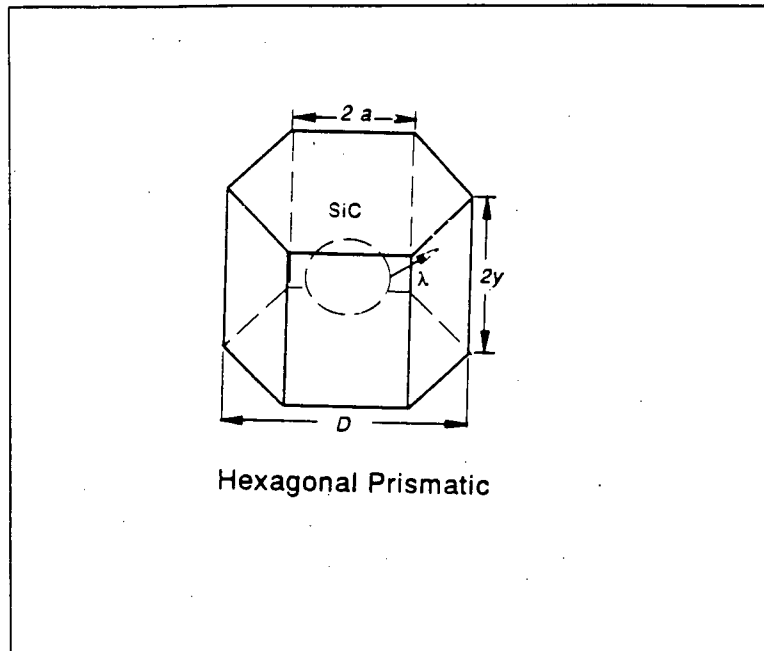
$$\therefore a^3 = \left(\frac{4}{3}\right) \pi r^3 \times (100/v) \quad (1.2)$$

$$\text{or, } a = \sqrt[3]{\left(\frac{4}{3}\right) \pi r^3 \times (100/v)} \quad (1.3)$$

Therefore interparticle distance " $\lambda$ " can be obtained as -

$$\lambda = (a/2 - r) \times 2 \quad (1.4)$$

## 2. Hexagonal Packing:



Calculating, in a similar way as in simple cubic, we get,

Volume of each cell,  $V_c = (4/3) \pi r^3 \times (100/v)$ ,       $v = \text{vol\% of SiC in the composite}$

$$= \frac{3\sqrt{3}}{8} D^2 H, \quad (1.5)$$

$D = \text{diagonal length of the base of prism}$

and  $H = \text{Height of the hexagonal cell.}$

Using the geometric properties of hexagonal prisms, it can be shown that,

$$H = 2y = 2(3)^{1/2} a \quad \text{and} \quad D = 2a$$

where,  $a = \text{half of the length of the base of the hexagon.}$

Therefore, the volume of each cell can be expressed as

$$V_c = \frac{3\sqrt{3}}{8} \times 4a^2 \times 2\sqrt{3}a \quad (1.6)$$

$$= 9a^3$$

Equating the volume of the cell from Eqn. (1.5) and Eqn. (1.6) we get,

$$9 a^3 = (4/3) \pi r^3 \times (100/v)$$

$$\text{or, } a = \sqrt[3]{(4 \pi r^3 \times (100/v))/3} \quad (1.7)$$

Thus, the interparticle distance of two SiC particles in adjacent cells is given by

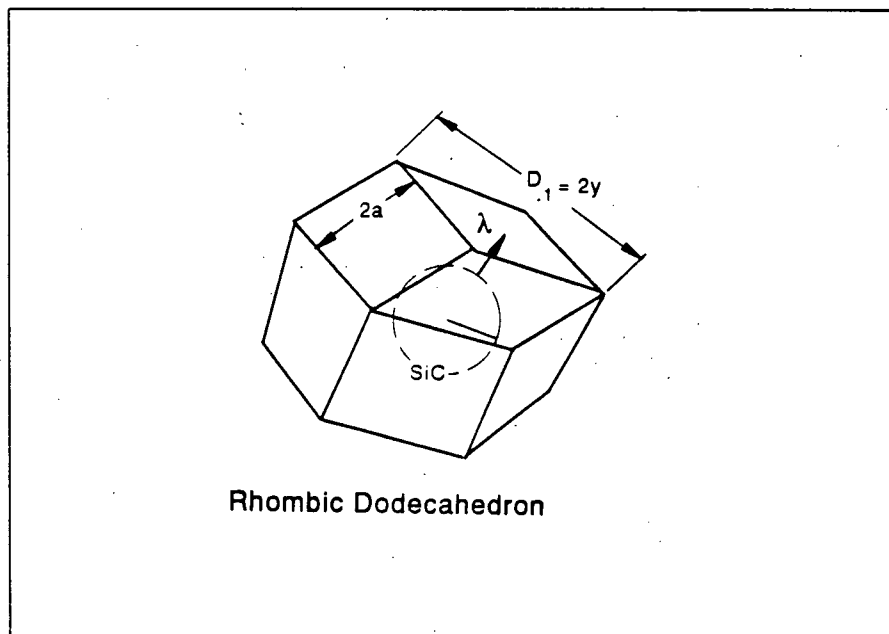
$$\lambda = (r_1 - r) \times 2 \quad (1.8)$$

$$\text{where, } r_1 = \sqrt{(R^2 - a^2)} = \sqrt{(4a^2 - a^2)} = \sqrt{3}a,$$

and  $r$  = radius of the SiC particle.

$$\lambda = (\sqrt{3}a - r) \times 2 \quad (1.9)$$

### 3. Rhombic Dodecahedron Packing:



Calculating, in a similar way as in the previous two packing geometries, we get

$$\begin{aligned} \text{Volume of each cell, } V_c &= (4/3) \pi r^3 \times (100/v), & v &= \text{vol\% of SiC in the composite} \\ &= D_1^3 / \sqrt{2} & D_1 &= \text{major diagonal of each side of} \\ & & & \text{the rhombus.} \end{aligned}$$

Using the geometric properties of rhombic dodecahedron model [41], it can be shown that,

$$D_1 = 2y$$

Substituting the value of  $D_1$ , we get the volume of the cell is equal to -

$$V_c = (2y)^3 / \sqrt{2} = 8y^3 / \sqrt{2} \quad (1.10)$$

or,  $8y^3 / \sqrt{2} = (4/3) \pi r^3 \times (100/v)$

or,  $y = \sqrt[3]{(4\sqrt{2} \pi r^3 \times (100/v))/2}$  (1.11)

The model has six closed packed faces shown by the faces of a hexagon are closest to a particle whose center coincides with the center of the cell.

From the figure of rhombic dodecahedron, it can be shown that the distance between the center of the rhombic dodecahedron to the side of the hexagon is given by  $r_1 = y$

Thus, the interparticle distance of two SiC particles in adjacent cells is given by

$$\lambda = (r_1 - r) \times 2 \quad \text{where, } r_1 = y,$$

and  $r = \text{radius of the SiC particle}$

$$\lambda = (y - r) \times 2 \quad (1.12)$$

Using the above equations and the four SiC compositions (20, 30, 50 and 75 vol% of SiC) used for the 1200 grit composition, the interparticle distance variation with SiC content has been calculated.

## B) Change in Interparticle distance with SiC particle size

Let the radius of the 1200 grit SiC be represented by  $r_{d2}$  and the radius of the 400, 600 and 800 grits (37, 22 and 15  $\mu\text{m}$  respectively) be represented by  $r_{d1}$

The volume percentage of SiC in the composites for the given calculations was kept constant at 50 vol% and hence a value of 50 was substituted for “ $v$ ” used in Eqn. 1.1.

Thus, since the SiC particles are assumed to be spherical in shape

$$\frac{4}{3} \pi r_{d1}^3 = N \frac{4}{3} \pi r_{d2}^3 \quad \text{where, } N \text{ is always greater than 1.}$$

Thus, 
$$\left(\frac{r_{d1}}{r_{d2}}\right)^3 = N \quad (1.13)$$

and  $N$  can be defined as the ratio of the volume of the 400, 600 and 800 grit SiC (37, 22 and 15  $\mu\text{m}$ , respectively) particles with the 1200 grit SiC (8  $\mu\text{m}$ ) reinforcements.

### 1. Simple Cubic Packing

Using the value of the interparticle distance obtained in Eqn. 1.4, we get

$$\lambda = (a/2 - r_{d1}) \times 2$$

Substituting the value of  $r_{d1}$  from eqn. 1.13, we obtain

$$\lambda = (a/2 - r_{d2}^{1/3} \cdot N^{1/3}) \times 2 \quad (1.14)$$

Substituting the value of  $a$  from Eqn. 1.3 and the value of  $v$ , we get the interparticle distance

$$\lambda = ((\sqrt[3]{(4/3) \pi r_{d2} N \times (100/50)})/2 - r_{d2} N^{1/3}) \times 2 \quad (1.15)$$

## 2. Hexagonal Packing

Similarly, using the value of the interparticle spacing obtained from Eqn. 1.9,

$$\lambda = (\sqrt{3}a - r) \times 2$$

Substituting the value of  $a$  from Eqn. 1.7, the value of  $r$  from Eqn. 1.13, and the value of  $v$  we get the interparticle distance as

$$\lambda = \left( \sqrt[3]{\frac{4}{3} \pi r d_2 N \times (100/50)} / 3 - r d_2 N^{1/3} \right) \times 2 \quad (1.16)$$

## 3. Rhombic Dodecahedron Model

Similarly, using the value of the interparticle spacing for rhombic dodecahedron model obtained from Eqn. 1.12, we get

$$\lambda = (y - r) \times 2$$

where, the value of  $y$  is obtained from Eqn. 1.11.

Substituting the values of  $y$  and  $r$  from Eqn. 1.11 and 1.13 respectively the interparticle distance for the rhombic dodecahedron model the change in values can be represented as,

$$\lambda = \left( \sqrt[3]{\frac{4\sqrt{2}}{3} \pi r d_2 N \times (100/50)} / 2 - r d_2 N^{1/3} \right) \times 2 \quad (1.17)$$

**Table 1.1** Variation of  $N$  ( obtained from Eqn. 1.13) with SiC grit size.

SiC grit size used as reinforcement	Value of $N$
1200	1
800	6.592
600	20.797
400	98.932